

**Development of a Micropatterned System to Study the
Role of Protein Tethers in Lipid Membrane Organization**

Samuel Lourenço Jacob

Thesis to obtain the Master of Science Degree in
Bioengineering and Nanosystems

Supervisors: Dr. Fábio Monteiro Fernandes,
Prof. João Pedro Estrela Rodrigues Conde

Examination Committee

Chairperson: Prof. Dr. Luís Joaquim Pina da Fonseca
Supervisor: Dr. Fábio Monteiro Fernandes
Member of the Committee: Dr. Liana Silva

November 2014

*Nature is the ultimate expression of freedom,
for it could not care less about the approval or satisfaction
of those with whom it shares existence.*

ACKNOWLEDGMENTS

An opening courtesy goes to Professor Manuel Prieto for accepting me for the research thesis and providing me with not only a great work opportunity, but offering good disposition and so many lectures on history, geography and other interesting subjects. On equal grounds, I would like to thank my main supervisor Dr. Fábio Fernandes for the bright ideas, support and strife through what it proved to be a fun, winding, but nonetheless difficult journey of unwanted results. I want to thank my supervisor at INESC-MN, Professor João Pedro Conde, for his enthusiasm, optimism, and backing throughout the project. Also, a special thanks to Dr^a. Virginia Chu, always ready to help and boost the project.

I want to acknowledge the help of all my lab partners. Particularly, I want to thank Marina Monteiro, for the exceptional achievement of keeping a cool head while sharing the cabinet with me, and to Paulo Caldas, my old acquainted friend, for the jokes, cheer and infinitely fun-to-do phosphate essays. I would like to thank Virginia Soares and José Bernardo for the lithography processes and help at INESC-MN.

One great share of gratitude goes to my dear Eva, for the immeasurable support, affection, intelligence and good taste. I must also thank my friend Denys Holovanchuk and, again, Paulo Caldas – we are the living proof that a group can be fun, silly and productive at the same time. A special acknowledgment goes to three of my oldest and closest friends in Algarve: Daiana, Artur and João de Sá. But to my family, I am most grateful. I would like to thank my mother for the unconditional support through all my life – even though my career is young, it could not even have been born without her; to my brother, for the classical music and violin melodies which, I am sure, provided plenty of inspiration; to my grandmother, for the excessive and wonderful food provided in my retreats from Lisbon to Algarve. Finally, I want to thank my late grandfather, for the example and all the memories.

ABSTRACT

The plasma membrane is a complex matrix of phospholipids and proteins that mediates important biological events. These events ultimately depend on the formation of lateral heterogeneities called membrane rafts. The plasma membrane interacts with the cytoskeleton, which is thought to help define and organize these rafts. Cytoskeleton adhesions to the membrane, such as those mediated by PIP₂, are thought to have a high impact on lipid distribution, especially if the membrane displays critical behavior. This work aimed to construct a model system that mimics cytoskeleton-PIP₂ tethers to the membrane. Making use of photolithography, we defined an avidin micropatterning on glass substrate; then, using supported lipid bilayers (SLBs) formed from liposomes containing biotinylated lipid, we attempted to study the effect of avidin-biotin binding in lipid phase separation and domain organization. Our optimization experiments showed that although formation of SLBs from small unilamellar vesicles onto the protein-coated surfaces did not occur, giant unilamellar vesicles (GUVs) adhered to an avidin surface and collapsed to form supported membranes as induced by osmotic shock. However, these giant liposomes were unable to adhere and form SLBs onto an avidin micropatterned surface, possibly due to folding modifications occurring by organic solvent washing during microfabrication. Although the optimization of this model system is yet to be completed, the collapse of GUVs by osmotic shock on micropatterned protein surfaces is a promising tool to generate a model for the study of the interplay between membrane adhesions and lateral lipid domain formation.

Keywords: Membrane raft, phase separation, cytoskeleton, membrane adhesion, microfabrication, supported lipid bilayers.

RESUMO

A membrana plasmática é uma estrutura celular complexa, constituída por fosfolípidos e proteínas, que desempenha uma variedade de funções biológicas essenciais. Estas funções estão associadas à formação de heterogeneidades laterais denominadas jangadas lipídicas. A membrana plasmática interage com o citoesqueleto, que por sua vez tem capacidade de organizar e definir as jangadas lipídicas. Pensa-se que as ancoragens do citoesqueleto à membrana celular, mediadas por lípidos como o PIP₂, têm um forte impacto na distribuição lipídica; uma vez que, aparentemente, a membrana apresenta um comportamento crítico, o efeito destas adesões torna-se mais importante e acentuado. Este projecto teve como objectivo construir um sistema modelo para mimetizar as adesões citoesqueleto-membrana. Usando fotolitografia, construiu-se um micropadrão de avidina em substrato de vidro; depois, usando membranas suportadas formadas por lipossomas contendo lípido biotinilado, pretendemos estudar o efeito da ligação avidina-biotina na separação de fases e organização de domínios. Os resultados obtidos revelaram que, apesar de a formação de membranas suportadas em vidro revestido com proteína não ter ocorrido usando lipossomas pequenos, lipossomas gigantes aderiram a superfícies revestidas de avidina e rebentaram para formar membranas suportadas após o choque osmótico. No entanto, estas vesículas foram incapazes de aderir à superfície padronizada com avidina, provavelmente devido a modificações de *folding* proteico aquando do processo de fabricação. Apesar deste sistema modelo estar por completar, a formação de membranas suportadas a partir de lipossomas gigantes em superfícies micropadronizadas com proteína é uma estratégia promissora para o estudo do papel das adesões membranares na formação de domínios lipídicos.

Palavras-chave: Jangada lipídica, separação de fases, citoesqueleto, adesões membranares, fotolitografia, membranas suportadas.

TABLE OF CONTENTS

Acknowledgments	ii
Abstract	iii
Resumo	iv
List of Figures	vii
List of Abbreviations	xv
1. INTRODUCTION	1
1.1. Plasma Membrane - Cytoskeleton Interactions.....	2
1.1.1. <i>The plasma membrane</i>	2
1.1.2. <i>Membrane rafts</i>	3
1.1.3. <i>Phase separation in lipid membranes</i>	4
1.1.4. <i>Cytoskeleton role in plasma membrane organization</i>	7
1.1.5. <i>PIP₂ role in cytoskeleton adhesions to the plasma membrane</i>	11
1.2. Membrane Model Systems in Biophysics	14
1.2.1. <i>Membrane model systems review</i>	14
1.2.2. <i>Merging micro/nanotechnologies and biophysics</i>	16
1.3. Rationale and Objective.....	18
2. MATERIALS AND METHODS	19
2.1. Materials and Reagents.....	20
2.2. Glass Substrate Treatment.....	20
2.2.1. <i>Functionalization with 3-glycidyloxypropyl trimethoxysilane</i>	20
2.2.2. <i>Photolithography</i>	20
2.2.3. <i>Protein immobilization</i>	21
2.2.4. <i>Avidin micropatterning</i>	21
2.2.5. <i>Biotin-fluorescein experiments</i>	22
2.3. Preparation of Supported Lipid Bilayers.....	22
2.3.1. <i>Lipid quantification</i>	22
2.3.2. <i>Small unilamellar vesicles</i>	23
2.3.3. <i>Giant unilamellar vesicles</i>	23
2.4. Confocal and Two-Photon Scanning Laser Microscopy Imaging	24
2.4.1. <i>Experimental setup</i>	24
2.4.2. <i>Image acquisition and treatment</i>	24
2.5. Fluorescence Recovery after Photobleaching.....	25
2.5.1. <i>Basic principles</i>	25
2.5.2. <i>Model for two-dimensional diffusion</i>	26

2.5.3.	<i>FRAP data acquisition</i>	27
2.5.4.	<i>FRAP data analysis</i>	28
3.	RESULTS AND DISCUSSION	29
3.1.	Fabrication of Avidin Micropatterning on Glass Substrate	30
3.1.1.	<i>Avidin and BSA immobilization on glass and resistance to acetone washing</i>	30
3.1.2.	<i>Model system conceptualization</i>	32
3.1.3.	<i>Avidin micropatterning fabrication on clean and GPTS-functionalized glass</i>	33
3.1.4.	<i>Avidin micropatterning fabrication using biotinylated BSA</i>	37
3.1.5.	<i>Effect of the microfabrication procedure on avidin ability for binding biotin</i>	40
3.2.	Formation of Supported Lipid Bilayers from Small Unilamellar Vesicles	42
3.2.1.	<i>Effect of avidin micropatterning in the formation and organization of supported lipid bilayers containing a ternary lipid mixture of POPC, Chol and PSM</i>	42
3.2.2.	<i>Formation of supported lipid bilayers from POPC SUVs onto BSA-coated glass substrate</i>	45
3.2.3.	<i>Formation of supported lipid bilayers from POPC SUVs onto avidin-micropatterned glass substrate</i>	48
3.2.4.	<i>Effect of temperature in the formation of supported lipid bilayers from POPC SUVs onto BSA and BSA-biotin/avidin-coated glass substrate</i>	51
3.2.5.	<i>Effect of poly (ethylene glycol) in the formation of supported lipid bilayers from POPC SUVs onto avidin-coated glass substrate</i>	53
3.3.	Formation of Supported Lipid Bilayers from Giant Unilamellar Vesicles	55
3.3.1.	<i>Formation of supported lipid bilayers from GUVs onto avidin-coated Ibidi glass bottom slides</i>	55
3.3.2.	<i>GUV concentration by glucose/sucrose density difference deposition</i>	57
3.3.3.	<i>Formation of supported lipid bilayers from GUVs onto avidin-coated glass Ibidi glass bottom slides by osmotic shock</i>	59
3.3.4.	<i>Formation of supported lipid bilayers from GUVs onto non-micropatterned and micropatterned avidin-coated glass coverslips</i>	61
3.3.5.	<i>Effect of acetone washing on GUV immobilization onto BSA-biotin and avidin-coated glass substrate</i>	63
3.4.	Final Remarks and Future Perspectives	65
4.	REFERENCES	67

LIST OF FIGURES

Figure 1.1 - Representation of the three classes of lipids present in the plasma membrane of mammals. The quantities of each class of lipid, in percentage of total lipid, are displayed below each category. Adapted from (4)..... 2

Figure 1.2 - Membrane raft model. Cholesterol associations with other lipids, such as sphingolipids, generate a discrete lipid compartment or domain with unique physical and biological properties. Cholesterol confers an ordering on the lipids that imparts changes in physical properties of the bilayer, including increased thickness and stiffness. Through poorly understood mechanisms, the rafts are coupled across the bilayer. Proteins that prefer an ordered lipid environment associate with the domains, often through a discrete targeting signal. A frequent raft signaling for proteins is palmitoylation of a membrane-proximal cysteine. Rafts are also enriched in GPI-anchored proteins. The blue and grey lipids represent “raft” and “non-raft” respectively. Adapted from (138). 3

Figure 1.3 - Hierarchy of raft-based heterogeneity in cell membranes. (A) Fluctuating nanoscale assemblies of sterol- and sphingolipids-related biases in lateral composition. This sphingolipids/sterol assemblage potential can be accessed and/or modulated by GPI-anchored proteins, certain TM proteins, acylated cytosolic effectors and cortical actin. Gray proteins do not possess the chemical or physical specificity to associate with this membrane connectivity and are considered non-raft. GPL, glycerophospholipids; SM, sphingomyelin. (B) Nanoscale heterogeneity is functionalized to larger levels by lipid- and/or protein-mediated activation events (e.g., multivalent ligand binding, synapse formation, protein oligomerization) that trigger the coalescence of membrane order-forming lipids with their accompanying selective chemical and physical specificities for protein. This level of lateral sorting can also be buttressed by cortical actin. (C) The membrane basis for heterogeneity as revealed by the activation of raft phase coalescence at equilibrium in giant plasma membrane vesicles (GPMVs). Separated from the influence of cortical actin and in the absence of membrane traffic, multivalent clustering of raft lipids can amplify the functional level to a microscopic membrane phase. Membrane constituents are laterally sorted according to preferences for membrane order and chemical interactions. Adapted from (18). 5

Figure 1.4 – Transition temperature and critical fluctuations in GPMVs. GPMVs are uniform at high temperature and contain two coexisting liquid phases at low-temperature. GPMVs undergo micrometer-scale fluctuations at temperatures just above their respective miscibility transition temperature, visualized when cells are pre-labeled with a fluorescent lipid analog. The critical temperature falls roughly between the second and third images. Scale bars are 5 μm . Adapted from (32). 6

Figure 1.5 - The fence-and-picket model of membrane organization. (A) Schematic view of the plasma membrane, showing the membrane skeleton (MSK), the diffusing transmembrane (TM) protein (red), and a TM protein anchored to the MSK, acting as a picket (blue). (B) The membrane-skeleton

“fence” model (the bottom view of the plasma membrane, i.e., the view from inside the cell). The plasma membrane may be partitioned into closely apposed domains (compartments) for the translational diffusion of membrane molecules. All the membrane-constituent molecules undergo short-term confined diffusion within a compartment and long-term hop movement between compartments (hop diffusion). The compartment boundaries are composed of the actin-based MSK (fence) and the TM proteins anchored to and aligned along the actin fences (pickets, including the TM proteins transiently bound to the actin fences). (D) The diffusion of molecules in the region around the immobilized TM (reddish-orange region) is slower, owing to the hydrodynamic friction-like effect at the surface of the immobilized protein. This effect could propagate over distances equivalent to multiple diameters of picket proteins. When such diffusion barriers are aligned along the membrane-skeleton fence, they form effective compartment boundaries. Adapted from (48). 9

Figure 1.6 - Three-tiered hierarchical mesoscale-domain architecture of the plasma membrane.

(A) Membrane compartments, generated by the partitioning of the entire plasma membrane by the membrane-associated actin-based membrane skeleton (fence) and transmembrane (TM) proteins anchored to the membrane-skeleton fence (pickets, not shown in this figure). (B) Raft domains enriched in cholesterol, glycosphingolipids and GPI-anchored proteins, with sizes limited by the membrane compartments. (C) Dynamic protein complex domain composed of dimers and greater oligomers of integral membrane proteins, which may exist only transiently. This type of domain also includes coat-protein-induced and scaffolding-protein-induced protein assemblies. Adapted from (48). 11

Figure 1.7 - Regulation of actin-binding proteins by PIP₂. Local increase of PIP₂ concentration affects many aspects of the actin cytoskeleton. (A) Plasma membrane - actin cytoskeleton interactions are enhanced through the activation of ERM-family proteins. (B) Cell adhesion to the extracellular matrix (ECM) is increased by enhancing the binding of talin of β-integrins. (C) The activity of WASP and WAVE family proteins is enhanced by PIP₂. These proteins promote Arp2/3-mediated actin filament assembly. (D) Filament barbed end and capping proteins, such as gelsolin and heterodimeric capping protein, are inhibited by PIP₂. (E),(F) Actin filament disassembly and monomer sequestering are diminished through inhibition of ADF/cofilin and twinfilin by PIP₂. Adapted from (55). 12

Figure 1.8 - Schematic diagram of a supported lipid bilayer. The membrane is separated from the substrate by a 10 - 20 Å thick layer of water. Adapted from (82). 15

Figure 1.9 - Schematic drawing of photolithography in silicon substrate with a positive photoresist. The first step involves oxidation of the substrate for passivation, forming SiO₂ (a), followed by photoresist spin-coating and heating (b). The previously formed photomask is used to expose photoresist to light (c), which makes it soluble in the photoresist developer (d). By removing the uncovered material by etching process (e) and stripping the remaining photoresist, a pattern is created on the substrate. Adapted from (90). 17

Figure 2.1 – Basic principles of a typical FRAP experiment. The fluorescence signal is measured in the ROI with a low-intensity laser beam ($t < 0$). At $t = 0$, with a high intensity laser beam, the fluorescent molecules are quickly photobleached inside the ROI, causing a decrease in fluorescence.

Then, the diffusion process after photobleaching is again monitored with a low-intensity beam ($t > 0$). Due to diffusion transport, the bleached molecules (purple dots) will exchange their position in the bleached area with non-bleached fluorescence molecules (green) from the surroundings, resulting in a recovery of the signal inside the ROI. By plotting the fluorescence intensity of the photobleached spot as a function of time, a FRAP curve is obtained. With a suitable mathematical model, it is possible to extract the diffusion coefficient D and the local mobile fraction of labeled molecules, M_f . Adapted from (139). 25

Figure 3.1 – General protein immobilization on glass procedure. (A) On cleaned glass substrate (silica substrate), a droplet of avidin is added to the glass coverslips and protein adsorbs on the surface (non-covalent immobilization). (B) On GPTS-functionalized glass (i.e. silanized glass) a droplet of avidin is added in basic pH buffer, necessary for the reaction of amine group(s) on the protein chain with epoxide groups on the surface (covalent immobilization). See Materials and Methods for more details (sections 2.2.1 and 2.2.3). 30

Figure 3.2 – Avidin and BSA resistance to acetone washing after adsorption onto clean or GPTS-functionalized glass. (A) Confocal images showing avidin and BSA-coated surfaces, on clean glass or GPTS-functionalized glass, before acetone washing (1,3,5,7) and after 20 second acetone washing (2,4,6,8). Fluorescence is from avidin-Alexa488 (1:25 mol:mol labeled to unlabelled protein ratio) and from BSA-Alexa594 (1:25 mol:mol conjugate to unlabelled protein ratio). One representative image was chosen among several collected. Scale bar is 25 μm (B) Bar plot showing normalized fluorescence intensity of avidin and BSA surface, on clean glass or GPTS-functionalized glass, before and after 20 second acetone washing. Values represent mean \pm standard deviations. Fluorescence intensity was collected from different areas of the coverslip surface, averaged from at least 3 representative images of the surface, and normalized for the maximum fluorescence observed for each fluorophore. BSA and avidin were added at 1 mg/mL concentration. 31

Figure 3.3 – Model of avidin micropatterning on glass coverslips. Glass coverslips with dimensions 50 x 24 mm contain duplicate regions, each region containing nine squares of 1 x 1 mm. Pink regions correspond to immobilized avidin; white regions correspond to empty or BSA-blocked regions. In the first, second and third row of squares, the whole area with immobilized avidin accounts for 50%, 20% and 10% of the total area, respectively. The side length of the squares decreases from left to right (20, 10 and 5 μm). Each 1 x 1 mm square has a roman numeral so that it can be identified under the microscope (not shown in figure). This distribution of immobilized protein aimed to study the effect of the tether size and total area of tethering in phase separation and lipid membrane reorganization. 32

Figure 3.4 – Protocol used to create an avidin micropatterning on clean or GPTS-functionalized glass using photolithography. A clean or GPTS-functionalized glass coverslip (1) was subject to photoresist spin-coating (2). A laser working at 405 nm irradiated regions to be later immobilized with avidin, pre-defined by a virtual mask (3) and photoresist developer selectively removed irradiated regions, exposing the glass underneath (4). An aqueous solution of avidin was then added to the glass slides for adsorption or reaction with surface epoxides, which are not shown on the picture (5).

Finally, an acetone squirt removed the photoresist containing adsorbed avidin, leaving discrete regions of avidin immobilized on glass either by adsorption (6A) or bound covalently (6B). 33

Figure 3.5 – Photoresist mask designed by photolithography. (A) Photoresist mask fluorescence. Red regions represent photoresist fluorescence and black regions represent exposed glass where avidin was to be later immobilized. Region 1 shows the numeral that identifies which pattern, out of nine possible patterns, was under observation. Region 2 shows the pattern, which is made of 20 μm squares and accounts for 50% of the total 1 x 1 mm square area. Region 3 represents the area outside the patterns, which was filled with photoresist that would later be removed. (B) XZ plane image of photoresist pattern on glass. The glass-water and photoresist-water interface is shown at green and photoresist at red; photoresist thickness was approximately 1.45 μm as expected; between photoresist regions lie squares with 5 μm dimensions. Collected fluorescence is from photoresist. (C) Photoresist emission spectrum obtained under confocal microscope. $\lambda_{\text{exc}} = 488 \text{ nm}$. $\lambda_{\text{em peak}} \approx 605 - 610 \text{ nm}$ 34

Figure 3.6 – Avidin micropatterning formed on clean and GPTS-functionalized glass coverslips. (A) Micropatterning surface after avidin addition to non-functionalized glass, showing 5 μm squares (20% protein-coated area). The numeral that identifies which pattern was under observation, and the average intensity ratios between inside and outside micropatterned regions are also shown. (B), (C) Micropatterning showing 20 and 10 μm side squares (50% and 20% protein-coated area), respectively. (D) Micropatterning surface after avidin addition to GPTS-functionalized glass showing 20 μm squares (10% protein-coated area). The roman numeral and the average intensity ratio between inside and outside micropatterned regions are also shown. (E), (F) Micropatterning showing 20 and 5 μm side squares (20% and 10% protein-coated area), respectively; the arrow indicates regions of high intensity and non-defined avidin region, respectively (F). Fluorescence is from avidin-Alexa488 (1:25 mol:mol labeled to unlabelled protein ratio). Avidin was added at 1 mg/mL concentration. 36

Figure 3.7 – Protocol used to create an avidin micropatterning using biotinylated BSA. A clean glass coverslip (1) was subject to photoresist spin-coating (2). A laser working at 405 nm irradiated regions to be later immobilized with avidin, pre-defined by a virtual mask (3) and photoresist developer selectively removed irradiated regions, exposing the glass underneath (4). An aqueous solution of BSA-Biotin was then added to the glass slides for adsorption (5), followed by an aqueous solution of avidin, which adsorbed on the surface, photoresist and/or bound to BSA-biotin (6). Finally, an acetone squirt removed the photoresist containing adsorbed BSA-biotin with bound avidin, leaving discrete regions of BSA-biotin-avidin complex immobilized on glass (7). 37

Figure 3.8 – Avidin micropatterning on glass. (A) Micropatterned surface after avidin addition and before acetone washing. Region 1 shows the numeral that identifies which pattern, out of nine possible patterns, was under observation. Region 2 shows the pattern, which is made of 20 μm squares; total protein-coated area is 50%. Region 3 represents the area outside the patterns, which was filled with photoresist and adsorbed BSA-biotin-bound avidin that would later be removed. Fluorescence can be seen everywhere, which indicates successful avidin immobilization on the surface. (B) Avidin micropatterning after acetone washing. Regions 1, 2 and 3 depicted are the same

as in (A), except now BSA-biotin-bound avidin adsorbed onto photoresist got lifted-off and Alexa488 fluorescence revealed a well-defined avidin micropatterning. (C) Avidin micropatterning showing 20 μm squares (50% protein-coated area). (D) Avidin micropatterning showing 10 μm squares (50% protein-coated area). (E) Avidin micropatterning showing 5 μm squares (20% protein-coated area). Fluorescence is from avidin-Alexa488 (1:12 mol:mol). (F) Avidin-Alexa488 emission spectrum measured inside and outside avidin-enriched regions ($\lambda_{\text{em peak}} \approx 520 \text{ nm}$); ratio of average fluorescence intensities inside and outside the same regions is also shown. BSA-biotin and avidin were added at 0.1 and 1 mg/mL concentration, respectively..... 39

Figure 3.9 – Biotin-fluorescein binding to avidin after standard micropatterning fabrication. (A) Avidin micropatterning revealed after biotin-fluorescein. The roman numeral which identifies which pattern, out of nine possible patterns, is under observation is shown on the left. (B), (C) Avidin micropatterning showing 20 μm and 10 μm side squares (20% total protein-coated area), respectively. (D) Bar plot showing normalized fluorescence intensity \pm standard deviation for a control (non-micropatterned BSA-biotin and avidin-coated glass coverslip), for a control after acetone washing and inside and outside micropatterned regions. Fluorescence intensity from the controls was collected from different areas of the coverslip surface and averaged from at least 3 representative images of the surface; in the micropatterned samples, it was collected from several ROIs defined either inside or outside avidin-enriched regions – all intensities were normalized for the maximum fluorescence observed. Fluorescence is from biotin-fluorescein, which was added to the coverslips at 50 $\mu\text{g/mL}$ concentration. Unlabeled BSA-biotin and avidin were added at 0.1 mg/mL concentration. 41

Figure 3.10 – Liquid phase separation in glass supported lipid bilayers containing ternary mixture of POPC, Chol and PSM. (A) L_o phase as revealed by the signal of NBD-DPPE. NBD-DPPE partitions between both L_o/L_d phase, although its content is higher in L_o phase as evidenced by L_o/L_d intensity ratios. (B) L_d phase as revealed by the signal from Rhod-DOPE. Rhod-DOPE partitions mostly into L_d phase, as evidenced by L_d/L_o intensity ratios. (C) Overlay of NBD-DPPE and Rhod-DOPE signals, showing L_o (green) and L_d (red) phase coexistence. NBD-DPPE and Rhod-DOPE were used at 1:200 mol:mol and 1:500 mol:mol labeled to unlabeled lipid ratio. 42

Figure 3.11 – Effect of avidin micropatterning on glass in the formation and organization of supported lipid bilayers from SUVs composed of a ternary mixture of POPC, Chol and PSM. (A),(B),(C) NBD-DPPE, Rhod-DOPE and avidin-Alexa350 fluorescent signal, respectively, with ternary control mixture (in the absence of DOPE-cap-biotin). Each of the corresponding intensity ratio between inside and outside avidin-enriched regions is shown. By comparing the different signals, we can observe that NBD-DPPE co-localized with avidin micropatterning; Rhod-DOPE was partially excluded from avidin-enriched regions. (D),(E),(F) NBD-DPPE, Rhod-DOPE and avidin-Alexa350 fluorescent signal, respectively, with ternary mixture containing DOPE-cap-biotin. Each of the corresponding intensity ratio between inside and outside avidin-enriched regions is shown. We observed that NBD-DPPE co-localized again with avidin micropatterning; Rhod-DOPE shifted towards avidin-enriched regions when compared with control experiment. Fluorescence is from NBD-DPPE (1:200 mol:mol), Rhod-DOPE (1:500 mol:mol) and avidin-Alexa350 (1:25 mol:mol). (G), (H)

Correlation plot showing normalized fluorescence intensity of NBD and Rhod versus alexa350 fluorophores, respectively, each in the absence and presence of biotinylated lipid. Each point represents a ROI defined only on avidin-enriched regions; a minimum of 40 ROIs per plot were defined this way. BSA-biotin was added at 0.1mg/mL and avidin at 1 mg/mL. Avidin micropatterning was fabricated according to section 3.1.4. 44

Figure 3.12 – Effect of BSA coating on the formation of glass supported lipid bilayers from POPC SUVs (in the absence of biotinylation). (A), (B), (C) Fluorescence recovery after photobleaching experiment onto glass supported lipid bilayer for control sample (not blocked with BSA) showing pre-bleach, bleach and post-bleach phase, respectively. (D), (E) FRAP curves (normalized fluorescence intensity over time) obtained for NBD-DPPE and Rhod-DOPE respectively, showing the recovered diffusion coefficient D and mobile fraction M_f for each. (F), (G) Fluorescence across the glass surface blocked with BSA. Small independent patches of lipid membranes were observed and confirmed by FRAP experiments. (H), (I), (J) FRAP experiment performed on the borders of a membrane patch, showing NBD-DPPE pre-bleach, bleach and post-bleach phases respectively; recovery was observed only inside the bright patch. In either confocal imaging or FRAP experiments, Fluorescence is from NBD-DPPE. NBD-DPPE or Rhod-DOPE were used at 1:200 mol:mol or 1:500 mol:mol labeled to unlabeled lipid ratio. BSA was added at 0.1 mg/mL concentration. 48

Figure 3.13 – Effect of avidin micropatterning on the formation of supported lipid bilayers from POPC SUVs (in the absence of biotinylation). (A), (B), (C) Avidin micropatterning showing NBD-DPPE fluorescent signal, avidin-Alexa350 fluorescent signal and overlay between the two for the sample not blocked with BSA; exclusion of NBD-DPPE from avidin-enriched regions was observed. (D), (E), (F) Avidin micropatterning showing NBD-DPPE fluorescent signal, avidin-Alexa350 fluorescent signal and overlay between the two for the sample blocked with additional 0.1 mg/mL BSA; NBD-DPPE signal is enriched in avidin-enriched regions. (G), (H) FRAP curve (normalized fluorescence over time) for NBD-DPPE outside the avidin-enriched regions (in glass) for the sample not blocked with BSA and inside avidin-enriched regions in BSA-blocked sample, respectively. Diffusion coefficient D and mobile fraction M_f are also shown. NBD-DPPE and avidin-Alexa350 were used at 1:200 and 1:12 labeled to unlabeled lipid and protein ratio, respectively. Avidin pattern was fabricated according to section 3.1.4., Figure 3.17. BSA-biotin and avidin were added at 1 mg/mL concentration and BSA was added at 0.1 mg/mL concentration. 51

Figure 3.14 – Effect of temperature in the formation of supported lipid bilayers from POPC SUVs containing biotinylated lipid onto BSA and BSA-biotin/avidin coated glass substrate. (A) Rhod-DOPE fluorescence in BSA-coated surface at room temperature (25°C). (B) Rhod-DOPE fluorescence in BSA-coated surface at 60°C. (C) Rhod-DOPE fluorescence in glass surface blocked with BSA-biotin plus avidin at 25°C. (D) Rhod-DOPE fluorescence in glass surface blocked with BSA-biotin plus avidin at 60°C. (E) FRAP experiment performed on a lipid membrane patch in BSA-coated surface at 60°C. (F) FRAP experiment performed on BSA-biotin and avidin-coated surface at 60°C and the corresponding Rhod-DOPE diffusion coefficient D and mobile fraction M_f ; FRAP curve is not

shown. Both in (E) and in (F) a representative image of pre-bleach, bleach and post-bleach phase are shown. Rhod-DOPE and DOPE-cap-biotin were used at 1:500 and 1:1000 labeled to unlabeled lipid ratio, respectively. Unlabeled BSA, BSA-biotin and avidin were added at 1 mg/mL concentration..... 52

Figure 3.15 – Effect of PEG in the formation of supported lipid bilayers from POPC SUVs containing biotinylated lipid onto BSA-biotin and avidin-coated glass coverslips. (A) Rhod-DOPE fluorescence in glass substrate coated with BSA-biotin and avidin, without PEG incubation (control). (B) Rhod-DOPE fluorescence in glass substrate coated with BSA-biotin and avidin, after 5 minutes of incubation with PEG. (C) Rhod-DOPE fluorescence in glass substrate coated, after 10 minutes of incubation with PEG. (D) Rhod-DOPE fluorescence in glass substrate coated with BSA-biotin and avidin, after 20 minutes of incubation with PEG. The marked spot is the bleaching spot after FRAP experiment, showing no fluorescence recovery. Rhod-DOPE and DOPE-cap-biotin were used at 1:500 and 1:1000 labeled to unlabeled lipid ratio, respectively. BSA, BSA-biotin and avidin were added at 1 mg/mL concentration..... 54

Figure 3.16 – Formation of supported lipid bilayer from GUVs containing a mixture of POPC, biotinylated lipid (DOPE-cap-biotin) and either NBD-DPPE or Rhod-DOPE as a membrane marker, in Ibidi glass bottom slides. (A) XY slice of a GUV labeled with NBD-DPPE in Ibidi uncoated glass slides. (B) XY slice of a GUV labeled with Rhod-DOPE in Ibidi uncoated glass slides. (C) XZ image sequence over time showing an immobilized GUV labeled with NBD-DPPE adhered to Ibidi glass bottom slides coated with BSA-biotin and avidin. After some time, the vesicle collapsed and formed a supported lipid bilayer. (D) XY slice of GUVs labeled with Rhod-DOPE in Ibidi glass bottom slides coated with BSA. (E) XY slice of GUVs labeled with Rhod-DOPE in Ibidi glass bottom slides coated with BSA-biotin and avidin; some of the GUVs collapsed and formed supported lipid bilayers. (F) FRAP experiment performed onto a SLB formed by GUV collapse; the FRAP curve (normalized fluorescence intensity over time) and the correspondent diffusion coefficient D and mobile fractions M_f are shown on the right. NBD-DPPE, Rhod-DOPE and DOPE-cap-biotin were used at 1:200 mol:mol, 1:500 mol:mol and 1:1000 mol:mol labeled to unlabeled lipid ratio. Unlabeled BSA, BSA-biotin and avidin were added at 1 mg/mL concentration..... 57

Figure 3.17 – POPC GUVs concentration in different volume fractions collected from an 8 mL glucose solution. (A) Representative image of the top fraction corresponding to the first 2 mL (8 – 6 mL). (B) Representative image of the fourth fraction from the top (2 – 1mL). (C) Representative image of the fifth fraction from the top (1 – 0.5 mL). (D) Representative image of the bottom fraction, corresponding to the last 500 μ L (0.5 – 0 mL) fraction. Fluorescence is from Rhod-DOPE (1:500 mol:mol labeled to unlabeled lipid ratio). (E) Bar plot showing the average normalized fluorescence intensity \pm standard deviation for each collected fractions. Intensities were obtained from at least three representative images of each fraction and normalized to the maximum fluorescence intensity observed..... 58

Figure 3.18 – Formation of supported lipid bilayers from POPC GUVs onto BSA-biotin/avidin-coated Ibidi glass bottom slides by osmotic shock induction. (A) GUVs labeled with Rhod-DOPE (red) or NBD-DPPE (green) before osmotic shock; most GUVs were immobilized in the surface. (B)

GUVs labeled with Rhod-DOPE (red) or NBD-DPPE (green) after osmotic shock. SLBs were formed from vesicles after collapse had been induced by osmotic shock. (C) NBD-DPPE channel showing SLBs formed from GUVs after osmotic shock. (D) Rhod-DOPE channel showing supported lipid bilayer formed from GUVs after osmotic shock. (E) Overlay between NBD-DPPE and Rhod-DOPE channels. (F), (G) FRAP experiments on SLB formed by GUV labeled with NBD-DPPE or Rhod-DOPE, showing a representative image of both bleach and post-bleach phase. FRAP curves (normalized fluorescence intensity over time) below show diffusion coefficients D and fluorophore mobile fractions M_f . NBD-DPPE and Rhod-DOPE were used at 1:200 mol:mol and 1:500 mol:mol labeled to unlabeled lipid ratio. Unlabeled BSA-biotin and avidin were added at 1 mg/mL concentration. 61

Figure 3.19 – Formation of supported lipid bilayers from POPC GUVs onto micropatterned and non-micropatterned avidin-coated glass coverslips. (A), (B) GUVs onto glass coverslips coated with BSA-biotin and avidin before and after osmotic shock, respectively. (C), (D) GUVs onto glass coverslips micropatterned with avidin before and after osmotic shock, respectively. The xy plane shown is above the surface and the micropatterning is not visible (E), (F) Overlay channels (Rhod-DOPE at red + avidin-Alexa350 at green), showing GUVs onto avidin micropatterning, after osmotic shock; an SLB formed from GUV collapse is shown in (E). Fluorescence is from avidin-Alexa488 and Rhod-DOPE, which were used at 1:25 mol:mol and 1:500 mol:mol labeled to unlabeled protein and lipid ratio, respectively. Avidin pattern was fabricated according to section 3.1.4., Figure 3.17. BSA-biotin and avidin were added at 1 mg/mL concentration. 62

Figure 3.20 – Effect of acetone washing in the formation of supported lipid bilayers from POPC GUVs in Ibidi glass slides. (A), (B) GUVs (red) in a BSA-biotin and avidin-coated glass (green) not exposed and exposed to acetone, respectively. SLBs were observed even before osmotic shock induction; the lower part of the GUVs (lower hemisphere) is pointed out in the picture. (C), (D) GUVs (red) in a BSA-biotin and avidin-coated glass (green) not exposed and exposed to acetone, respectively, after osmotic shock induction in order to form SLBs. While most GUVs collapsed on the control (not exposed to acetone), in the sample washed with acetone practically no SLBs were detected. Avidin-Alexa488 and Rhod-DOPE were used at 1:25 mol:mol and 1:500 mol:mol labeled to unlabeled protein and lipid ratio, respectively. BSA-biotin and avidin were added at 0.1 mg/mL concentration. 64

LIST OF ABBREVIATIONS

ABP – Actin-binding protein	N-WASP - Neuronal Wiscott-Aldrich Syndrome protein
AFM – Atomic force microscopy	PC – Phosphatidylcoline
Arp2/3 - Actin-related protein 2/3	PDMS - Polydimethylsiloxane
BSA – Bovine serum albumin	PE – Phosphatidylethanolamine
BSA-biotin - Biotin-labeled bovine serum albumin	PEG - Polyethylene glycol
Chol – Cholesterol	PG – Phosphatidylglycerol
DAG - Diacylglycerol	PH – Pleckstrin homology
DOPE - 1,2-dioleoyl- <i>sn</i> -glycero-3-phosphoethanolamine	PI - Phosphatidylinositol
DOPE-cap-biotin - 1,2-dioleoyl- <i>sn</i> -glycero-3-phosphoethanolamine- <i>N</i> -(cap biotiny)	PIP₂ – Phosphatidylinositol 4,5-bisphosphate
DRM – Detergent-resistant membranes	PIP₃ - Phosphatidylinositol 3,4,5-triphosphate
E-beam – Electron-beam	PM – Plasma Membrane
ECM – Extracellular matrix	POPC - 1-palmitoyl-2-oleoyl- <i>sn</i> -glycero-3-phosphocholine
ERM – Ezrin, radixin, moesin	POPS - 1-palmitoyl-2-oleoyl- <i>sn</i> -glycero-3-phosphoserine
FCS – Fluorescence correlation spectroscopy	PS – Phosphatidylserine
FERM - Four-point one, ezrin, radixin and moesin	PSM - <i>N</i> -palmitoyl- <i>D</i> -erythro-sphingosylphosphorylcholine
FRAP – Fluorescence recovery after photobleaching	QCM-D – Quartz crystal microbalance with dissipation
FRET – Förster resonance energy transfer	Rhod-DOPE - 1,2-dioleoyl- <i>sn</i> -glycero-3-phosphoethanolamine- <i>N</i> -(lissamine Rhodamine B sulfonyl)
GPI – Glycosylphosphatidylinositol	ROI – Region of interest
GPTS - 3-glycidyloxypropyl trimethoxysilane	SM – Sphingomyelin
GPMV – Giant plasma membrane vesicle	SPT – Single particle tracking
GUV – Giant unilamellar vesicle	STED – Stimulated emission depletion
HDMS – Hexamethyldisilazane	SLB – Supported lipid bilayer
IP₃ - Inositol 1,4,5-triphosphate	SPR – Surface plasmon resonance
L_d – Liquid-disordered	SUV – Small unilamellar vesicle
L_o – Liquid-ordered	TCR – T cell receptor
LUV – Large unilamellar vesicle	TIRFM – Total Internal Reflection Fluorescence Microscopy
MARCKS - myristoylated alanine rich C-kinase substrate	Ti:Sa – Titanium:Sapphire
MLV – Multilamellar vesicle	TM – Transmembrane
NBD – <i>n</i> -(7-nitrobenz-2-oxa-1,3-diazol-4-yl)	WASP - Wiscott-Aldrich Syndrome protein
NBD-DPPE - 1,2-dipalmitoyl- <i>sn</i> -glycero-3-phosphoethanolamine- <i>N</i> -(7-nitro-2-1,3-benzoxa-diazol-4-yl)	WAVE – WASP-family verprolin-homologous protein
NMR – Nuclear magnetic resonance	
NSOM - Near-field scanning optical microscopy	

1. INTRODUCTION

1.1. PLASMA MEMBRANE - CYTOSKELETON INTERACTIONS

1.1.1. The plasma membrane

The plasma membrane (PM), or cell membrane, is present in all cells, not only delimiting the extracellular from the intercellular space and environment, but playing an important role in a variety of biological processes. The detailed study and elucidation of PM structure has been a concern for almost a century. In 1925, Gorter and Grendel proposed that the cell membrane basic structure was one of a lipid bilayer (1). Later, in 1972, Singer and Nicholson suggested the fluid mosaic model, postulating that the PM behaved like a fluid constituted both by lipids and proteins distributed so as to minimize free energy, which despite some inaccuracies which will be later stressed out, has proved to be a valuable model (2).

Concerning the PM constituents, lipids are amphipathic molecules containing both a hydrophobic and a hydrophilic moiety, and represent the major component of PMs, greatly contributing to the formation of the ubiquitous bilayer structure (3). Eukaryotic PM lipids include (i) glycerophospholipids, such as phosphatidylethanolamine (PE), phosphatidylglycerol (PG), phosphatidylserine (PS), phosphatidylcholine (PC) and phosphatidylinositol (PI) (4); (ii) sphingolipids, such as ceramide and sphingomyelin (SM); (iii) sterols, with cholesterol (Chol) being the sole and very important sterol in mammalian cells (Figure 1.1) (3, 5). Most studies suggest that the lipid distribution across the bilayer is asymmetric, with PC and sphingolipids predominantly occupying the outer leaflet and PE, PS, PI and Chol the inner, cytosolic leaflet; moreover, there seems to be cross-talk between glycerophospholipids and sphingolipids to maintain this asymmetry (6). The lipid diversity is thought to be important to maintain homeostasis, since the PM is able to keep up with changes in metabolite concentrations, pH or temperature without being damaged or disrupted (7). Concerning membrane proteins, these may be either: intrinsic or integral, embedded in the fluidic bilayer by strong hydrophobic interactions with the lipids; extrinsic, or peripheral, bound to the membrane by weak interactions or glycosylphosphatidylinositol (GPI) anchor, palmitoyl, myristoyl moieties, etc (3, 8). Membrane proteins are important to organize lipid distribution, since lipids with length that best match the transmembrane (TM) domain of intrinsic proteins are more likely to be found in protein-lipid interface (9). Furthermore, Chol is known to increase stiffness and thickness of PM, allowing for protein sorting and interaction with possible structural and regulatory implications (3, 7, 10). The

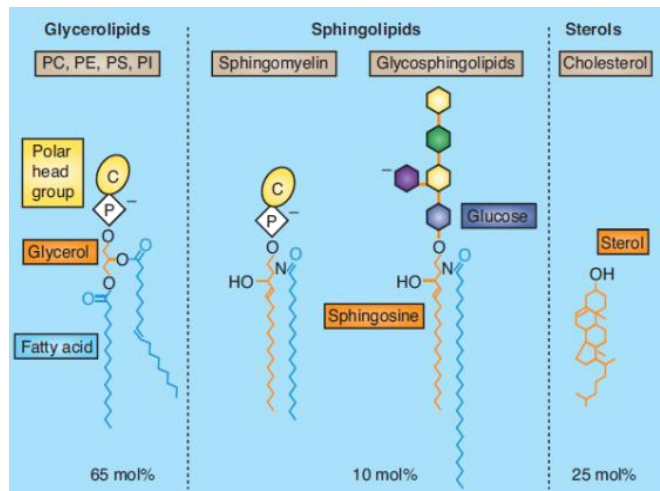


Figure 1.1 - Representation of the three classes of lipids present in the plasma membrane of mammals. The quantities of each class of lipid, in percentage of total lipid, are displayed below each category. Adapted from (4).

interplay between the lipid and proteins of the PM is thought to play a crucial role in cell polarity, vesicular trafficking, extracellular matrix (ECM) interactions and signaling through the formation of specific lipid domains called membrane rafts (11). In the next section we discuss what is currently known about these structures.

1.1.2. Membrane rafts

The fluid mosaic model assumes that the membrane lipids and proteins are homogeneously distributed over the bilayer – however, lateral lipid segregation was shown to exist in membrane model systems (12), and nowadays a more refined view suggests that small lateral heterogeneities, or lipid/membrane rafts, exist in the cell membrane (Figure 1.2) (8, 13, 14). The concept of membrane raft came about after the discovery that glycosphingolipids cluster in the Golgi apparatus before being sorted to the apical membrane of polarized MDCK epithelial cells (15). Following this discovery, other studies showed the existence of membrane structures which were insoluble in nonionic detergent Triton X-100 at 4°C, called detergent-resistant membranes (DRM), rich in Chol, GPI-anchored proteins and glycosphingolipids (16). Due to the controversy that DRMs might be an experimental artifact and not membrane raft structures (17), detergent-free studies were carried out, including (i) electron microscopy observations of antibody-labeled raft antigens; (ii) drag measures of antibody-bound raft proteins; (iii)

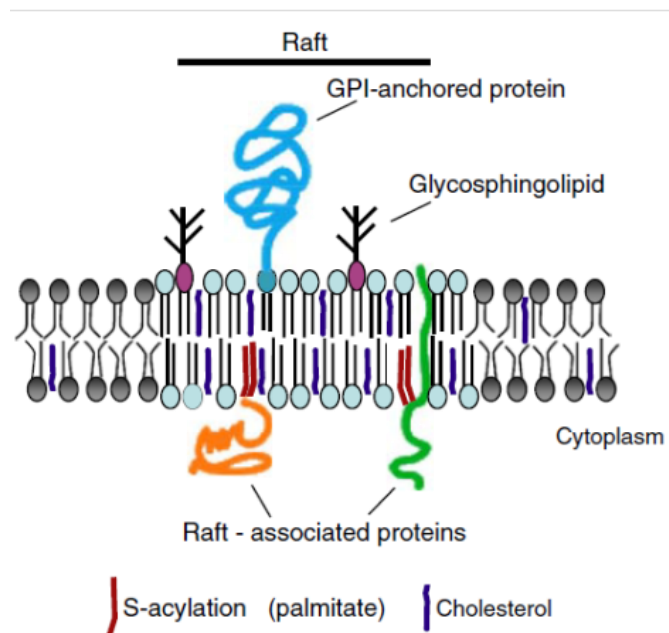


Figure 1.2 - Membrane raft model. Cholesterol associations with other lipids, such as sphingolipids, generate a discrete lipid compartment or domain with unique physical and biological properties. Cholesterol confers an ordering on the lipids that imparts changes in physical properties of the bilayer, including increased thickness and stiffness. Through poorly understood mechanisms, the rafts are coupled across the bilayer. Proteins that prefer an ordered lipid environment associate with the domains, often through a discrete targeting signal. A frequent raft signaling for proteins is palmitoylation of a membrane-proximal cysteine. Rafts are also enriched in GPI-anchored proteins. The blue and grey lipids represent “raft” and “non-raft” respectively. Adapted from (138).

single-particle tracking (SPT), fluorescence correlation spectroscopy (FCS) and Förster resonance energy transfer (FRET) measurements of GPI-anchored proteins; (iv) more recently, stimulated emission depletion (STED), near-field scanning optical microscopy (NSOM) and atomic force microscopy (AFM) measurements. These studies corroborated the existence of nanoscale assemblies of GPI-anchored proteins, cholesterol and sphingolipids in biological membranes (Figure 1.3 - A) (3,

18). In many cases, cytoskeleton proteins such as actin, myosin and ezrin were implicated in the formation of these heterogeneities; we concern ourselves with the cytoskeleton later in this work. At the 2006 Keystone Symposium, membrane rafts were defined: “Membrane rafts are small (10 - 200 nm), heterogeneous, highly dynamic, sterol- and sphingolipids-enriched domains that compartmentalize cellular processes. Small rafts can sometimes be stabilized to form larger platforms through protein-protein and protein-lipid interactions” (19). Throughout this discussion, the term “membrane raft” is used to designate the more commonly known term “lipid raft” – this is preferable since both lipids and proteins are known to play an important role. Membrane rafts are essential for processes such as vesicular trafficking, endocytosis and signaling (13, 17). These functions are thought to be played out by coalescence of the dynamic nanoscale rafts into larger raft domains by specific lipid and proteins interactions, with little or no energy input (Figure 1.3 - B) (3, 18, 20). In fact, during clathrin-independent endocytosis, multimerization was shown to promote GPI-anchored proteins sorting to Chol- and sphingolipid-enriched regions; this type of endocytosis depends on cholesterol-binding protein caveolin, forming caveolae (11). In addition, energy-independent membrane invaginations were promoted by clustering of GM₁ receptor by multivalent binding of cholera toxin (18). This coalescence also occurs in the formation of the immunological synapse, which doesn't involve the formation of caveoli. In B cells, antigen binding leads to association of B cell receptor with signaling effector Lyn kinase. In T cells, raft components of the T cell receptor such as GPI-anchored protein Thy-1 are trapped in clusters, leading to the accumulation of Chol, sphingolipids and saturated long-chain phosphatidylcholine in the synapse, separating this major cluster from the remaining membrane rich in unsaturated glycerophospholipids; cytoskeleton proteins have shown to be necessary in this process (18, 21). Indeed, these raft regions in biological membranes can be related to what happens with *in vitro* model systems. The next section details the current understanding of the principles underlying phase separation in membrane model systems and their relation to membrane rafts.

1.1.3. Phase separation in lipid membranes

Artificial liposomes are often used as model systems of biological membranes, containing simple lipid mixtures which allow tight control of membrane properties by temperature and lipid composition. Liquid phase coexistence in membrane model systems occurs in mixtures containing Chol and two types of lipid: one with a high gel-fluid and one with a low gel-fluid transition temperature (22, 23). In many cases, phase separation is known to be caused by Chol rigid sterol rings which favor interactions with saturated, stiffer hydrocarbon chains and disfavors interactions with unsaturated ones. This, in turn, promotes increased membrane thickness and phase segregation with formation of a liquid-ordered (L_o) phase and a liquid-disordered (L_d) phase (12).

Due to their biological relevance, one of the most used ternary lipid mixtures contains unsaturated phosphatidylcholine, sphingomyelin and Chol, for which boundaries and compositions are already well

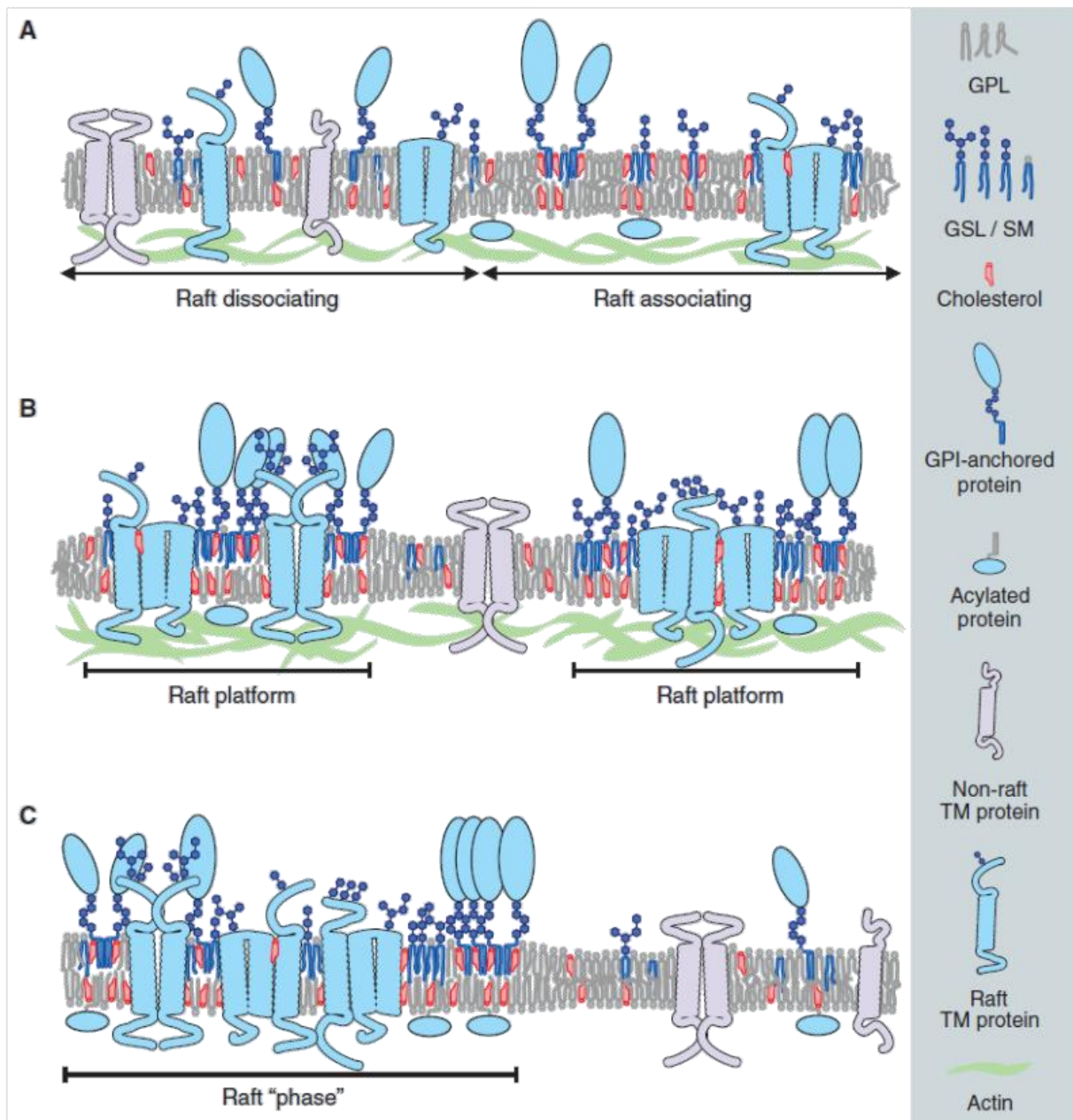


Figure 1.3 - Hierarchy of raft-based heterogeneity in cell membranes. (A) Fluctuating nanoscale assemblies of sterol- and sphingolipids-related biases in lateral composition. This sphingolipids/sterol assemblage potential can be accessed and/or modulated by GPI-anchored proteins, certain TM proteins, acylated cytosolic effectors and cortical actin. Gray proteins do not possess the chemical or physical specificity to associate with this membrane connectivity and are considered non-raft. GPL, glycerophospholipids; SM, sphingomyelin. (B) Nanoscale heterogeneity is functionalized to larger levels by lipid- and/or protein-mediated activation events (e.g., multivalent ligand binding, synapse formation, protein oligomerization) that trigger the coalescence of membrane order-forming lipids with their accompanying selective chemical and physical specificities for protein. This level of lateral sorting can also be buttressed by cortical actin. (C) The membrane basis for heterogeneity as revealed by the activation of raft phase coalescence at equilibrium in giant plasma membrane vesicles (GPMVs). Separated from the influence of cortical actin and in the absence of membrane traffic, multivalent clustering of raft lipids can amplify the functional level to a microscopic membrane phase. Membrane constituents are laterally sorted according to preferences for membrane order and chemical interactions. Adapted from (18).

described (24); in general, these lipid mixtures tend to mimic the lipid composition of the outer membrane leaflet (25). Though a deeper understanding is needed, it is thought that sphingolipids tend

to associate with Chol in L_o phase due to (i) long and saturated hydrocarbon chains; (ii) highly polar and hydrated head groups which are able to increase associative potential with Chol and other sphingolipids (5, 18). Before going any further, it is crucial to point out that while membrane model systems are in thermodynamic equilibrium, the same is not true for biological membranes, which are constantly deviating from equilibrium by processes such as vesicular trafficking and cytoskeleton interactions (26). Thus, one needs to be wary when relating results *in vitro* to phenomena occurring *in vivo*. Likewise, the terms L_o and L_d only apply to membrane model systems where physico-chemical properties of lipid phases are known and diffusional parameters may be accurately accessed (14, 18). According to the fluid mosaic model, phase separation was not thought to be possible in cell membranes due to the complexity and diversity of its components; however, the underlying principles of L_o/L_d phase separation *in vitro* are now thought to be similar to what happens in biological membrane rafts. Next, we give an overview of some important studies on membrane model systems and its implications to living cells.

By 1999, studies with ternary mixture GUVs using confocal microscopy and fluorescence correlation spectroscopy have allowed for the first time the imaging and characterization of L_o and L_d phases (27). Later, GUVs containing a single-phase lipid composition and GM₁ receptors were shown to undergo large-scale phase separation after cholera toxin binding (28). In more advanced studies using giant plasma membrane vesicles (GPMVs) - cells treated with paraformaldehyde and dithiothreitol in order to separate the cell membrane from cytoskeleton and cell trafficking influence – showed that membranes displayed Chol-dependent coalescence of GM₁ receptors by cholera toxin at 37°C, with formation of micrometer-sized L_o -like phase (Figure 1.3 - C); in this case, TM proteins were incorporated in the L_o -like phase domains, even though at an inferior ordering level than observed in membrane models (29, 30). Temperature studies with GPMVs highlighted that these membranes seemed to be made up of a single phase at high temperatures, but separated into two coexisting L_o - and L_d -like phases below a miscibility transition temperature T_{mix} ; remarkably, TM proteins were excluded from L_o -like regions (31). In an important study, it was revealed that GPMVs undergo critical fluctuations near T_{mix} (32) (Figure 1.4), similarly to ternary mixture GUVs and SLBs prepared with critical composition (33, 34). In the theory of critical phenomena, at low-temperature, domain line tension (positive free energy per unit length along the phase boundary) is high, resulting in large circular, smooth domains – naturally, this line tension depends on the mismatch between the thickness of the two phases, which ultimately depends on lipid composition (35). As temperature

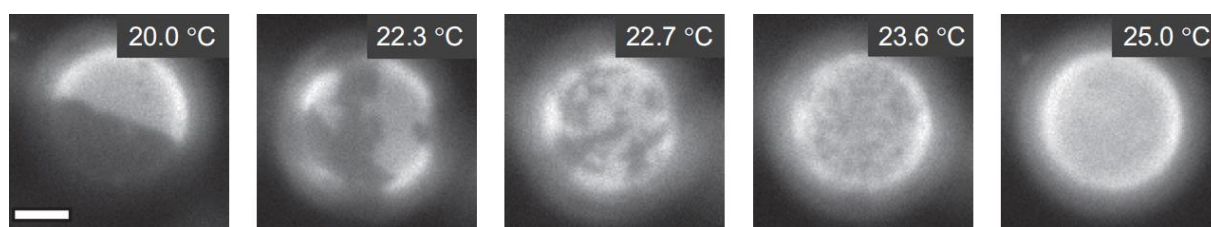


Figure 1.4 – Transition temperature and critical fluctuations in GPMVs. GPMVs are uniform at high temperature and contain two coexisting liquid phases at low-temperature. GPMVs undergo micrometer-scale fluctuations at temperatures just above their respective miscibility transition temperature, visualized when cells are pre-labeled with a fluorescent lipid analog. The critical temperature falls roughly between the second and third images. Scale bars are 5 μ m. Adapted from (32).

approaches the critical point, line tension decreases, domain edges become rough, the composition of the two phases becomes similar and fluctuations start to occur (36). At or near this point, these composition fluctuations occur due to thermal motions, because the energy requirement to maintain regions of different composition is minimal (33). The discovery that GPMVs have near-critical composition suggests that living cell membranes have similar compositions, and may be tuned to reside near miscibility critical points (32). These conclusions lead many authors to speculate that lateral heterogeneities in the cell membrane (at physiological temperature) could correspond to critical fluctuations with dimensions below 50 nm.

Altogether, these studies suggest that (i) membrane rafts may be nanoscale near-critical fluctuations occurring in the cell membrane at physiological temperature; (ii) although lipid-lipid interactions seem to be important in membrane organization, lipid-protein interactions and ligand binding seem to play an essential role in nanoscale raft coalescence, which occurs in important biological processes (e.g. immunological synapse) - cell membranes are poised for activation of coalescence at physiological temperature, which translates in a micrometer-scale raft phase that can occur by merging and stabilizing nanoscale rafts present in biological membranes (3, 18, 29, 30). It is worth noting that the impact of external perturbations in changing membrane properties should be much greater near the vicinity of the critical point, since energy requirements are minimum (9). In fact, studies with GUVs containing a critical composition and GPMVs adhered to a supported lipid bilayer showed large-scale arrangement and stabilization of domain structures at physiological temperatures, suggesting an important role played by adhesions on domain definition (37). In all these studies with membrane model systems, the actin cytoskeleton was absent, probably easing the formation of larger, micro-sized rafts. However, our current understanding of plasma membrane domains suggests an active role of the cytoskeleton in defining the formation of membrane rafts (3). In the next sections we detail how the cytoskeleton interacts with the cell membrane and contributes for its organization.

1.1.4. Cytoskeleton role in plasma membrane organization

The cytoskeleton is a dynamic structure that plays a fundamental role in eukaryotic cells. The hypothesis that the cytoskeleton could interact with the plasma membrane has been suggested when integral membrane proteins and cytoskeleton proteins were found to co-pellet after Triton X-100 extraction (38). Classical studies in erythrocytes, showing the existence of a 2D membrane skeleton based on spectrin and ankyrin proteins, added evidence to the idea of an interacting cytoskeleton and plasma membrane (39). Since then and until now, PM-cytoskeleton interactions have been associated with several functions such as receptor clustering, migration, shape, cell-cell and cell-ECM interactions, cell division, vesicular trafficking, endo- and exocytosis and signaling. Membrane cytoskeleton defects have also been implicated in neurological (e.g. spinocerebellar ataxia) and hematological diseases (e.g. malaria and elliptocytosis) (11, 40). The whole 3D structure of cytoskeleton has three main components (i) intermediate filaments proteins, coded by seventy different genes and five families of associated proteins; (ii) microtubule proteins, comprising six α - and β -tubulin proteins and more than a dozen associated proteins; (iii) microfilaments, or actin filaments,

with six actin proteins and seventy families of actin-binding proteins (ABP). We also have to take in account myosin and kinesin motor proteins, from microfilaments and microtubules respectively, which are coded by forty genes each. Such a large cell component has certainly potential to bind the membrane in varied ways (41). As a general rule, cytoskeleton may bind to PM by three different ways: 1) the cytoskeleton proteins may bind directly to lipid phase; 2) cytoskeleton may bind, directly or via adapter proteins, to TM proteins; 3) cytoskeleton elements may link to proteins that bind the inner leaflet of PM; this is the case for ABPs such as ezrin, radixin moesin, which link actin to phosphatidylinositol 4,5-bisphosphate (PIP₂). Tubulin was shown to associate with cell membrane fractions and lipids from purified cells, even though its role is still not clear. Intermediate filament protein vimentin has been shown to bind to ganglioside GM₂ with high affinity and to interact with purified lipid bilayers containing negatively charged lipids (41). However, up to now, cortical actin skeleton, here referred as membrane skeleton, has proved to be the most important membrane-interacting component. *In vitro* studies show that F-actin binds to lipid bilayers when characteristic inner leaflet glycerophospholipids such as PS and PE are incorporated; in addition, adsorption of this protein to liposomes containing PS and Chol altered the size of Chol-dependent lipid domains (42, 43). In another study, assembly of actin networks assisted by actin-related protein 2/3 (Arp2/3) complex and initiated by Neuronal Wiscott-Aldrich Syndrome protein (N-WASP) on vesicles with phosphatidylinositol 4,5-bisphosphate (PIP₂) lead to membrane domains coincident with sites of actin polymerization (42). Both Chol depletion and cortical actin perturbations or density changes have shown to perturb and affect the dynamics of proteins and lipids (44–46). In phagocytic cups, PIP₂ accumulation in actin-delimited regions lead to lower diffusion rate than in other membrane regions as measured by fluorescence recovery after photobleaching (FRAP); however, this was not due to electrostatic repulsions between negatively charged PIP₂ and actin, which suggests another mechanism (47). In fact, the diffusion coefficients for TM proteins and lipids in membrane, as measured by SPT, FCS and FRAP, are approximately 20-fold smaller than those found in membrane model systems. The motion of TM proteins is characterized by temporary confinement in a compartmentalized membrane region, where the molecules diffuses freely, although they can jump between compartments after some time (1 - 50ms); this results in a lower diffusion coefficient than that observed in GPMVs and artificial membranes, where simple Brownian diffusion is observed (48, 49). Conversely, other studies by SPT and optical tweezers suggest that certain TM proteins, such as E-cadherin, are practically immobile in the membrane (50). Surprisingly, lipids in both cell membrane leaflets also showed compartmentalization and intercompartmental movement, with residence time in compartments being lower than TM proteins (1 - 10ms) (51). All this evidence, added to the fact that actin cytoskeleton removal leads to increased diffusion of TM proteins and formation of L_o-like microscopic phases in GPMVs (51), lead to the fence-and-picket model which will now be discussed.

The fence-and-picket model was proposed by Kusumi and colleagues to explain how cytoskeleton organizes the PM (48, 52). The cytoskeleton below the membrane represents the fences that delimit membrane domains - inside these domains, or compartments, TM proteins are relatively free to move and collisions of the cytosolic tails with cytoskeleton keeps them corralled (Figures 1.5 - A, B). When the distance between the skeleton and the membrane is large enough, or when the skeleton is

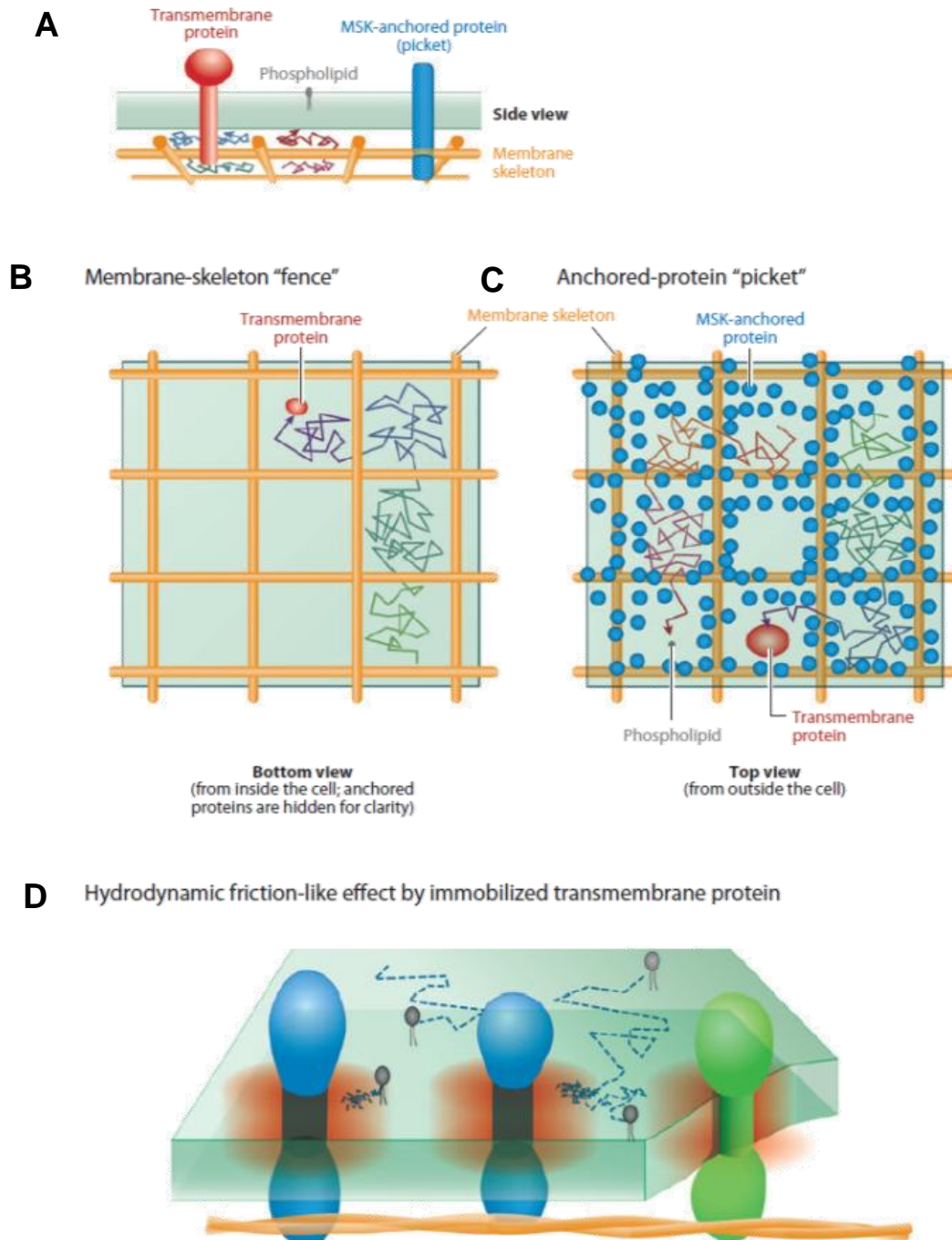


Figure 1.5 - The fence-and-picket model of membrane organization. (A) Schematic view of the plasma membrane, showing the membrane skeleton (MSK), the diffusing transmembrane (TM) protein (red), and a TM protein anchored to the MSK, acting as a picket (blue). (B) The membrane-skeleton “fence” model (the bottom view of the plasma membrane, i.e., the view from inside the cell). The plasma membrane may be partitioned into closely apposed domains (compartments) for the translational diffusion of membrane molecules. All the membrane-constituent molecules undergo short-term confined diffusion within a compartment and long-term hop movement between compartments (hop diffusion). The compartment boundaries are composed of the actin-based MSK (fence) and the TM proteins anchored to and aligned along the actin fences (pickets, including the TM proteins transiently bound to the actin fences). (D) The diffusion of molecules in the region around the immobilized TM (reddish-orange region) is slower, owing to the hydrodynamic friction-like effect at the surface of the immobilized protein. This effect could propagate over distances equivalent to multiple diameters of picket proteins. When such diffusion barriers are aligned along the membrane-skeleton fence, they form effective compartment boundaries. Adapted from (48).

temporarily removed, intercompartmental movement of TM proteins occurs, which is known as “hop diffusion”. The pickets are represented by TM proteins (Figure 1.5 - C) which are tethered to the cytoskeleton (fences) and act as a diffusional barrier to lipids by (i) steric hindrance; (ii) hydrodynamic friction-like effect, explainable because the viscosity of the fluid membrane around immobilized proteins increases and diffusion is slowed (Figure 1.5 - D). When these effects are not strong enough to corral the lipids, they move between compartments - hop diffusion. This model shows that each molecule in PM has two diffusion coefficients: one for “microscopic” diffusion within the compartments, which is close to that observed for GPMVs and artificial membranes (where the actin skeleton is absent); one for “macroscopic” diffusion across the compartments, which is 20-fold lower than the one observed in previous cases (where actin skeleton is present) (41, 48). But how does this model include membrane rafts? An extension of this model was proposed by the same authors, considering three tiers, or mesoscale domains in the fence-and-picket model:

1. Membrane compartments (Figure 1.6 - A), ranging from 40 - 300 nm diameter, which organize the PM. They are created by interaction of the actin skeleton (fences) with TM proteins (pickets). This is the most basic tier and distinguishes PM from artificial membranes.
2. Membrane raft domains (Figure 1.6 - B), enriched in Chol, sphingolipids and GPI-anchored proteins, ranging from 2 – 20 nm, although they can be as large as the apical membrane of epithelial cells. Pickets exclude Chol from its vicinity due to structural incompatibility; additionally, size of membrane rafts is limited to that of the compartments (300 nm) which suppresses raft size. This explains micro-sized raft formation in GPMVs where cytoskeleton is absent.
3. Dynamic protein complex domains (Figure 1.6 - C): complexes of membrane-associated and integral proteins, also including coat-proteins and scaffolding proteins, ranging from 3 - 10 nm. This tier can be distinguished from raft domains because in the first lipid interactions play a critical role, while in the latter protein-protein interactions dominate.

These tiers may be important for several biological functions. The first tier may allow for receptor clustering in signaling pathways. The confinement of B cell receptor within compartments was shown to be an important mechanism for suppression of the receptor diffusivity and allowing activation of B cells (48). Another function may be oligomerization-induced trapping of receptors. Immediately after activation by multivalent binding of antigens, the Fc ϵ RI receptor is immobilized; disruption of actin skeleton leads to increased diffusion of the clusters, suggesting a role in this process (53). Concerning the second and third tiers, these interact with one another: under stimulus, protein complexes (GPI-anchored or TM proteins) may coalesce by raft-based lipid interactions to form larger oligomers receptor complexes. This is thought to be what happens in the immunological synapse, where recruitment of Lyn, a raft-associated protein, was promoted after B cell receptor antigen binding; in T cells, recruitment of CD3 and CD28, together with TCR, induced raft formation at the cluster – the actin cytoskeleton enables formation of a stable IS and sustains activation of immune cells through compartmentalization (21). Other case studies where membrane raft-cytoskeleton interactions are crucial may be found in reviews (41, 48).

Before going further, it is noteworthy to say that this model is an important attempt to explain diffusion discrepancies in different studies by hypothesizing how the cytoskeleton organizes the cell membrane. Nevertheless, it does not say anything about the nature of membrane rafts inside compartments. Thus, the hypothesized critical nature of membrane rafts and the cytoskeleton fence-and-picket model are mainly complementary in our understanding of membrane dynamics. In fact, based on the fence-and-picket model, Monte Carlo simulations showed that near-critical fluctuations in the membrane lead to subdiffusion and that PM-cytoskeleton network interactions enhance phase separation at the nanoscale, prevent large-scale formation and eventually lead to lipid hop diffusion (54). Even though the biophysical community is getting closer to a minimal raft model, there is still much to be ascertained. The last section focuses on PIP_2 as an important component in PM-cytoskeleton interactions.

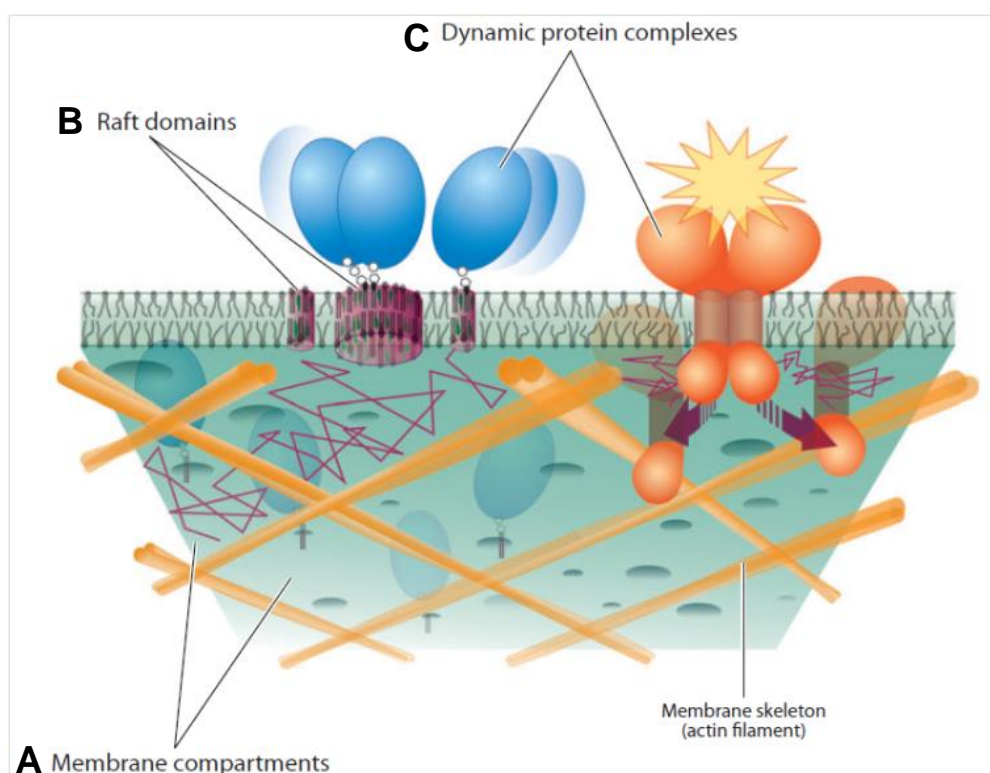


Figure 1.6 - Three-tiered hierarchical mesoscale-domain architecture of the plasma membrane. (A) Membrane compartments, generated by the partitioning of the entire plasma membrane by the membrane-associated actin-based membrane skeleton (fence) and transmembrane (TM) proteins anchored to the membrane-skeleton fence (pickets, not shown in this figure). (B) Raft domains enriched in cholesterol, glycosphingolipids and GPI-anchored proteins, with sizes limited by the membrane compartments. (C) Dynamic protein complex domain composed of dimers and greater oligomers of integral membrane proteins, which may exist only transiently. This type of domain also includes coat-protein-induced and scaffolding-protein-induced protein assemblies. Adapted from (48).

1.1.5. PIP_2 role in cytoskeleton adhesions to the plasma membrane

Phosphatidylinositol (PI) and its phosphorylated derivatives, phosphoinositides, are an important class of lipids in cell membranes, comprising about 10% of all the PM lipids. Phosphatidylinositol 4,5-

bisphosphate (PIP₂ or PI(4,5)P₂) is the most abundant PI in cell membranes (~ 1% of total PM lipids) (55). The initial interest in PIP₂ was due to its role in forming diacylglycerol (DAG), inositol 1,4,5-triphosphate (IP₃) and phosphatidylinositol 3,4,5-triphosphate (PIP₃), which are three important second messengers (56). More recently, PIP₂ has been shown to regulate cytoskeleton and membrane dynamics by (i) interacting with multiple ABPs, clathrin adapter proteins and some Rho family GTPases; (ii) indirectly regulating activity of TM proteins such as ion channels, transporters and signaling receptors. A number of diseases, including cancer, have been associated with defects of lipid kinases and phosphatases that regulate PIP₂ homeostasis (55, 56). Furthermore, studies reveal that an increase in PIP₂ levels in cells promote polymerization of actin filaments and stabilization of PM interactions; accordingly, decreasing levels of PIP₂ show decrease in actin assembly (41). Due to their relevance, we are going to focus on ABPs. Since both PIP₂ and cytoskeleton polymers have negative charge, PIP₂ doesn't interact directly with the cytoskeleton; conversely, many ABP have positively charged domains, thus can interact with PIP₂ and promote a multiplicity of processes (Figure 1.7). Some of these interactions take place via canonical phosphoinositide-binding domains such as PH, PTB, PX, FYVE (Fab1, YOTB, Vac1 and EEA1) and FERM (four-point one, ezrin, radixin and moesin); others use noncanonical motifs (55). ABPs involved in actin filament nucleation include WASP, N-WASP and WASP-family verprolin-homologous protein (WAVE), regulators of Arp2/3 complex which promotes growth and branching of actin networks. These ABPs are activated upon PIP₂ binding to its NH₂-terminal basic motif, activating Arp2/3 (55). Actin depolymerizing factors,

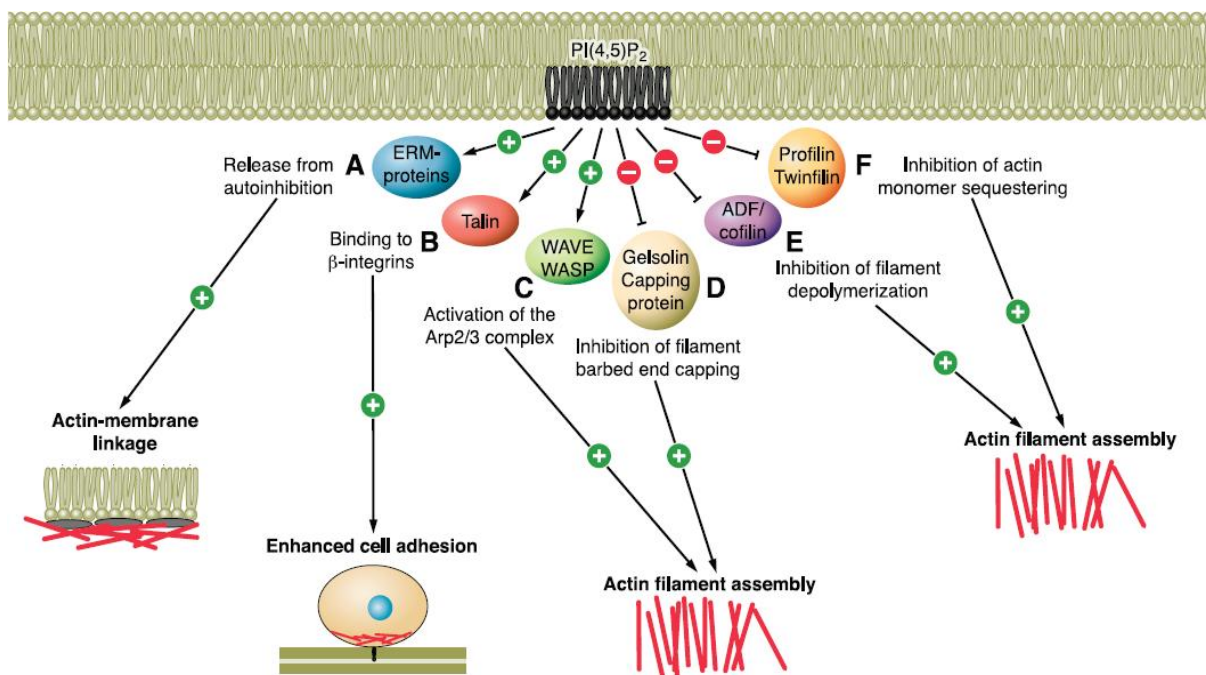


Figure 1.7 - Regulation of actin-binding proteins by PIP₂. Local increase of PIP₂ concentration affects many aspects of the actin cytoskeleton. (A) Plasma membrane - actin cytoskeleton interactions are enhanced through the activation of ERM-family proteins. (B) Cell adhesion to the extracellular matrix (ECM) is increased by enhancing the binding of talin of β-integrins. (C) The activity of WASP and WAVE family proteins is enhanced by PIP₂. These proteins promote Arp2/3-mediated actin filament assembly. (D) Filament barbed end and capping proteins, such as gelsolin and heterodimeric capping protein, are inhibited by PIP₂. (E),(F) Actin filament disassembly and monomer sequestering are diminished through inhibition of ADF/cofilin and twinfilin by PIP₂. Adapted from (55).

ADF/cofilins, promote actin filament disassembly and severing; by high affinity-binding of cationic domains to PIP₂, these proteins are strongly inhibited and actin treadmilling is accelerated. Profilin and twinfilin may act as monomer sequestering proteins, slowing actin filament formation – this activity is thought to be inhibited when bound to the charged inositol head group of PIP₂ (55, 56). Another ABP is capping protein, which blocks the barbed ends of actin filaments and prevents addition or loss of monomers; even though the mechanism is controversial, the activity of capping protein is inhibited by PIP₂. Gelsolin superfamily include gelsolin and villin proteins which are Ca²⁺-regulated proteins and display severing and capping activities, similar to capping proteins - upon binding of PIP₂ through mechanism similar to profilin, this activity is inhibited. Talin is a cytosolic protein abundant in focal adhesion, and binds integrins, either directly or by interacting with vinculin and α -actinin. PIP₂ is a talin activator and binds its FERM domain, promoting talin binding to β -integrin resulting in cell adhesion (56). Finally, the ezrin-radixin-moesin (ERM) family of proteins directly links the cytoskeleton to the plasma membrane. All vertebrates express at least one of these proteins, which present high sequence homology (57). They provide structural reinforcement for the cell cortex and are particularly concentrated in membrane protrusions (e.g. uropods, filopodia). Previous studies have shown that both moesin and ezrin bind PIP₂-LUVs, PIP₂-GUVs, thus becoming more prone to proteolysis; this suggests a looser structure after binding to lipid membranes (58, 59). Their actin binding site is activated both by threonine phosphorylation and PIP₂ binding to FERM domain (56). ERM proteins contain the N-terminal FERM domain and a C-terminal ERMAD domain (ERM association domain), usually bound to each other in the resting state, and a linker coiled-coil region in between; following protein activation, these two dissociate and autoinhibition is released, with F-actin binding site in ERMAD being exposed (60). Recently, a detailed mechanism of how PIP₂ binds and activates moesin was suggested: FERM domain contains two PIP₂ binding sites, and PIP₂ binds transiently to a first site (PATCH) and then stably to the second (POCKET), inducing conformational activation (57). Anchoring of membrane rafts to cytoskeleton through ERM was previously shown to be a necessary condition for immunological synapse formation and T cell activation (61).

Thus, the central role that PIP₂ plays in cytoskeleton reorganization implies that its proper distribution in the PM is extremely important. There is strong evidence that regulation of PIP₂ distribution is done by providing spatio-temporal segregation of pools (62). Multiple mechanisms have been proposed for this, including the sequestering of PIP₂ through electrostatic interactions with poly-basic proteins such as myristoylated alanine rich C-kinase substrate (MARCKS) or growth-associated protein 43 (63, 64). Contrarily, other studies suggest that PIP₂ compartmentalization can be achieved simply by hydrogen bonding between head groups at or above physiological pH, without contribution from proteins (65). This last hypothesis was not supported by more recent studies showing that PIP₂ doesn't form clusters in fluid membrane model systems in pH ranges 4.8 - 8.4 (66). In another study, PIP₂ synthesis has been proved to occur within actin polymerization regions by phosphatidylinositol-4-phosphate 5-kinase (PI4P5K), which, together with MARCKS, could account for compartmentalization of PIP₂ (67). Another proposed mechanism is through association with cholesterol-enriched membrane rafts; in fact, enriched pools of PIP₂ associate with DRM upon Triton X-100 treatment (68). This is supported by studies showing that PIP₂ is enriched in sphingolipid and cholesterol membrane

rafts, mediating actin skeleton adhesions through ABP (69). Disruption of membrane rafts by depletion of cholesterol using methyl- β -cyclodextrin (M β CD) inhibited PIP₂ turnover and functions, also corroborating this hypothesis (70). Further studies with PIP₂-specific phosphatases targeted either to raft or nonraft domains of T cells provided strong evidence that PIP₂ functions in membrane rafts and is necessary in cell signaling and activation (71). These last results are difficult to explain, since PIP₂ sn2 acyl chain is most often arachidonic acid, a polyunsaturated chain which is not expected to have affinity for more ordered lipid structures such as rafts (56, 66). Also, in lipid monolayers, cholesterol-dependent L_o phase formation mainly excluded PIP₂ to the L_d phase; PIP₂ lateral organization was also dependent on Ca²⁺ (72, 73). A recent study from the host laboratory quantified the L_d/L_o partition coefficient of a PIP₂ fluorescent derivative as 3.6 in the absence of calcium and 1.9 in the presence of moderately high concentration of the divalent ion (74). These results only show that the mechanism by which PIP₂ compartmentalizes in cell membranes is still a very controversial issue.

By the end of this part review, we have an idea of some of the principles underlying the nature of membrane rafts, the role of cytoskeleton network in membrane organization and cytoskeleton adhesions to the membrane rafts. Besides all this, we now have to take into account PIP₂ adhesions through ABP at the interface of the cytoskeleton-plasma membrane interactions; the direct effect of these adhesions in defining membrane domains is still elusive. The next introductory part explores *in vitro* approaches to study the biological membrane and cytoskeleton interplay.

1.2. MEMBRANE MODEL SYSTEMS IN BIOPHYSICS

1.2.1. Membrane model systems review

One of the main goals of biophysics is to determine key parameters within a functional biological system. Due to the enormous complexity of biological structures such as cell membranes, the necessity to build a simple, cell-free, well-controlled systems is one of the main tasks of biological sciences (75). Synthetic Biology aims to build such minimal systems using “bottom-up” approaches, meaning that a synthetic cell is produced from the scratch from a pool of biological components necessary to assemble the system (76). Although this goal is far from being reached, many membrane systems produced *in vitro* from bottom-up approaches are simple enough to allow for satisfactory quantification and, at the same time, being complex enough to retain the fundamental principles of what happens *in vivo* (75, 76). Since the raft hypothesis (13), phase separation has been intensely investigated in artificial membranes as models for the plasma membrane and these model systems have been developed not only to study lipid-lipid, but lipid-protein interactions (75). We now briefly discuss three important membrane model systems: giant unilamellar vesicles, giant plasma membrane vesicles and supported lipid bilayers.

Giant unilamellar vesicles (GUVs) have about 1 – 100 μ m in diameter, and typical protocols to prepare them include 1) spreading of lipid mixtures on a platinum electrode, which is then dipped on an aqueous buffer and an electric field is applied to produce GUVs; 2) gentle hydration with charged

lipids, creating electrostatic repulsions between bilayers and allowing GUVs formation (75). GUVs have been often used to study phase behavior in binary and ternary lipid mixtures due to their large size and simple methods of preparation (77). Phase separation is often visualized by partitioning of fluorescent probes into L_o or L_d domains (78). Concerning the theme of our work, GUVs studies include: profilin interactions with PIP_2 (75); PIP_2 binding to N-WASP, which lead to activation of Arp2/3 complex and dendritic actin network formation on PIP_2 -enriched domains - this proved that this binding is necessary and sufficient to induce phase separation and actin polymerization (79). Studies with GUVs also showed that tethering these membranes to protein surfaces has the potential to reorganize the lipid domain distribution (80).

Giant plasma membrane vesicles (GPMVs) are cell membrane regions, detached from the cell cortex and absent of cytoskeleton, retaining some of the complexity of the native plasma membrane (75). Phase separation, similar to what happens in GUVs, has been described in GPMVs (29, 31). GPMVs have been shown to display robust critical behavior - when the temperature is maintained at a critical value, the line tension between coexisting domains approaches zero and composition fluctuations occur (32). How these fluctuations are related to the formation of lipid rafts is unclear, but it is likely that if the plasma membrane is close to a critical point, the sensitivity for external perturbations such as cytoskeleton interaction is greatly increased (54). The relevance of these studies has already been discussed in the section 1.1.3.

Supported lipid bilayers (SLBs) are planar membranes formed on a hydrophilic substrate, such as silica or mica, containing a very thin layer of liquid between the support and membrane (Figure 1.8) (75). Thanks to the solid support which confers high stability, controlling the conditions without affecting membrane stability is relatively easy. Another advantage of SLBs is their accessibility to surface-imaging and manipulation techniques such as Total Internal Reflection Fluorescence Microscopy (TIRFM), Surface Plasmon Resonance (SPR), Quartz Crystal Microbalance with Dissipation (QCM-D), Nuclear Magnetic Resonance (NMR), FCS and AFM (75, 78, 81). The first attempts to create SLBs used sequential transfer of monolayers from air-water interface to a solid substrate by the Langmuir-Blodgett technique (75, 82). Perhaps the easiest way to create SLBs is from adsorption and fusion of small unilamellar vesicles (SUVs) or large unilamellar vesicles

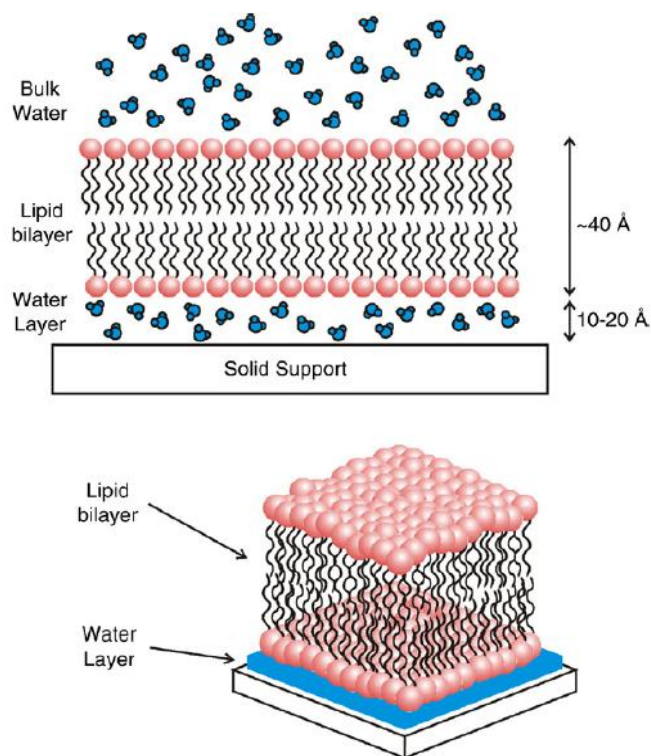


Figure 1.8 - Schematic diagram of a supported lipid bilayer. The membrane is separated from the substrate by a 10 - 20 Å thick layer of water. Adapted from (82).

(LUVs), which can be prepared via 1) sonication and ultracentrifugation of water-lipid suspensions; 2) extrusion of multilamellar vesicles (MLVs) through porous membranes, respectively (82). Electrostatic interactions, presence of divalent cations (particularly calcium) and the support itself play a role in the efficiency of the adsorption (83). SLBs are often used for surface functionalization. Biotinylated lipids can be doped in SLBs to attach to a streptavidin target (84) and form double membranes which have been used to study the neurological synapse (85). GPI-anchored proteins may also be incorporated (86). Several groups have tried to attach cortical actin skeleton to SLBs to mimic what happens *in vivo*. Ponticulin, a TM protein that anchors actin network to the cell membrane and serves as a nucleation site for actin assembly, allowed the formation of actin network bound to SLB; dissociation constants of F-actin with ponticulin were successfully determined by SPR and QCM-D (87). The incorporation of TM proteins in SLBs has been successful but leads, sometimes, to the loss of function or mobility due to interactions with the substrate; to overcome this issue, the use of polymer cushions to increase the hydration layer or long-chain tethers to the support have already been described (75, 78). In another study, a thin dendritic actin layer bound to SLBs containing PIP₂ was formed upon stimulation with actin binding proteins (N-WASP, Arp2/3, etc); after addition of frog egg extract, filopodia-like structures rose from the surface of SLBs (88). Other studies may be found in a recent review (76). The next section shows how micro and nanotechnologies may be merged with supported lipid bilayers in biology and biophysics.

1.2.2. Merging micro/nanotechnologies and biophysics

Micro- and nanotechnologies have emerged in the past two decades as forefronts in Physics, Chemistry and Biology, accompanied by the advances in fabrication and characterization of increasingly smaller structures (89). In fact, many of the micro/nanofabrication techniques have their roots in standard top-down fabrication methods developed for the semiconductor industry (90). Lithography, the cornerstone of this field, is the technique used to transfer a certain pattern onto a substrate; the most widely used is photolithography, which uses a polymeric photosensitive material, or photoresist, and a light source to create this pattern (Figure 1.9) (90). The first method of patterning SLBs was developed in 1997 using standard photolithography – patterned grids of photoresist, aluminum oxide or gold on oxidized silicon substrates were used to partition the bilayer in corrals where lipids are able to diffuse freely without trespassing the barriers (91). Patterned SLBs can also be created by selectively destroying regions with high intensity deep-UV radiation through a photomask in aqueous medium – the UV radiation creates ozone and singlet oxygen, which react with lipids to create highly localized lipid-free regions (92). Photolithography has also been used to create micropatterned avidin arrays using gold and alkanethiols functionalization (93). One technique that makes use of photolithography is the lift-off method. A thin layer of parylene is deposited on silicon and patterned by standard photolithography; after the SLBs has been formed onto it, the parylene is peeled away, leaving a patterned bilayer; this has been done down to one micron feature size (94). To study phosphotyrosine signaling, lipid dynamics and cytoskeleton transport during IgE-FcεRI binding, mast cells were transfected with green fluorescent protein (GFP)-fused Lyn kinase, membrane raft

markers or actin and the spatiotemporal organization of the plasma membrane of blast cells interacting with liftoff-patterned SLBs was observed over time by confocal microscopy (95). Electron-beam (E-beam) lithography provides higher resolutions than standard photolithography, although the latter is more simple and quick to perform (90). E-beam lithography has been used to define chromium lines, creating a diffusion barriers for lipids and proteins to (i) provide spatial control of EphA2 receptor tyrosine kinase in human breast cancer cells; (96, 97) (ii) constrain peptide-MHC and ICAM proteins to study immunological synapse formation in T cells (86). The reorganization of EphA2 receptor clusters due to chromium lines resulted in changes in actin cytoskeleton morphology, which is in agreement with what is already known (97). E-beam lithography has also been used to construct substrates bearing patterned protein ligands, allowing well-defined signals to be delivered to T cell in order to study how antigen presenting cells-derived signals influence membrane organization and TCR clustering during T cell activation (98). Using intense UV light, a biotin micropatterning was successfully produced by photodestruction of biotin molecules using a photomask (99). Soft lithography has also been used in this field - fibronectin micropatterned SLBs have been prepared by microcontact printing using a polydimethylsiloxane (PDMS) mold; PDMS has been molded against a previously lithographically patterned surface (100–102). Patterned SLBs have also been used in microfluidics; combining the small volume of microfluidics to the lateral mobility of membrane components, they can be used as biosensors (84) - these last applications are beyond the scope of our work and may be consulted in the following review (82).

While in the first section we reviewed some of the fundamental principles that underlie membrane rafts and PM-cytoskeleton interplay, in this second section we gave a bird's eye view on *in vitro* systems which are used to mimic and replicate what happens in

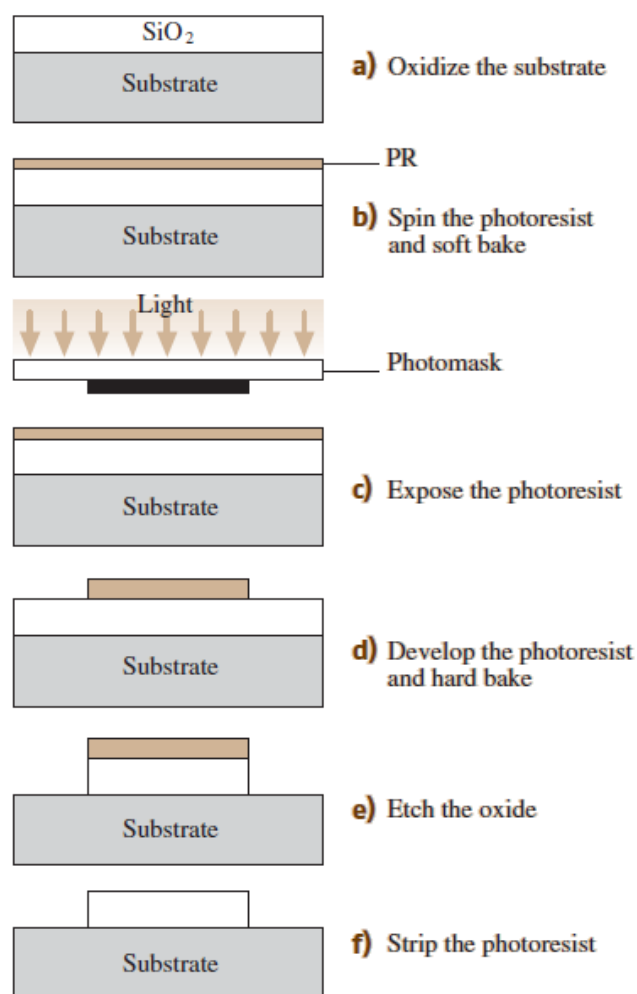


Figure 1.9 - Schematic drawing of photolithography in silicon substrate with a positive photoresist. The first step involves oxidation of the substrate for passivation, forming SiO_2 (a), followed by photoresist spin-coating and heating (b). The previously formed photomask is used to expose photoresist to light (c), which makes it soluble in the photoresist developer (d). By removing the uncovered material by etching process (e) and stripping the remaining photoresist, a pattern is created on the substrate. Adapted from (90).

biomembranes – this hard task is, to some extent, facilitated by the merging of micro and nanotechnologies.

1.3. RATIONALE AND OBJECTIVE

Our current understanding of lateral heterogeneities in the plasma membrane embraces two fundamental concepts. First, the concept of membrane rafts as near-critical composition fluctuations in the PM; the interplay between these rafts and local membrane-protein interactions (e.g. ligand binding) could result in phase separation and coalescence to form larger rafts with biological relevance. Second, the fence-and-picket model which provides a valuable framework to understand how the cytoskeleton organizes and distributes membrane heterogeneities. In the vicinity of a critical point, the presence of membrane adhesions, such as PIP₂-mediated cytoskeleton adhesions, are expected to dramatically influence phase separation, and this might be the physical basis behind the relevance of the cytoskeleton in several membrane raft-associated cellular functions. Presently, it is consensual that PIP₂ plays a crucial role in tethering actin skeleton to the plasma membrane and functions in a myriad biological processes (29, 41). More specifically, PIP₂ binds ABPs, such as ezrin, radixin and moesin, which in turn bind to actin, acting as intermediates in cytoskeleton-plasma membrane interactions (43). While most studies aiming to characterize the physical principles responsible for lateral heterogeneities in the plasma membrane have focused on spontaneous phase separation of biologically relevant lipid mixtures, still fewer studies have attempted to characterize the direct effect of cytoskeleton adhesions in detail. In face of the growing evidence in favor of the importance of the cytoskeleton in generating and defining membrane rafts, this project aimed to establish a new model system for the study of the impact of membrane adhesions on phase separation in biologically relevant lipid membranes. We expect that the development of this system, which is yet to be completed, will significantly contribute to a more comprehensive characterization of the role of PM - cytoskeleton interactions in membrane raft organization.

This model system was based on the tethering of SLBs to an avidin micropatterned glass surface through biotinylated lipid, thus mimicking, in a simple fashion, PIP₂-ERM cytoskeleton tethers. The first part of the work aimed to create an avidin micropatterning through the use of simple photolithography procedure and protein adsorption on glass substrate. In the second and third part of the work, we attempted to create SLBs containing biotinylated lipid onto the previously formed avidin micropatterning, using SUVs and GUVs respectively. SLBs were chosen as a membrane model due to their stability conferred by the solid support and compatibility with micro- and nanofabrication techniques (59). Thereafter, using a novel approach, we pretended to conclude whether or not the presence of membrane adhesions was sufficient to induce lipid domain formation and phase separation in biologically relevant membranes.

2. MATERIALS AND METHODS

2.1. MATERIALS AND REAGENTS

Microscope glass coverslips with dimensions 24 mm x 50 mm and 0.17 mm thickness were obtained from Menzel-Gläser (Braunschweig, Germany). Hydrogen peroxide, sulfuric acid, UVASOL grade ethanol and perchloric acid were obtained from Merck (Darmstadt, Germany). Avidin from egg white, bovine serum albumin (BSA), biotin-labeled bovine serum albumin (BSA-biotin), cholesterol (Chol), 3-glycidyloxypropyl trimethoxysilane (GPTS), poly (ethylene) glycol (PEG) 3400 and Biotin (5-fluorescein) were obtained from Sigma-Aldrich (St. Louis MO, USA). Avidin Alexa Fluor 488 conjugate (avidin-Alexa488), avidin Alexa Fluor 350 conjugate (avidin-Alexa350) and bovine serum albumin Alexa Fluor 594 conjugate (BSA-Alexa594) were purchased from Invitrogen (Breda, The Netherlands). PFR 7790G-27-cP positive photoresist and TMA238WA photoresist developer were obtained from JSR Micro (Leuven, Belgium). Hexamethyldisilazane (HDMS) was obtained from TCI America (Oregon, USA).

1-palmitoyl-2-oleoyl-*sn*-glycero-3-phosphocholine (POPC), *N*-palmitoyl-*D*-erythro-sphingosylphosphorylcholine (PSM), 1,2-dioleoyl-*sn*-glycero-3-phosphoethanolamine-*N*-(cap biotinyl) (DOPE-cap-biotin) and lipid probes 1,2-dioleoyl-*sn*-glycero-3-phosphoethanolamine-*N*-(lissamine Rhodamine B sulfonyl) (Rhod-DOPE) and 1,2-dipalmitoyl-*sn*-glycero-3-phosphoethanolamine-*N*-(7-nitro-2-1,3-benzoxa-diazol-4-yl) (NBD-DPPE) were obtained from Avanti Polar Lipids (Alabaster, AL). All lipid solutions were kept in UVASOL grade chloroform, purchased from Merck (Darmstadt, Germany).

All aqueous solutions in this project were prepared using MilliQ water.

2.2. GLASS SUBSTRATE TREATMENT

2.2.1. Functionalization with 3-glycidyloxypropyl trimethoxysilane

All glass coverslips used were first rinsed in Piranha solution ($\text{H}_2\text{SO}_4:\text{H}_2\text{O}_2$, 3:1 v/v) during at least 2 hours, washed copiously with deionized water and dried under gaseous nitrogen (N_2) flux. In the first experiments of this work, glass coverslips were functionalized with GPTS according to protocols described in literature (103, 104); the later experiments of this project do not involve silanized (i.e. GPTS-functionalized) coverslips. Briefly, coverslips were incubated in GPTS 1% v/v in ethanol for 1 hour, washed at least three times in ethanol and dried under N_2 flux. The glass substrate was cured at 150°C for at least 2 hours, then rinsed in ethanol and dried again under N_2 flux.

2.2.2. Photolithography

To develop a photoresist mask, glass coverslips were first submitted to a vapor priming process during approximately 30 minutes, to promote subsequent photoresist adhesion. Silanized coverslips

didn't require any vapor priming step, since the silanes on the glass surface already provided an adequate surface for photoresist adhesion. Briefly, the samples were first dehydrated under vacuum for 2 minutes and heated to 130°C, then exposed to gaseous hexamethyldisilazane (HDMS) at 6 Torr during 5 minutes and finally dried under N₂ flux, followed by vacuum. After this step, light-sensitive polymer, or photoresist, was spin-coated all over the substrate at 2500 rpm and soft-baked at 85°C to obtain a predicted thickness of $\approx 1.45 \mu\text{m}$. Exposure of the regions to be later removed was done using direct write laser (DWL) lithography at 405 nm, performed by Lasarray 2.0 from Heidelberg Instruments (Heidelberg, Germany); the position of these regions were determined by a virtual mask previously constructed using AutoCAD software from Autodesk Inc, synchronized with Lasarray 2.0. Finally, the samples were baked at 110°C for 60 seconds, cooled, exposed to photoresist developer for 60 seconds, which removed previously light-exposed regions; the samples were finally washed with deionized water and dried. The treated glass coverslips were conserved at 4°C before using, to minimize photoresist mask degradation (one week maximum).

2.2.3. Protein immobilization

Solutions of proteins (either avidin, BSA or BSA-biotin) to be immobilized in non-functionalized glass coverslips or glass bottom eight-well μ -Slides from Ibidi (Munich, Germany) were prepared at 0.1 or 1 mg/mL in pH 7.4 buffer containing 10 mM PBS, 1 M NaCl, 2.7 mM KCl and 50 μM NaN₃. Avidin-Alexa350 or avidin-Alexa488 were mixed with unlabeled avidin solution (1:12 or 1:25 mol:mol labeled to unlabeled protein, for either avidin-Alexa350 or avidin-Alexa488) and BSA-Alexa594 was mixed with unlabeled BSA or BSA-biotin solution (1:25 mol:mol labeled to unlabeled protein) in the same buffer. 200 μL of the final protein solution was then added to the substrate and incubated for 1 hour; the substrate was washed in water and dried under N₂ flux.

Protein solutions added to GPTS-functionalized glass were prepared at 1 mg/mL in pH 9 buffer containing 10 mM NaHCO₃ and 1 M NaCl, mixed with the same quantities of fluorescent conjugate as in non-functionalized glass coverslips. Basic pH proved important for reaction with the surface epoxides (103, 105, 106) and high salt concentration enhanced protein-surface interactions (107). A 200 μL droplet was added to the coverslips, and after 1 hour incubation, washed in water and dried under N₂ flux, the substrate was immersed in 2 mM glycine solution 0.5 M NaHCO₃ pH 9 to quench the remaining epoxides, and again washed and dried (103).

2.2.4. Avidin micropatterning

Throughout the work, we used different procedures to create the avidin micropatterning. The first two strategies, briefly, made use of non-functionalized or GPTS-functionalized coverslips containing photoresist mask. The coverslips were incubated with 200 μL avidin (either in PBS or NaHCO₃ buffer, see section 2.2.3), washed with water, dried and rapidly washed with acetone to remove the photoresist and the overlying adsorbed protein, leaving avidin-enriched regions immobilized on the surface. See Results and Discussion (section 3.1.3) for more details on the procedure.

The avidin micropatterning fabrication procedure used in supported lipid membrane experiments made use of BSA-biotin to immobilize avidin. Clean coverslips were incubated with 200 μL BSA-biotin, washed with water, dried under N_2 flux and incubated with 200 μL avidin followed by the same washing and drying step. The coverslips were rapidly washed with acetone to remove the photoresist and the overlying adsorbed protein, leaving only the BSA-biotin-avidin complex immobilized on the glass surface. See Results and Discussion (section 3.1.4) for more details on the procedure. The patterning was visualized by confocal or two-photon fluorescence microscopy.

2.2.5. Biotin-fluorescein experiments

To evaluate whether or not micropatterning fabrication resulted in avidin incapability for binding biotin, we made use of a biotin-fluorescein conjugate. A biotin-fluorescein solution in ethanol was first quantified spectrophotometrically and diluted to 50 $\mu\text{g}/\text{mL}$ in 10 mM PBS, 1 M NaCl, 2.7 mM KCl and 50 μM NaN_3 buffer. The concentration ensures that the number of molecules of conjugate per milliliter is higher than the number of avidin monomers (4 binding-sites/avidin) adsorbed on the surface. 200 μL of solution was then added to the glass coverslips previously coated with BSA-biotin and avidin during 1 hour; in the case of micropatterned samples, this was done after acetone washing. The coverslips were then washed in water, dried under N_2 flux and observed under the confocal microscope.

2.3. PREPARATION OF SUPPORTED LIPID BILAYERS

2.3.1. Lipid quantification

Unlabelled lipids POPC, PSM and DOPE-cap-biotin were quantified using a methodology described in literature (108). Briefly, this method was based on the determination of inorganic phosphate hydrolyzed from phospholipids in the presence of perchloric acid at 200°C. The inorganic phosphate reacted with ammonium heptamolibdate and ascorbic acid, forming a blue compound which was detected at 825 nm. The phosphate concentration, in this case, is equal to the phospholipid concentration, since POPC, PSM and DOPE-cap-biotin contain only one phosphate group.

Labeled lipids Rhod-DOPE and NBD-DPPE were quantified spectrophotometrically using published absorption coefficients - $\epsilon_{559\text{nm, chloroform}} = 95 \times 10^3 \text{ M}^{-1} \text{ cm}^{-1}$ and $\epsilon_{458\text{nm, chloroform}} = 21 \times 10^3 \text{ M}^{-1} \text{ cm}^{-1}$, respectively (109).

Cholesterol concentration in stock solution was determined gravimetrically with a UMT2 high-precision scale from Mettler Toledo (Columbus, Ohio). Empty vials were weighted several times and then filled with the desired volume of Chol, which was then evaporated using N_2 flux and kept in vacuum overnight. Vials with Chol film were weighted and cholesterol mass determined by the difference in masses from registered weights.

2.3.2. *Small unilamellar vesicles*

Required volumes of lipid and fluorescent probe stock solutions were mixed in chloroform to the desired quantities. Ternary lipid mixtures to form 86% L_o and 14% L_d phase were composed of POPC:Chol:PSM (1:1:1 mol:mol:mol), DOPE-cap-biotin (1:1000 mol:mol conjugate to unlabeled lipid ratio) and mixed with NBD-DPPE (1:200 mol:mol labeled to unlabeled lipid ratio) and Rhod-DOPE (1:500 mol:mol labeled to unlabeled lipid ratio) as membrane markers (24). Simple POPC mixtures were prepared with either NBD-DPPE (1:200 mol:mol) or Rhod-DOPE (1:500 mol:mol) as membrane markers, and DOPE-cap-biotin (1:1000 mol:mol) when necessary. The lipid mixtures were then dried under N_2 flux, left in vacuum overnight and resuspended in liposome hydration buffer (10 mM PBS, 150 mM NaCl, 3 mM KCl, pH 7.20). Freeze-thaw cycles were performed to re-equilibrate and homogenize the samples, and sonication was performed on a Branson Sonifier 250 from Branson Ultrasonics (Danbury, USA) during 15 minutes to form small unilamellar vesicles (SUVs). After this step, the mixture was centrifuged using a Sigma 2K15 centrifuge from B. Braun (Melsungen, Germany) at 20000 g and 15°C, during 30 minutes to remove particles from the sonifier microtip. The supernatant containing the vesicles was conserved at 4°C until necessary.

Before adding the SUVs to the glass coverslips, vesicles were diluted in liposome fusion buffer (10 mM HEPES, 150 mM NaCl, 3 mM NaN_3 , 3 mM $CaCl_2$, pH 7.40) to 1 mM final lipid concentration; the calcium ion was present to enhance fusion of the liposomes to the surface (83, 110). A 200 μ L droplet was added to the glass substrate to form SLBs, and after one hour incubation, the samples were washed in liposome washing buffer (10 mM HEPES, 150 mM NaCl, 3 mM NaN_3 , pH 7.40) to remove excess vesicles. An additional previously-treated glass coverslip was used to cover the substrate to prevent dehydration. The samples were visualized using confocal fluorescence microscopy.

2.3.3. *Giant unilamellar vesicles*

Giant unilamellar vesicles (GUVs) were obtained by electroformation using platinum wires as previously described (111). Required volumes of lipid and lipid fluorescent probe stock solutions were mixed in chloroform to the final concentration of 1 mM. Simple POPC mixtures included DOPE-cap-biotin (1:1000 mol:mol labeled to unlabeled lipid ratio) and Rhod-DOPE (1:500 mol:mol labeled to unlabeled lipid ratio) or NBD-DPPE (1:200 mol:mol labeled to unlabeled lipid ratio) as a membrane marker. A total of 2 μ L were spread over each electrode, which were subsequently emerged in 1 mL 200 mM sucrose solution pre-heated at 30°C. Electroformation was performed at this temperature at 10 Hz frequency and 2 V amplitude during 75 minutes. The giant vesicles were then released into the solution by gently shaking the wires.

In order to increase the concentration of GUVs, a total of 4 or more electroformations were performed in the same conditions and vesicle-containing solutions were mixed together in a falcon tube to a total of 4 mL solution. An additional 4 mL of 200 mM glucose solution were added to the tube; the solution was incubated overnight in order to enrich vesicles in the bottom of the tube (as a result of the difference in density inside and outside the vesicles). Before using GUVs, a quantity and

quality check was performed in uncoated eight-well μ -Slides from Ibsi (Munich, Germany) using confocal fluorescence microscopy. Supported lipid bilayers were formed by incubating 200 μ L GUV solution plus 100 μ L glucose solution into either avidin-coated glass bottom eight-well μ -Slides from Ibsi (Munich, Germany) or avidin-coated glass coverslips during 1 hour, followed by removal of 200 μ L solution and subsequent addition of the same volume of water to cause an osmotic shock and rupture of avidin-bound GUVs. The so formed SLBs were visualized by confocal fluorescence microscopy.

2.4. CONFOCAL AND TWO-PHOTON SCANNING LASER MICROSCOPY IMAGING

2.4.1. Experimental setup

All measurements were performed on a Leica TCS SP5 (Leica Microsystems CMS GmbH, Mannheim, Germany) inverted confocal microscope (DMI6000). Excitation lines provided by an argon laser were focused into the sample by apochromatic immersion objectives, either 10x (0.4 numerical aperture) or 63x water objective (1.2 numerical aperture) from Zeiss (Jena, Germany); a pinhole of 1 airy unit (AU) was used to block out-of-focus signals. Two-photon excitation data were obtained using the same Leica TCS SP5 inverted microscope and objectives, but with a titanium-sapphire pulsed laser (Ti:Sa) as the excitation light source; in this case, since the two-photon excitation focal volume is very small, pinhole diameter used was 600 μ m to maximize emitted light collection.

2.4.2. Image acquisition and treatment

In the first part of this work, in order to measure the quantity of avidin immobilized on glass, as well as to evaluate micropatterning, avidin-Alexa488 was excited by 488 nm argon laser line and fluorescence was collected between 500 - 650 nm. To measure the quantity of BSA or BSA-biotin immobilized on glass, BSA-Alexa594 was excited by 514 nm argon laser line and fluorescence was collected between 570 - 750 nm. Biotin-fluorescein was excited at 488 nm and fluorescence was collected between 500 - 700 nm.

In the second and third part of this work, to measure the quantity of protein and quality of avidin micropatterning, avidin-Alexa350 was excited at 760 nm using Ti:Sa laser and fluorescence was collected between 400 - 460 nm. To study membrane organization and lipid distribution, NBD-DPPE and Rhod-DOPE were excited by a 488 nm and 514 nm argon laser lines, respectively. When used simultaneously on the same sample, fluorescence from the NBD group was collected between 470 - 530 nm and fluorescence from the Rhod group was collected between 570 - 700 nm; when used separately, fluorescence from the NBD group was collected between 500 - 700 nm and fluorescence from the Rhod group was collected between 530 - 700 nm. When avidin-Alexa488 and Rhod-DOPE

were used simultaneously, excitation was provided at 488 nm and 514 nm, and fluorescence collected between 500 – 530 nm and 580 – 750 nm, respectively.

In micropatterned samples, fluorescence intensity ratios between the inside of the micropatterned regions and the outside were calculated according to equation (1):

$$Ratio(Inside/Outside) = \left(\frac{\sum_{i=1}^n [I_i^{in} - I_b]}{n} \right) / \left(\frac{\sum_{j=1}^m [I_j^{out} - I_b]}{m} \right) \quad (1)$$

Where I_i^{in} and I_j^{out} are the average fluorescence intensities of n and m ROIs defined inside and outside the micropatterned region, respectively. I_b is the background fluorescence intensity, measured in the same conditions than the samples except with laser output at 0% power. Analysis of imaging data was carried out using ImageJ software developed by Wayne Rasband (NIH, USA).

2.5. FLUORESCENCE RECOVERY AFTER PHOTBLEACHING

2.5.1. Basic principles

In a typical FRAP experiment, fluorescent molecules present in a certain region of interest (ROI), are rapidly and irreversibly switched off, or photobleached, by a high-intensity laser beam. Then, when possible, diffusion of bleached fluorophore from the ROI to the surroundings (and vice-versa for unbleached fluorophore) results in a fluorescence recovery over time, which can be monitored using a low intensity laser beam (112–119). Thus, the technique involves three phases (Figure 2.1): (i) *pre-*

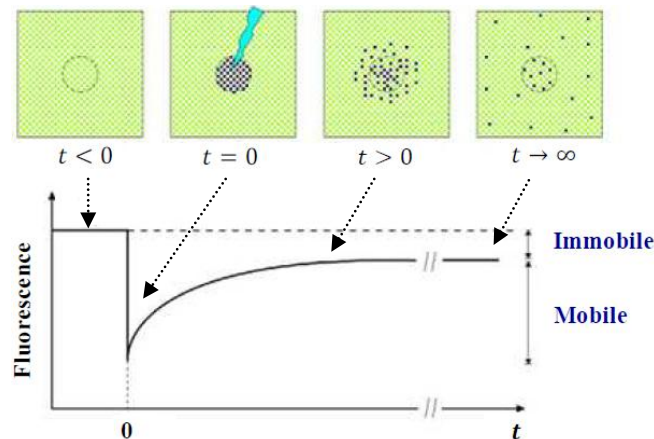


Figure 2.1 – Basic principles of a typical FRAP experiment. The fluorescence signal is measured in the ROI with a low-intensity laser beam ($t < 0$). At $t = 0$, with a high intensity laser beam, the fluorescent molecules are quickly photobleached inside the ROI, causing a decrease in fluorescence. Then, the diffusion process after photobleaching is again monitored with a low-intensity beam ($t > 0$). Due to diffusion transport, the bleached molecules (purple dots) will exchange their position in the bleached area with non-bleached fluorescence molecules (green) from the surroundings, resulting in a recovery of the signal inside the ROI. By plotting the fluorescence intensity of the photobleached spot as a function of time, a FRAP curve is obtained. With a suitable mathematical model, it is possible to extract the diffusion coefficient D and the local mobile fraction of labeled molecules, M_f . Adapted from (139).

bleach phase, where fluorescence intensity is measured with a low-intensity beam; (ii) *bleach* phase, where a high-intensity beam is rapidly applied to the ROI in order to bleach a significant fraction of fluorophore; (iii) *post-bleach* phase, where recovery of fluorescence within the ROI is monitored, again, with a low-intensity beam. From the recovered data, we can not only study fluorophore transport and kinetics (e.g. obtain lateral diffusion coefficient, D) but estimate the fluorophore mobile and immobile fraction (M_f and $1-M_f$, respectively) (Figure 2.1).

In this project, we made use of FRAP technique to confirm if a supported lipid bilayer was formed onto substrate and to evaluate membrane general properties, such as homogeneity, by determining lipid lateral diffusion coefficient and mobile fraction. The next section briefly describes how these parameters can be obtained from a mathematical treatment of a fluorescence recovery curve under certain assumptions.

2.5.2. Model for two-dimensional diffusion

Axelrod et al. have proposed a model for determining the lateral diffusion coefficient of a fluorophore considering two-dimensional (2D) diffusion and a laser beam of uniform circular disk intensity profile (114). Another assumption in the model is that photobleaching of the fluorophore to a non-fluorescent species is a simple irreversible first-order reaction given by equation (2):

$$\frac{dC(r, t)}{dt} = -\alpha I(r)C(r, t) \quad (2)$$

Where α is the rate constant of photobleaching for a specific fluorophore, $I(r)$ is intensity profile of the bleaching pulse in the plane and $C(r, t)$ is the concentration of unbleached fluorophore, at position r and time t . For a circular disc profile, $I(r)$ is given by:

$$I(r) = \begin{cases} P_0/\pi\omega^2, & r \leq \omega \\ 0, & r > \omega \end{cases} \quad (3)$$

In which P_0 is the total laser power and ω is the radius of the circular laser beam. The differential equation (2) is then solved for the boundary and initial conditions, respectively (4) and (5):

$$C(\infty, t) = C_0 \quad (4)$$

$$C(r, 0) = C_0 e^{-\alpha T I(r)} \quad (5)$$

In which C_0 is the initial uniform fluorophore concentration and T is the interval of the bleaching pulse. These conditions consider (i) fluorescent molecules initially uniformly distributed in an infinite, flat membrane with concentration C_0 ; (ii) laser intensity bleaching pulses T shorter than characteristic times for diffusion. Generally, the fluorescence observed at position r and $t \geq 0$ (after photobleaching) can be written as follows:

$$F(t) = \frac{q}{A} \int I(r)C(r, t)d^2r \quad (6)$$

Where q is the product of all quantum efficiencies of laser light absorption, emission and detection, and A is the attenuation factor of the beam during fluorescence recovery. In equation (6), the term $C(r, t)$ must also be a solution of the partial differential equation (7) for lateral diffusion of a single species of fluorophore, given by:

$$\frac{dC(r, t)}{dt} = D\nabla^2 C(r, t) \quad (7)$$

Where D is the diffusion coefficient and ∇^2 is the Laplacian operator. Soumpasis proposed a simplified solution (113) assuming total recovery of fluorescence, given by equation (8):

$$F(t) = e^{-\frac{2\tau_D}{t}} \left[I_0\left(\frac{2\tau_D}{t}\right) + I_1\left(\frac{2\tau_D}{t}\right) \right] \quad (8)$$

Where τ_D is the characteristic diffusion time and I_0 and I_1 are Bessel functions. Finally, the lateral diffusion coefficient D can then be determined using equation (9):

$$D = \frac{\omega^2}{4\tau_D} \quad (9)$$

Where ω , in this case, is the radius of the circular ROI. This method was ideal for the studies performed, since our objective was to study diffusion in supported lipid bilayers, which can conveniently be approximated to a 2D system.

2.5.3. FRAP data acquisition

FRAP measurements were performed on the same Leica TCS SP5 (Leica Microsystems CMS GmbH, Mannheim, Germany) inverted confocal microscope (DMI6000), based on FRAP image-based protocols (120). Excitation lines provided by an argon laser were focused into the sample by an apochromatic immersion 63x water objective (1.2 numerical aperture) from Zeiss (Jena, Germany); instead of 1 AU, the pinhole was changed to 2 AU to increase light collection. The microscope settings were controlled by the FRAP-Wizard of LAS-AF microscope software version 15.1 (Leica Microsystems CMS GmbH, Mannheim, Germany) that allowed to define the scanning conditions, the time lapse between the images and the number of frames in each phase (pre-bleach, photobleach and post-bleach).

In all FRAP experiments, NBD-DPPE was excited at 488 nm and fluorescence was collected between 500 - 700 nm; Rhod-DOPE was excited at 514 nm and fluorescence was collected between 530 - 700 nm. Circular ROI for bleaching was defined with 2.5 μm radius in all experiments. Images were acquired over time using a frame size of 256 x 256 pixels and 1400 Hz scan speed, to maximize

laser intensity inside the ROI. In pre-bleach phase, 10 image scans were performed at low-laser intensity (1 - 5%). In bleach phase, 3 image scans were performed, in order to minimize recovery during bleaching, at high-laser intensity (100%) so as to maximize bleaching efficacy. In post-bleach phase, a minimum of 150 image scans were performed again at low-laser intensity.

2.5.4. FRAP data analysis

The analysis of raw FRAP data was performed using FRAP Analyser software version 1.0.5 developed by A. Halavaty, M. Yatskou and E. Friederich at the University of Luxembourg (<http://actinsim.uni.lu/eng/>) (121). The intensity over time was first normalized, so that recovery curves become independent of initial values and fluorophore concentration, using the double-normalization method (115, 122) as in equation (10):

$$F_{norm}(t) = \left(\frac{F(t) - F_b(t)}{F_{prebleach}} \right) \left(\frac{F_{ref(prebleach)}}{F_{ref}(t) - F_b(t)} \right) \quad (10)$$

Where $F(t)$, $F_{ref}(t)$, $F_b(t)$ are the average fluorescence intensity ($t \geq 0$) inside the bleached, referenced unbleached and background ROI, respectively. In this case, the background ROI is defined on a region where membrane is absent; when background signal could not be measured, it was set to 0. The “prebleach” subscript is indicative of the average fluorescence intensity before bleaching ($t < 0$) in the bleached or reference ROI – these parameters are constants (time-independent). Except for the bleached ROI, all other ROIs were defined *a posteriori* to the FRAP experience with 2.5 μm radius. Using the normalized fluorescence, the diffusion time can be obtained by fitting a modified version of equation (8) to the experimental data according to equation (11):

$$F_{norm}(t) = a_0 + a_1 e^{-\frac{2\tau_D}{t}} \left[I_0 \left(\frac{2\tau_D}{t} \right) + I_1 \left(\frac{2\tau_D}{t} \right) \right] \quad (11)$$

Where $a_0 = F_{norm}(0)$ and $a_1 = F_{norm}(\infty) - F_{norm}(0)$; these terms are introduced to account for non-zero intensity at the bleach moment and incomplete recovery, respectively. Diffusion coefficient can then be obtained using equation (9). The quality of the fit was evaluated by the usual criteria, namely chi-square $\chi^2 < 1.3$ and a random distribution of residuals. The mobile fraction M_f was then readily calculated using equation (12):

$$M_f = \frac{F_{norm}(\infty) - F_{norm}(0)}{F_{norm(prebleach)} - F_{norm}(0)} \quad (12)$$

In which $F_{norm(prebleach)}$, $F_{norm}(0)$ and $F_{norm}(\infty)$ are the normalized fluorescence intensities before the bleach, immediately following the bleach ($t = 0$) and after full recovery ($t \rightarrow \infty$) (115).

3.RESULTS AND DISCUSSION

3.1. FABRICATION OF AVIDIN MICROPATTERNING ON GLASS SUBSTRATE

3.1.1. Avidin and BSA immobilization on glass and resistance to acetone washing

The first part of the work revolved around the development of an avidin micropatterning on glass using photolithography. Due to the fact that this technique is a widely used and simple microfabrication technique (90), we attempted to use it to define the avidin regions. This procedure, although apparently simple, first required that avidin immobilization on glass would not be compromised by solvents used in standard photolithography, such as acetone, which enables photoresist removal after exposure. This led us to perform several tests with clean glass or GPTS-functionalized glass to evaluate avidin and BSA immobilization, namely (i) how much protein was lost during the acetone washing step; (ii) the effect of GPTS-functionalization in resistance to acetone washing. Adsorptions onto clean glass and protein functionalization onto silanized glass (Figure 3.1) were performed each according to the protocol described in Material and Methods (see sections 2.2.1 and 2.2.3).

Results for avidin showed that, before acetone washing, similar quantities of this protein immobilized either on clean glass and GPTS-functionalized glass. However, this protein showed little resistance to acetone washing - when adsorbed on clean glass, about 80% of the protein was peeled off after acetone washing (Figure 3.2 - A1 - A4, B). GPTS-functionalized avidin seemed to confer some level of resistance (more than half the protein remained on the surface), which was expected since some protein is covalently bound to glass GPTS (Figure 3.2 - B). Importantly, BSA is shown to be very resistant to organic solvent washing since almost no protein was lost during the washing step either on clean or GPTS-functionalized glass (Figure 3.2 – A5 - A8, B).

Given the results for these proteins, the next steps focused on the conceptualization and development of an avidin micropatterned model system.

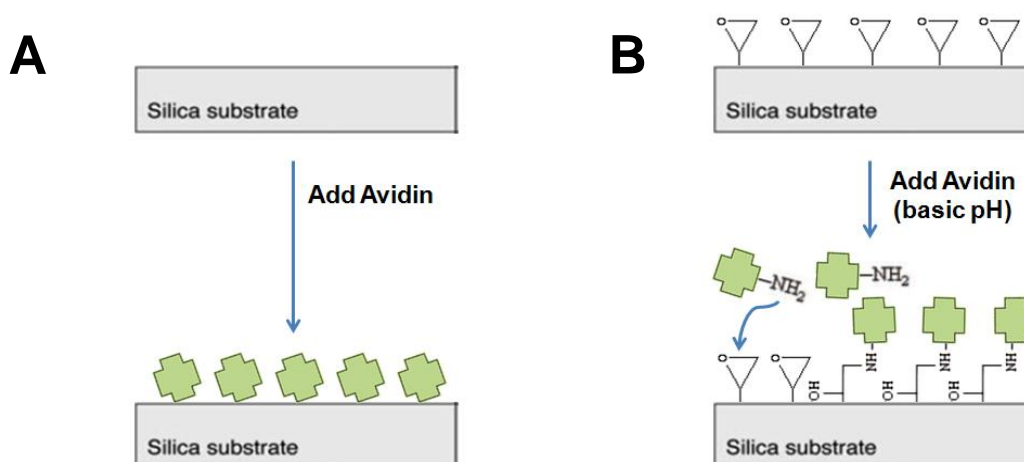


Figure 3.1 – General protein immobilization on glass procedure. (A) On cleaned glass substrate (silica substrate), a droplet of avidin is added to the glass coverslips and protein adsorbs on the surface (non-covalent immobilization). (B) On GPTS-functionalized glass (i.e. silanized glass) a droplet of avidin is added in basic pH buffer, necessary for the reaction of amine group(s) on the protein chain with epoxide groups on the surface (covalent immobilization). See Materials and Methods for more details (sections 2.2.1 and 2.2.3).

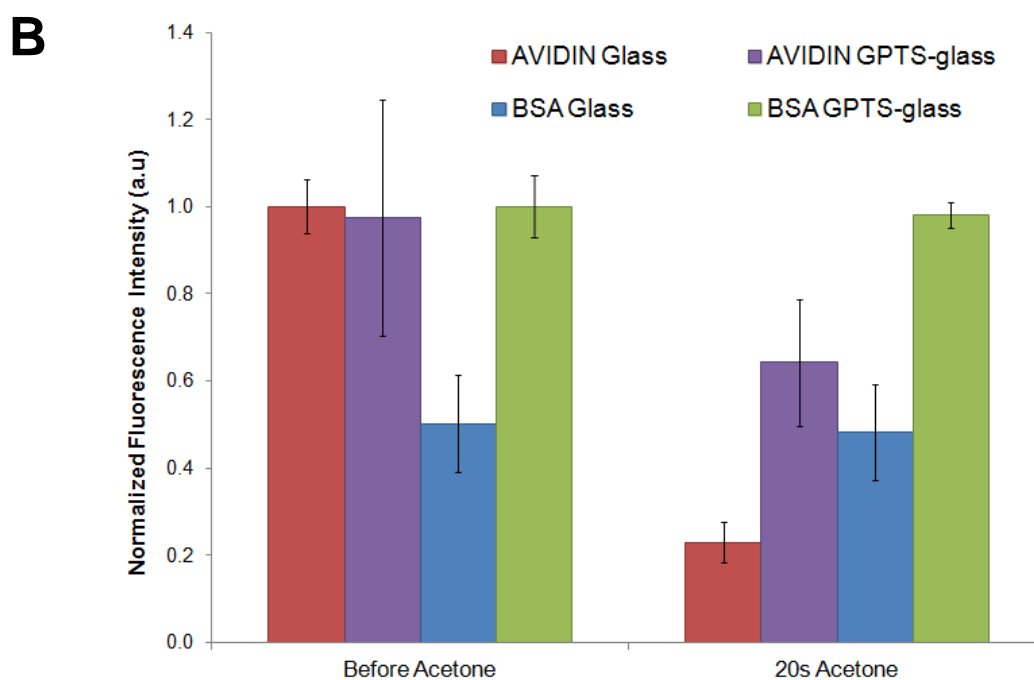
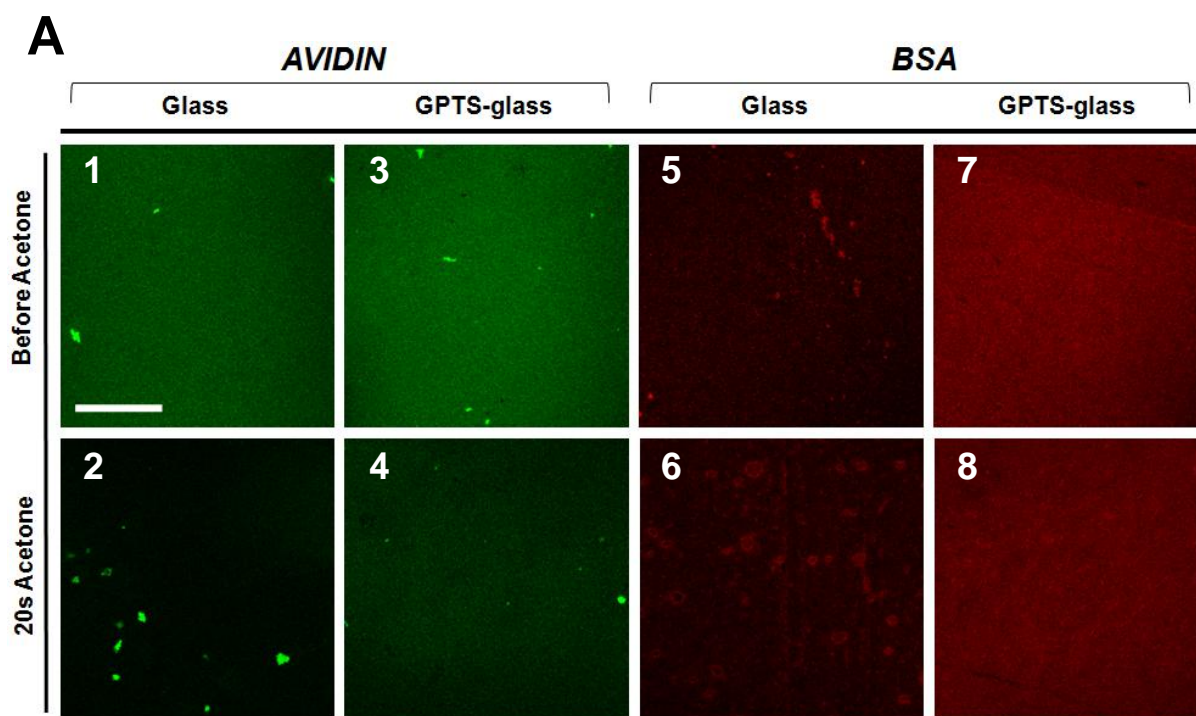


Figure 3.2 – Avidin and BSA resistance to acetone washing after adsorption onto clean or GPTS-functionalized glass.

(A) Confocal images showing avidin and BSA-coated surfaces, on clean glass or GPTS-functionalized glass, before acetone washing (1,3,5,7) and after 20 second acetone washing (2,4,6,8). Fluorescence is from avidin-Alexa488 (1:25 mol:mol labeled to unlabelled protein ratio) and from BSA-Alexa594 (1:25 mol:mol labelled to unlabelled protein ratio). One representative image was chosen among several collected. Scale bar is 25 μ m (B) Bar plot showing normalized fluorescence intensity of avidin and BSA surface, on clean glass or GPTS-functionalized glass, before and after 20 second acetone washing. Values represent mean \pm standard deviations. Fluorescence intensity was collected from different areas of the coverslip surface, averaged from at least 3 representative images of the surface, and normalized for the maximum fluorescence observed for each fluorophore. BSA and avidin were added at 1 mg/mL concentration.

3.1.2. Model system conceptualization

After optimization, we conceptualized a model to form discrete regions of avidin onto the glass coverslips (Figure 3.3). We defined different total areas of immobilized avidin – 50%, 20% and 10% of the 1 x 1 mm square - each square would contain regions of different sizes (squares of 20, 10 and 5 μm side length). These defined protein regions aimed to serve as adhesions to the membranes formed onto glass, which would allow us to study the effect of these tethers in phase separation and lipid distribution, thus mimicking, in a simple fashion, cytoskeleton-cell membrane adhesions. The next steps included several strategies to form this model, based on the results obtained on the previous section (section. 3.1.1).

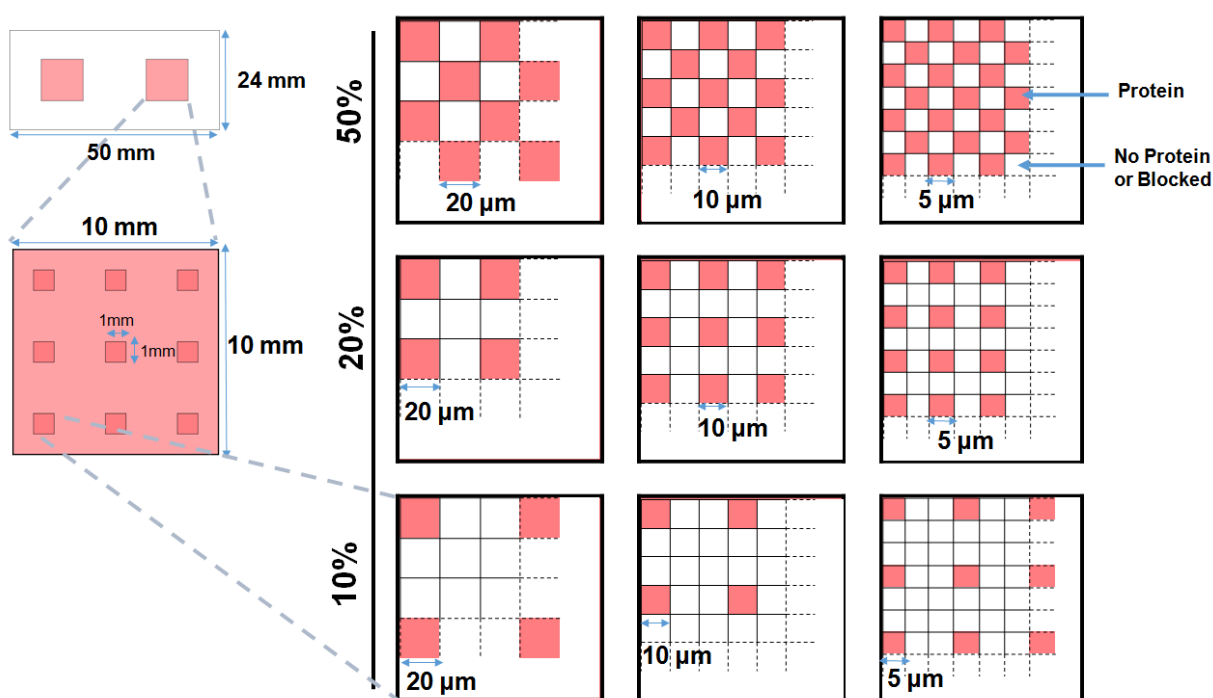


Figure 3.3 – Model of avidin micropatterning on glass coverslips. Glass coverslips with dimensions 50 x 24 mm contain duplicate regions, each region containing nine squares of 1 x 1 mm. Pink regions correspond to immobilized avidin; white regions correspond to empty or BSA-blocked regions. In the first, second and third row of squares, the whole area with immobilized avidin accounts for 50%, 20% and 10% of the total area, respectively. The side length of the squares decreases from left to right (20, 10 and 5 μm). Each 1 x 1 mm square has a roman numeral so that it can be identified under the microscope (not shown in figure). This distribution of immobilized protein aimed to study the effect of the tether size and total area of tethering in phase separation and lipid membrane reorganization.

3.1.3. Avidin micropatterning fabrication on clean and GPTS-functionalized glass

In section 3.1.1, we observed that in the absence of GPTS functionalization, non-negligible amounts of avidin were present in the glass surface after acetone washing ($\approx 20\%$ remained); additionally, GPTS-functionalization resulted in an increase in resistance of this protein to this washing step ($\approx 50\%$ remained). This led us to attempt to form an avidin micropatterning using both these strategies. First, a clean or GPTS-functionalized glass coverslip (Figure 3.4 - 1) was subjected to standard photolithography with the conditions described in section 2.2.2. The photoresist polymer was spin-coated onto the glass substrate (Figure 3.4 - 2); then, regions to be later immobilized with avidin were exposed to a laser beam at 405 nm (Figure 3.4 - 3); in the last step of photolithography, developer selectively removed laser-exposed regions of the photoresist, leaving the glass underneath

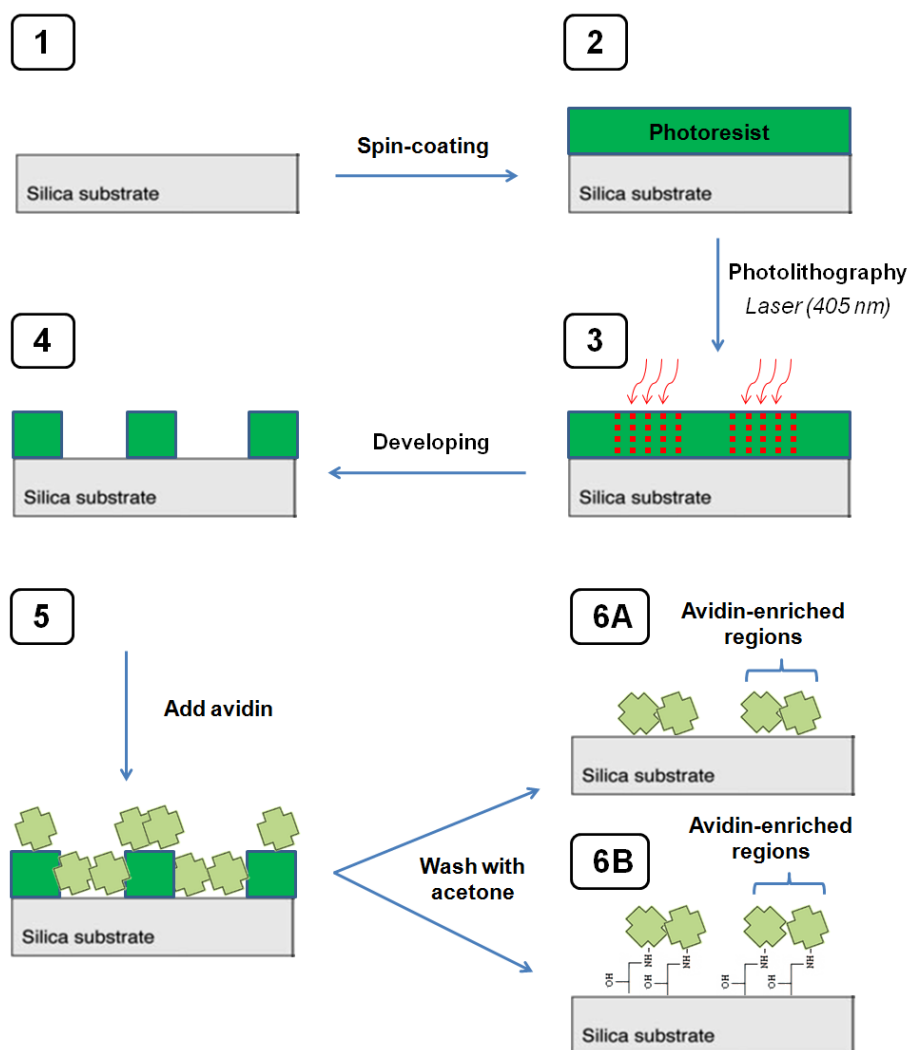


Figure 3.4 – Protocol used to create an avidin micropatterning on clean or GPTS-functionalized glass using photolithography. A clean or GPTS-functionalized glass coverslip (1) was subject to photoresist spin-coating (2). A laser working at 405 nm irradiated regions to be later immobilized with avidin, pre-defined by a virtual mask (3) and photoresist developer selectively removed irradiated regions, exposing the glass underneath (4). An aqueous solution of avidin was then added to the glass slides for adsorption or reaction with surface epoxides, which are not shown on the picture (5). Finally, an acetone squirt removed the photoresist containing adsorbed avidin, leaving discrete regions of avidin immobilized on glass either by adsorption (6A) or bound covalently (6B).

free for subsequent protein adsorption (Figure 3.4 - 4). Following photolithography, avidin was added and immobilized both on exposed glass and photoresist (Figure 3.4 - 5); while in clean glass avidin immobilized by adsorption, in GPTS glass coverslips avidin reacted with epoxides and covalently bound the surface. The last step involved photoresist removal using a fast acetone squirt - avidin adsorbed onto the photoresist was removed along with it, leaving discrete avidin-enriched regions immobilized on glass, either by adsorption or covalently bound (Figure 3.4 - 6A and 6B respectively).

We next show some results of the photolithography procedure, referring to steps 1 - 4 in Figure 3.4, before any protein adsorption. The photoresist displays fluorescence between approximately 500 - 700 nm (Figure 3.5 - A, C), which allowed to us to evaluate the quality of photoresist mask under the confocal microscope. The pattern formed by photolithography was well defined; the red regions represent the photoresist, which was removed later by acetone washing; the black regions are glass exposed regions, which were later coated with avidin (Figure 3.5 - A). We were also able to measure the thickness of the photoresist (Figure 3.5 - B) - 1.45 μm - using an xz scanning, which was in

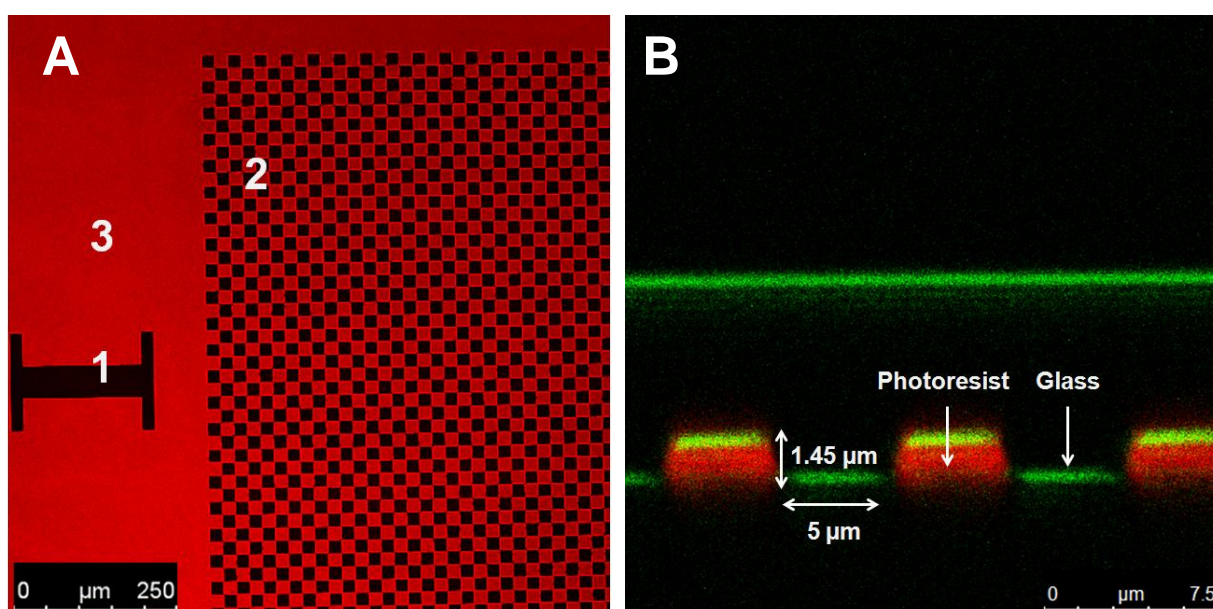
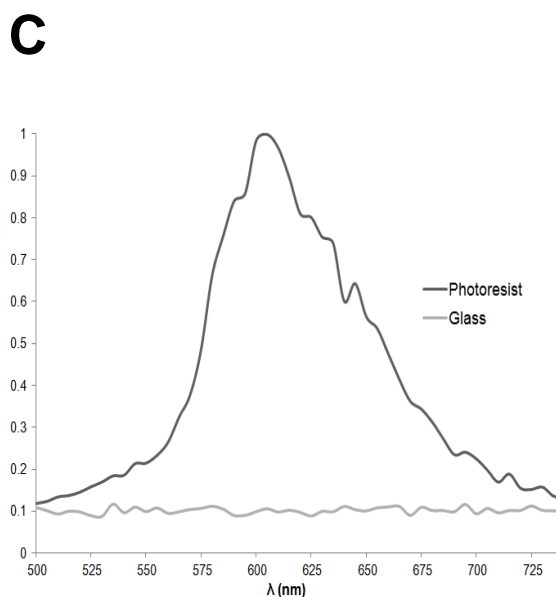


Figure 3.5 - Photoresist mask designed by photolithography. (A) Photoresist mask fluorescence. Red regions represent photoresist fluorescence and black regions represent exposed glass where avidin was to be later immobilized. Region 1 shows the numeral that identifies which pattern, out of nine possible patterns, was under observation. Region 2 shows the pattern, which is made of 20 μm squares and accounts for 50% of the total 1 x 1 mm square area. Region 3 represents the area outside the patterns, which was filled with photoresist that would later be removed. (B) XZ plane image of photoresist pattern on glass. The glass-water and photoresist-water interface is shown at green and photoresist at red; photoresist thickness was approximately 1.45 μm as expected; between photoresist regions lie squares with 5 μm dimensions. Collected fluorescence is from photoresist. (C) Photoresist emission spectrum obtained under confocal microscope. $\lambda_{\text{exc}} = 488 \text{ nm}$. $\lambda_{\text{em peak}} \approx 605 - 610 \text{ nm}$.



agreement with the thickness predicted by spin-coating conditions in photolithography (see section 2.2.2). Having validated the photolithography process, avidin micropatterning was created onto the glass coverslip, either non-functionalized or GPTS-functionalized, by avidin addition according to steps 5 and 6 in Figure 3.4.

In the non-functionalized samples, the avidin pattern was reasonably well defined as is evidenced by the roman numeral and 20, 10 and 5 μm side avidin squares. The ratio obtained when comparing average intensities inside and outside avidin-enriched regions was 21.68 ± 0.81 , which is satisfactory, although some areas surrounding the avidin-coated regions displayed residual fluorescence, suggesting that some avidin was present outside (Figure 3.6 – A, B, C). Two types of defects were observed in this patterning. First, a film-like structure could be seen protruding from some avidin squares (Figure 3.6 – C). These structures were likely formed during the acetone washing step, which removed some avidin from the squares and spread it on the glass outside these regions. The second type of defect was the higher fluorescence observed on the limits of the squares when compared to the bulk of these regions (Figure 3.6 – B). This effect was attributed to avidin that adsorbed on the photoresist vertical regions – photoresist has around 1.45 μm thickness, which means that protein adsorbs not only onto glass-exposed regions and onto upper photoresist layer, but on the sides of the photoresist. When acetone removes photoresist, avidin adsorbed on the side is either removed or adsorbs rapidly on the bottom, creating those structures with higher fluorescence intensity than inside the squares. These results suggest that although the pattern, overall, was visible, the acetone washing step caused the removal of some avidin from the squares and decreased the definition of the squares.

Results obtained for avidin micropatterning on GPTS-functionalized glass depicted a better definition than in the previous case, with neither residual fluorescence nor protrusions from the squares (Figure 3.6 – D). This is not surprising, since GPTS, as we have seen, provides a higher resistance to the acetone washing step, allowing for a higher number of molecules to stay immobilized after washing (section 3.1.1). The patterning was satisfactory for 20, 10 and 5 μm side squares; nevertheless, on the limits of the squares, film-like regions with higher intensity were observed again, just as in the case of avidin adsorbed on the non-functionalized glass and probably for the same reasons (Figure 3.6 – E). Despite the better definition overall, the ratio of average intensities between inside avidin-enriched regions and outside regions was 18.26 ± 0.63 , which was very similar to the previous result.

In either GPTS-functionalized and non-functionalized glass, some regions of the pattern were not defined and a high fluorescence signal was observed in a large area (Figure 3.6 – F). We attribute these results to an inefficient acetone washing step; if the avidin adsorbed on top of the photoresist is not removed fast enough during acetone washing, it can adsorb back on the surface of the glass, creating these structures.

At this point, we attempted a different strategy to improve the quality and quantity of avidin immobilized on the glass surface. Making use of the results obtained in section 3.1.1, suggesting that BSA was resistant to organic solvent washing, we attempted to use biotinylated BSA to form an avidin micropatterning.

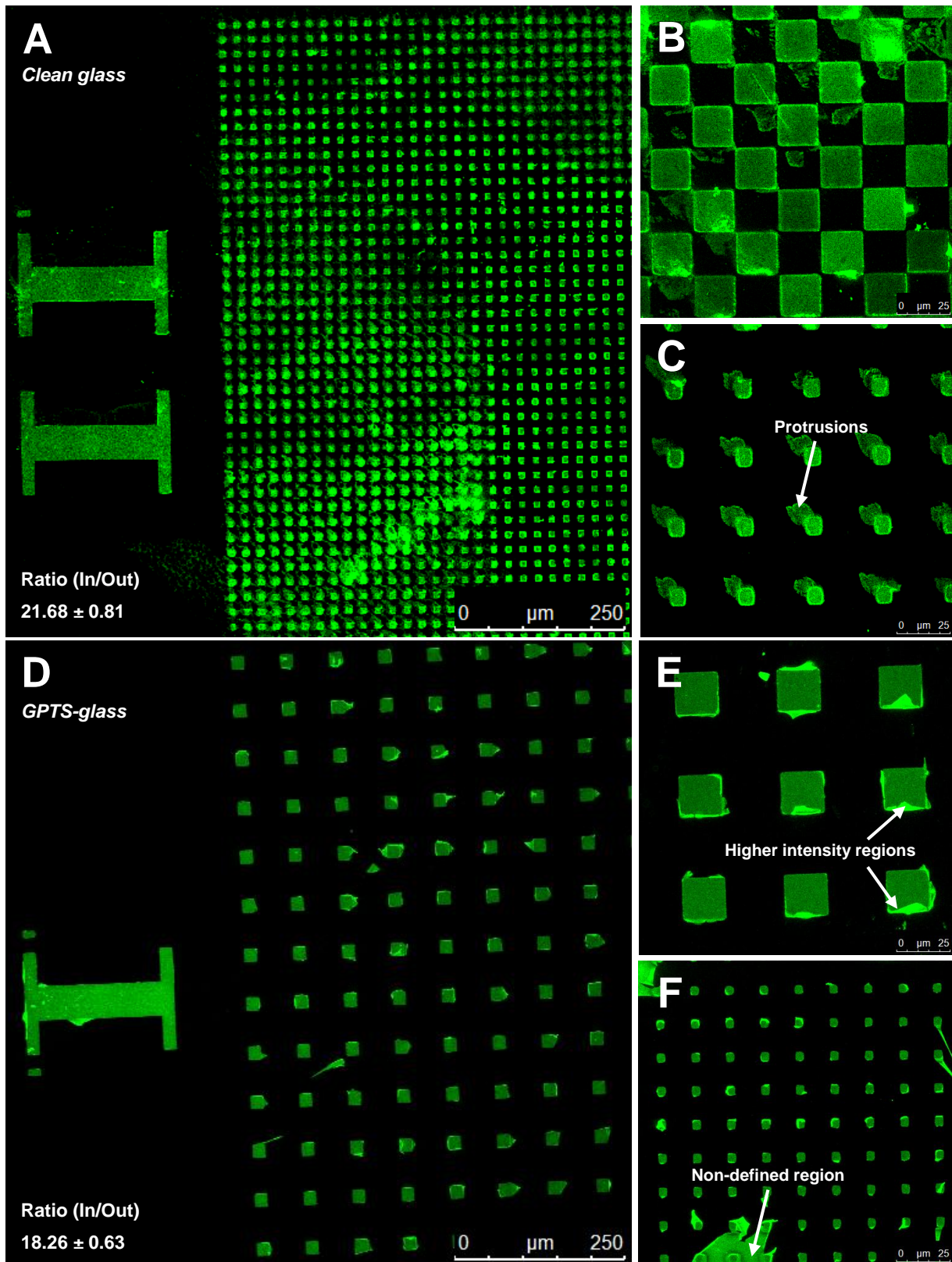


Figure 3.6 – Avidin micropatterning formed on clean and GPTS-functionalized glass coverslips. (A) Micropatterning surface after avidin addition to non-functionalized glass, showing 5 μm squares (20% protein-coated area). The numeral that identifies which pattern was under observation, and the average intensity ratios between inside and outside micropatterned regions are also shown. (B), (C) Micropatterning showing 20 and 10 μm side squares (50% and 20% protein-coated area), respectively. (D) Micropatterning surface after avidin addition to GPTS-functionalized glass showing 20 μm squares (10% protein-coated area). The roman numeral and the average intensity ratio between inside and outside micropatterned regions are also shown. (E), (F) Micropatterning showing 20 and 5 μm side squares (20% and 10% protein-coated area), respectively; the arrow indicates regions of high intensity and non-defined avidin region, respectively (F). Fluorescence is from avidin-Alexa488 (1:25 mol:mol labeled to unlabelled protein ratio). Avidin was added at 1 mg/mL concentration.

3.1.4. Avidin micropatterning fabrication using biotinylated BSA

Since BSA had shown to be extremely resistant to acetone washing, we attempted to create an avidin micropatterning using BSA-biotin to immobilize avidin. Potential advantages of this method are (i) the high affinity constant between biotin and avidin, which enables a great amount of avidin to be adsorbed ($K_a \approx 10^{15} \text{ M}^{-1}$) (123, 124); (ii) the extreme robustness and strength of avidin-biotin non-covalent bond, which is likely to stabilize the complex and is generally unaffected by extreme pH, temperature, organic solvents and other denaturing agents (125). The procedure was similar to the one used in section 3.1.3. The photoresist was first spin-coated, exposed to laser light and developed to yield a photoresist mask (Figure 3.7 – 1 – 4).

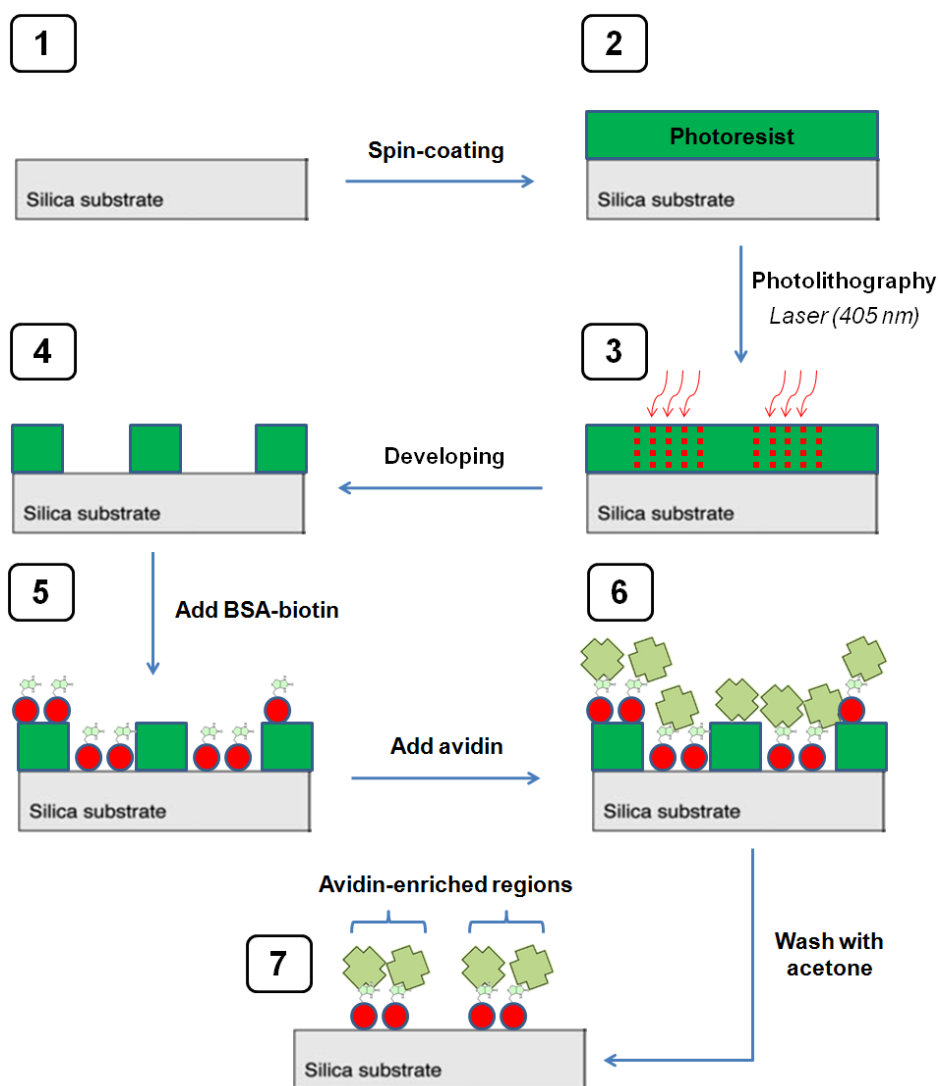


Figure 3.7 – Protocol used to create an avidin micropatterning using biotinylated BSA. A clean glass coverslip (1) was subject to photoresist spin-coating (2). A laser working at 405 nm irradiated regions to be later immobilized with avidin, pre-defined by a virtual mask (3) and photoresist developer selectively removed irradiated regions, exposing the glass underneath (4). An aqueous solution of BSA-Biotin was then added to the glass slides for adsorption (5), followed by an aqueous solution of avidin, which adsorbed on the surface, photoresist and/or bound to BSA-biotin (6). Finally, an acetone squirt removed the photoresist containing adsorbed BSA-biotin with bound avidin, leaving discrete regions of BSA-biotin-avidin complex immobilized on glass (7).

Following photolithography, BSA-biotin was added and adsorbed both on exposed glass and photoresist (Figure 3.7 – 5); secondly, avidin was added (Figure 3.7 – 6). – most of the avidin bound biotin, in principle, due to the high affinity between the two. Finally, an acetone squirt removed the photoresist, leaving the BSA-biotin-bound avidin on the surface (Figure 3.7 – 7).

We observed that the avidin immobilization step before acetone washing was efficient, since avidin-Alexa488 fluorescence was practically uniform everywhere, indicating that avidin immobilized both on photoresist and onto glass-exposed regions after binding BSA-biotin (Figure 3.8 - A). It is important to note that photoresist, when excited at 488 nm, has a much lower fluorescence than avidin-Alexa488 at the same excitation wavelength; as such, almost all fluorescence captured before acetone washing can be attributed to Alexa488. After washing with acetone, the photoresist was removed together with BSA-biotin and avidin adsorbed on it, forming a well defined pattern as it can be seen by the roman numeral and the 20 μm squares (Figure 3.8 - B). A small part of the pattern remained ill-defined, suggesting that BSA-biotin-bound avidin adsorbed onto the photoresist was not properly lifted-off during acetone washing step, resulting in either glass adsorption (similarly to what happened in the first micropatterning experiments, section 3.1.3, Figure 3.6 – F) or binding to other complexes (avidin has 4 monomer subunits and BSA is conjugated with up to 16 biotin molecules, resulting in a high binding potential). Nevertheless, the definition of all three different squares sizes - 20, 10 and 5 μm – was successful, which was crucial to our work, since the accurate size of the tethers was an important feature to define the model (Figure 3.8 - C, D, E). Perhaps one of the most important results was the high contrast observed between avidin-enriched regions and outside regions – it was essential that the outside of these regions contained little or no avidin, so as to minimize their impact on lipid organization. In fact, we compared Alexa488 emission spectrum outside and inside the avidin-enriched regions, concluding that no significant levels of avidin were present in the former, as opposed to the latter where the Alexa488 characteristic spectrum was detected (Figure 3.8 - F). Finally, we measured the absolute intensity of avidin-Alexa488 in several square regions, obtaining a ratio of average intensities of approximately 98 between inside and outside regions, which was very satisfactory for the purpose of our work and higher than the previous micropatterned samples without BSA-biotin.

Due to the high intensity ratio obtained between avidin squares and outside regions, stability of the BSA-biotin and good pattern definition, the protocol here depicted to create an avidin micropatterning onto glass was preferred to the previous procedures and was used in the subsequent studies of this work. The next experiments attempted to evaluate avidin capacity for binding biotin after the micropatterning procedure, which was crucial for the subsequent studies.

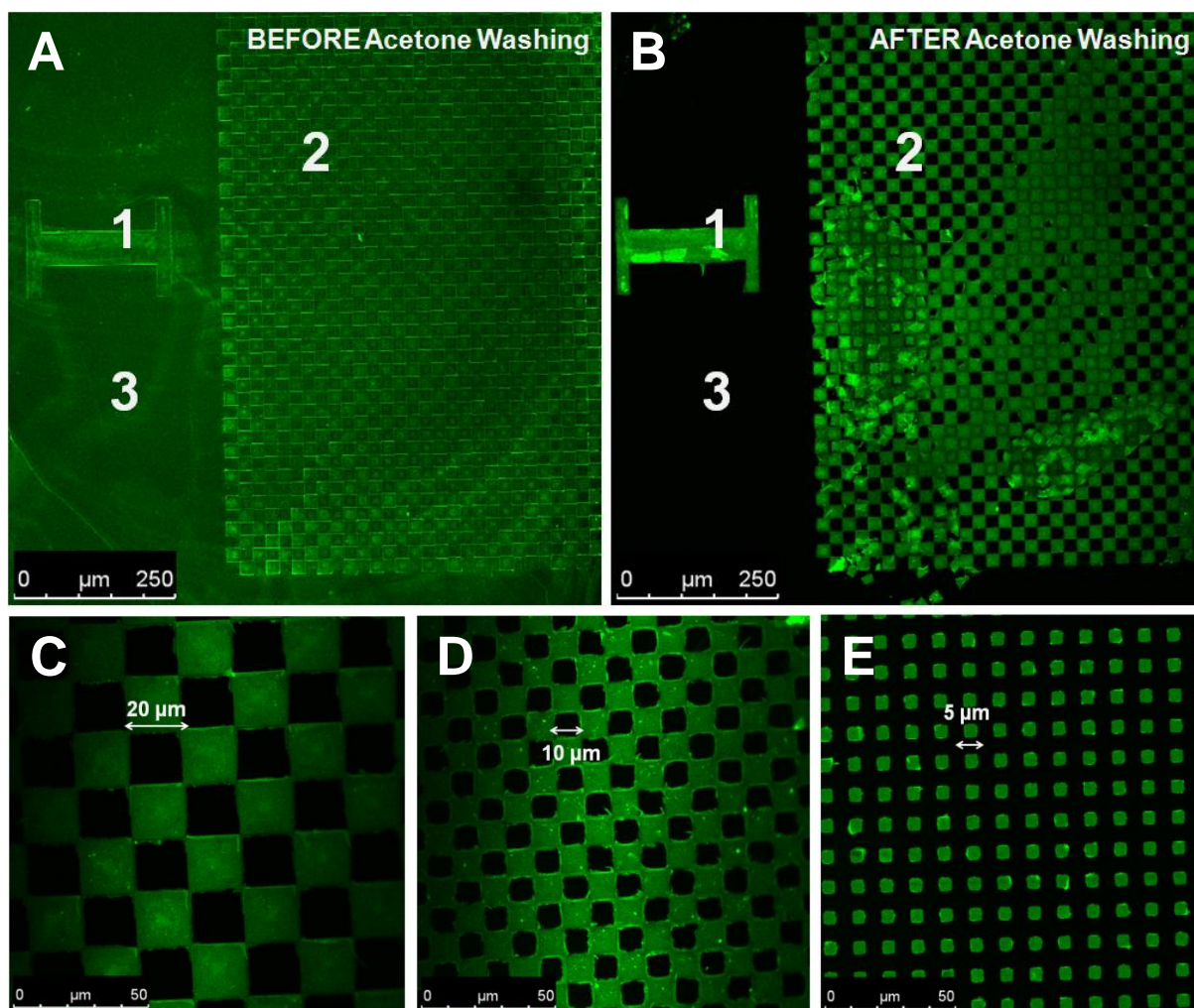
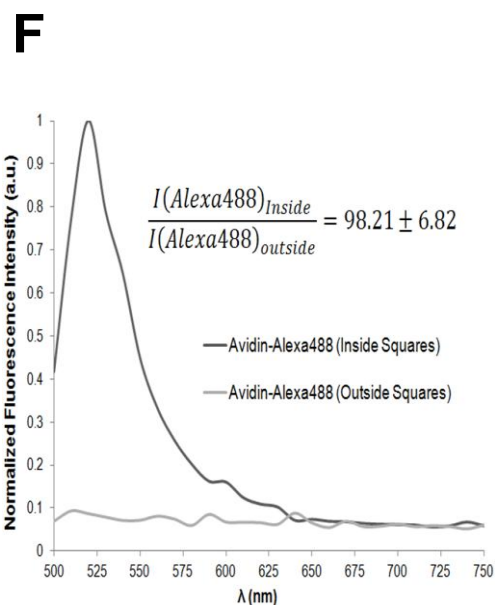


Figure 3.8 – Avidin micropatterning on glass. (A) Micropatterned surface after avidin addition and before acetone washing. Region 1 shows the numeral that identifies which pattern, out of nine possible patterns, was under observation. Region 2 shows the pattern, which is made of 20 μm squares; total protein-coated area is 50%. Region 3 represents the area outside the patterns, which was filled with photoresist and adsorbed BSA-biotin-bound avidin that would later be removed. Fluorescence can be seen everywhere, which indicates successful avidin immobilization on the surface. (B) Avidin micropatterning after acetone washing. Regions 1, 2 and 3 depicted are the same as in (A), except now BSA-biotin-bound avidin adsorbed onto photoresist got lifted-off and Alexa488 fluorescence revealed a well-defined avidin micropatterning. (C) Avidin micropatterning showing 20 μm squares (50% protein-coated area). (D) Avidin micropatterning showing 10 μm squares (50% protein-coated area). (E) Avidin micropatterning showing 5 μm squares (20% protein-coated area). Fluorescence is from avidin-Alexa488 (1:12 mol:mol). (F) Avidin-Alexa488 emission spectrum measured inside and outside avidin-enriched regions ($\lambda_{\text{em peak}} \approx 520 \text{ nm}$); ratio of average fluorescence intensities inside and outside the same regions is also shown. BSA-biotin and avidin were added at 0.1 and 1 mg/mL concentration, respectively.



3.1.5. Effect of the microfabrication procedure on avidin ability for binding biotin

The procedure used to fabricate avidin patterning involves surface modifications and treatment with organic solvents, namely acetone, which are generally not protein-friendly. We then attempted to evaluate if the microfabrication process compromised avidin ability to bind biotin. We made use of unlabeled BSA-biotin and avidin to construct the micropatterning according to standard procedure (section 3.1.4, Figure 3.7). Afterwards, biotin-fluorescein was added to the glass coverslip in order to bind avidin.

The results show that the micropatterning was considerably well-defined, although at an inferior level than expected (Figure 3.9 – A, B, C), suggesting that most of the micropatterned avidin was functional. We made use of two controls (non-micropatterned glass coverslips), washed or non-washed with acetone, to compare with the micropatterned samples. Apparently, acetone washing did not affect avidin capacity for binding biotin-fluorescein in the controls, suggesting that this solvent does not affect avidin functionality (Figure 3.9 – D). Additionally, about three times more biotin-fluorescein was able to bind to the controls, either washed or non-washed with acetone, than in the micropatterned samples. One reason for this would be that, while in controls we directly adsorb BSA-Biotin onto a cleaned glass coverslip, in micropatterned glass coverslips we subject the substrate to various treatments such as HDMS, photoresist and photoresist developer during the microfabrication, which may change the surface properties and result in smaller quantities of immobilized BSA and thus avidin. Nevertheless, the amount of functional avidin on the micropatterned surface suffices for the purpose of our work.

Apparently, avidin maintains its capacity for binding biotin even after acetone washing and micropatterning procedure, as evidenced by biotin-fluorescein binding. Given these positive results, this protocol, making use of BSA-biotin to form the avidin pattern, was used for the subsequent studies with supported lipid bilayers.

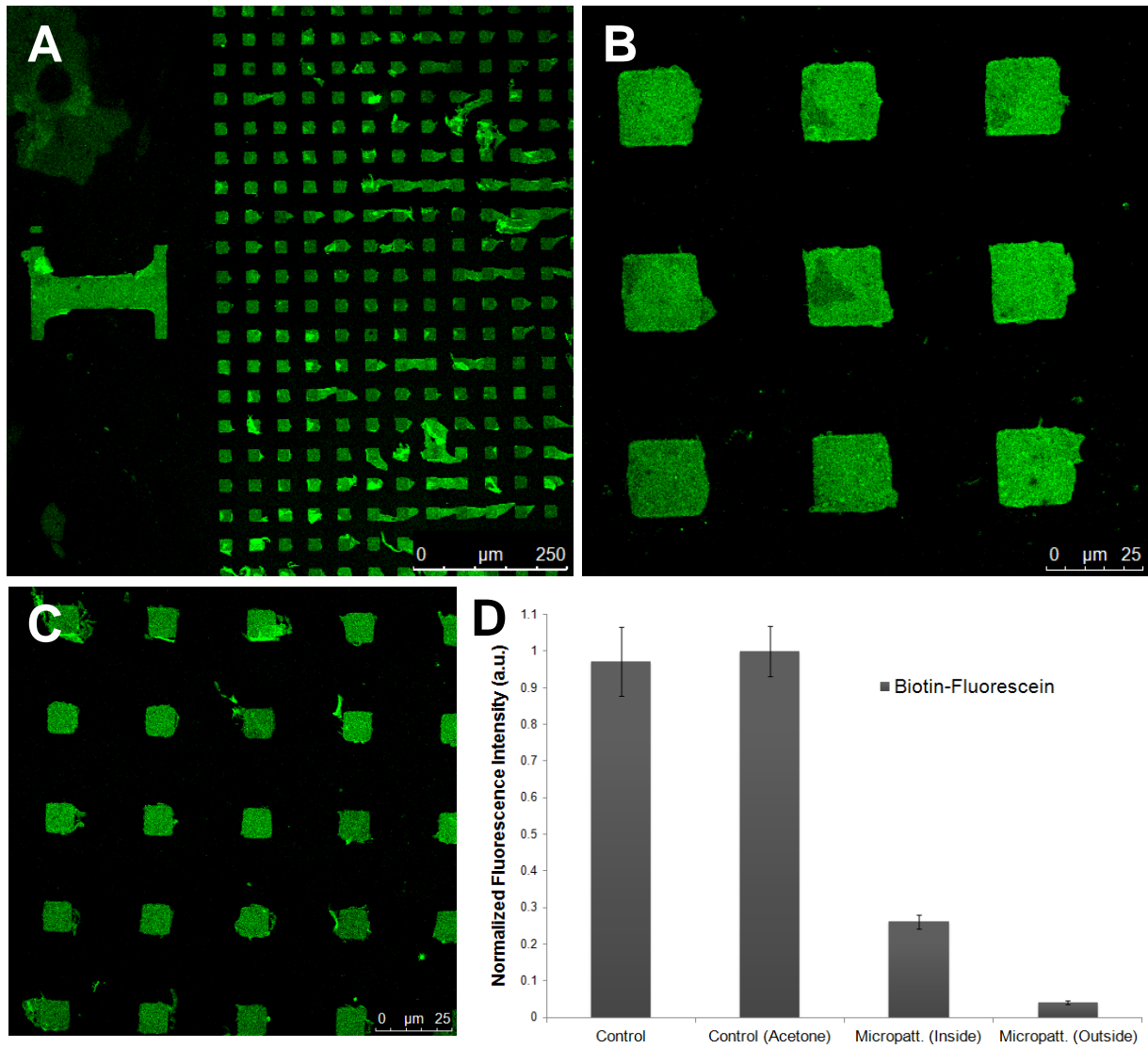


Figure 3.9 – Biotin-fluorescein binding to avidin after standard micropatterning fabrication. (A) Avidin micropatterning revealed after biotin-fluorescein. The roman numeral which identifies which pattern, out of nine possible patterns, is under observation is shown on the left. (B), (C) Avidin micropatterning showing 20 μm and 10 μm side squares (20% total protein-coated area), respectively. (D) Bar plot showing normalized fluorescence intensity \pm standard deviation for a control (non-micropatterned BSA-biotin and avidin-coated glass coverslip), for a control after acetone washing and inside and outside micropatterned regions. Fluorescence intensity from the controls was collected from different areas of the coverslip surface and averaged from at least 3 representative images of the surface; in the micropatterned samples, it was collected from several ROIs defined either inside or outside avidin-enriched regions – all intensities were normalized for the maximum fluorescence observed. Fluorescence is from biotin-fluorescein, which was added to the coverslips at 50 $\mu\text{g}/\text{mL}$ concentration. Unlabeled BSA-biotin and avidin were added at 0.1 mg/mL concentration.

3.2. FORMATION OF SUPPORTED LIPID BILAYERS FROM SMALL UNILAMELLAR VESICLES

3.2.1. Effect of avidin micropatterning in the formation and organization of supported lipid bilayers containing a ternary lipid mixture of POPC, Chol and PSM

The second part of the work focused on the formation of supported lipid bilayers from SUVs onto the previously created avidin micropatterning to evaluate the effect of protein adhesions to these membranes. As a first approach, we studied the behavior of SLB composed of a ternary lipid mixture containing POPC, Chol and PSM onto a cleaned glass coverslip; this mixture had potential to separate lipid phases into L_o (enriched mostly in saturated lipid, such as PSM and Chol) and L_d phase (enriched mostly in unsaturated lipids, such as POPC) (12). Rhod-DOPE has been shown to have a preference for L_d phase (126) and was used as a marker of this phase; NBD-DPPE has shown a slight preference for L_o phase and was used to partially mark L_o phase and to identify membrane formation (127). Indeed, when SUVs were added to glass substrate, a supported lipid bilayer was formed and phase separation was observed under the microscope (Figure 3.10). Intensity measurements on both phases

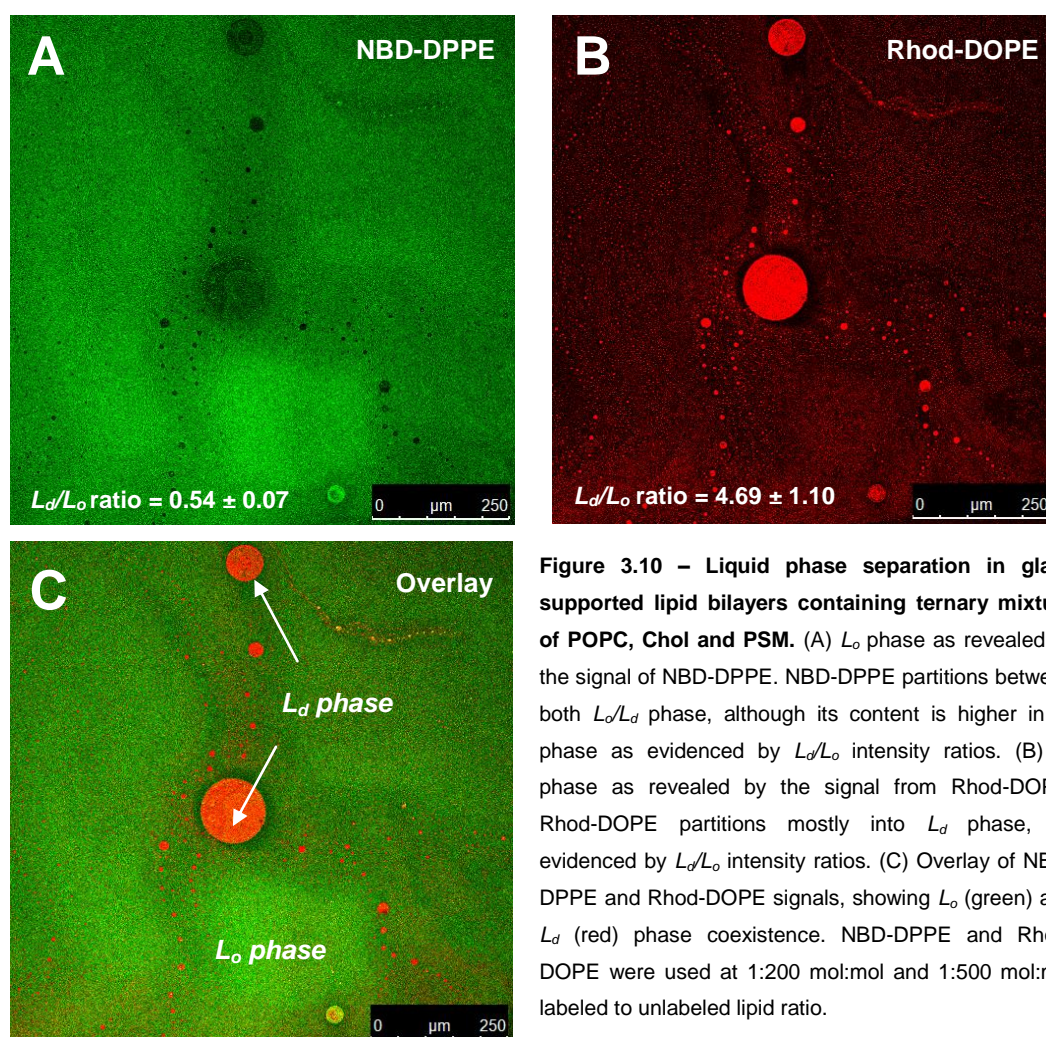


Figure 3.10 – Liquid phase separation in glass supported lipid bilayers containing ternary mixture of POPC, Chol and PSM. (A) L_o phase as revealed by the signal of NBD-DPPE. NBD-DPPE partitions between both L_o/L_d phase, although its content is higher in L_o phase as evidenced by L_d/L_o intensity ratios. (B) L_d phase as revealed by the signal from Rhod-DOPE. Rhod-DOPE partitions mostly into L_d phase, as evidenced by L_d/L_o intensity ratios. (C) Overlay of NBD-DPPE and Rhod-DOPE signals, showing L_o (green) and L_d (red) phase coexistence. NBD-DPPE and Rhod-DOPE were used at 1:200 mol:mol and 1:500 mol:mol labeled to unlabeled lipid ratio.

show that our results are consistent with the literature: NBD-DPPE signal was approximately twice as intense in L_o when compared to L_d phase (Figure 3.10 - A), while Rhod-DOPE was almost five times more enriched in L_d phase (Figure 3.10 - B) (126). Phase separation was observed, with the existence of circular L_d domains of different sizes (Figure 3.10 - C). The amount of each phase ($\approx 86/14\%$ L_o/L_d) was consistent with predictions by the ternary diagram used to prepare the lipid mixture (24).

Having verified phase coexistence using this mixture, the next step aimed to study the effect of avidin micropatterning, fabricated using BSA-biotin and avidin (see section 3.1.4, Figure 3.7), on the distribution and organization of both L_o and L_d phases. We first used the previous ternary lipid mixture as a control – in this system, no lipid component has any affinity for avidin. The results show that NBD-DPPE seemed to co-localize with avidin-enriched regions, while Rhod-DOPE was partially excluded from these regions, as is evident by the ratio between inside and outside protein-enriched regions obtained for both NBD and Rhod (Figure 3.11 - A, B, C). Our first expectation was that phase separation would occur, but L_o and L_d phase would not preferably co-localize in any region of the surface, since there is no membrane component with special affinity for any region. In fact, while interpreting the results one could be led to think that L_o phase was formed inside avidin-enriched regions, while L_d phase remained outside these regions. A more quantitative analysis of these results show that the fluorescence of NBD-DPPE is highly dependent on avidin concentration, while the fluorescence of Rhod-DOPE is not (Figure 3.11 – G, H). This suggests that the differences in fluorescence intensity inside and outside protein-coated surfaces are not associated with phase separation.

On the other hand, when biotinylated lipid was included at 0.1% both the signal of Rhod-DOPE and NBD-DPPE accumulated on avidin-coated surfaces, as evidenced by ratio measurements, suggesting a more efficient SUV deposition/interaction with these areas (Figure 3.11 – D, E, F). The correlation plot shows that the signal of both these lipids is dependent on avidin concentration when biotinylated lipid is incorporated (Figure 3.11, G, H). These results seem to indicate that SUV interaction with BSA-biotin/avidin-coated surfaces is effective in the presence of this lipid, leading to a higher number of vesicles adhered to these regions - this justifies Rhod-DOPE higher signal and correlation when compared with the control experiment (in the absence of biotinylated lipid). The very high NBD-DPPE fluorescence levels observed on protein-coated surfaces both in the absence and presence of biotinylated lipid are likely related with some binding of this phospholipid to BSA as NBD-labeled lipids have been shown to bind to BSA ($K_a \approx 10^6 \text{ M}^{-1}$) (128, 129). It should be noted that NBD-labeled lipids bound to BSA might exhibit superior fluorescence intensity than when incorporated within lipid bilayers with Rhod-DOPE, as a result of FRET alleviation. The next studies aimed to characterize the impact of protein-coating in the formation of supported lipid bilayers with a less complex lipid mixture.

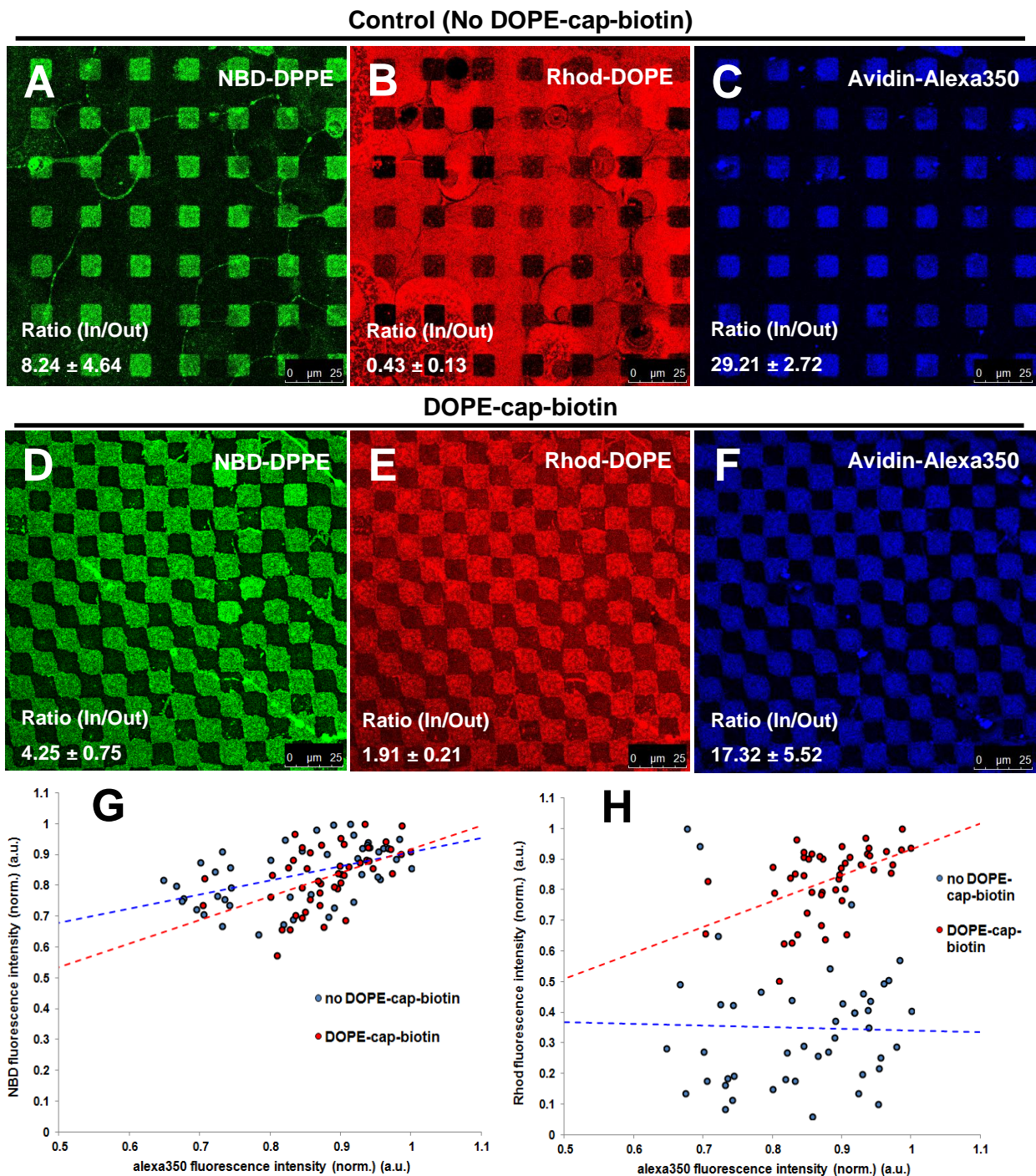


Figure 3.11 – Effect of avidin micropatterning on glass in the formation and organization of supported lipid bilayers from SUVs composed of a ternary mixture of POPC, Chol and PSM. (A),(B),(C) NBD-DPPE, Rhod-DOPE and avidin-Alexa350 fluorescent signal, respectively, with ternary control mixture (in the absence of DOPE-cap-biotin). Each of the corresponding intensity ratio between inside and outside avidin-enriched regions is shown. By comparing the different signals, we can observe that NBD-DPPE co-localized with avidin micropatterning; Rhod-DOPE was partially excluded from avidin-enriched regions. (D),(E),(F) NBD-DPPE, Rhod-DOPE and avidin-Alexa350 fluorescent signal, respectively, with ternary mixture containing DOPE-cap-biotin. Each of the corresponding intensity ratio between inside and outside avidin-enriched regions is shown. We observed that NBD-DPPE co-localized again with avidin micropatterning; Rhod-DOPE shifted towards avidin-enriched regions when compared with control experiment. Fluorescence is from NBD-DPPE (1:200 mol:mol), Rhod-DOPE (1:500 mol:mol) and avidin-Alexa350 (1:25 mol:mol). (G), (H) Correlation plot showing normalized fluorescence intensity of NBD and Rhod versus alexa350 fluorophores, respectively, each in the absence and presence of biotinylated lipid. Each point represents a ROI defined only on avidin-enriched regions; a minimum of 40 ROIs per plot were defined this way. BSA-biotin was added at 0.1mg/mL and avidin at 1 mg/mL. Avidin micropatterning was fabricated according to section 3.1.4.

3.2.2. Formation of supported lipid bilayers from POPC SUVs onto BSA-coated glass substrate

Given the results obtained in the previous experience, we tried to evaluate whether or not we could form a continuous supported lipid bilayer onto a simple non-micropatterned BSA-coated glass surface. We prepared SUVs from a single mixture of POPC, using NBD-DPPE or Rhod-DOPE as a membrane marker (in the absence of biotinylated lipid) and added to clean (uncoated) and BSA-coated glass coverslips.

Results from the control (uncoated, clean glass surface) showed a surface with homogeneous fluorescence; the presence of a supported lipid bilayer was confirmed by FRAP experiments (Figure 3.12 – A, B, C). We obtained a diffusion coefficient of $1.70 \pm 0.26 \mu\text{m}^2/\text{s}$ for Rhod-DOPE (Figure 3.12 – D), which is in agreement with literature - $1.80 \pm 0.20 \mu\text{m}^2/\text{s}$ obtained for Rhod-DOPE on a glass-supported POPC membrane (130); for NBD-DPPE, we obtained a diffusion coefficient of $1.30 \pm 0.22 \mu\text{m}^2/\text{s}$ (Figure 3.12 - E), which is close to that obtained for Rhod-DOPE. In both cases, total recovery was observed, indicating a 100% mobile lipid fraction, suggesting a well-formed, defect-free supported membrane.

Results from the BSA-coated glass surface depicted a rather heterogeneous NBD-DPPE fluorescence distribution along the surface, in contrast with the homogenous distribution observed in supported lipid bilayers on cleaned glass. However, a similar fluorescence surface distribution, containing these heterogeneities, was observed with Rhod-DOPE (results not shown); since this labeled phospholipid did not show affinity towards BSA (Figure 3.11 – B), we attributed these heterogeneities to immobilized SUVs on the coverslip surface which failed to fuse. This pool of labeled phospholipids is expected to be fully immobile and no fluorescence recovery is expected on the FRAP experiments for these molecules.

In experiments performed on BSA-coated glass, we observed small bright patches, about twice as intense as the remaining surface and hypothesized that these were isolated supported lipid membrane patches (Figure 3.12 - F, G); these patches were also present when Rhod-DOPE was used as phase marker instead of NBD-DPPE (results not shown).

To confirm our hypothesis, we performed a FRAP experiment on the interface between these patches and the outside regions. If recovery occurred in all ROI area, then membrane would exist both in outside regions and inside patches; if recovery occurred partially in one of the regions, that region would be the only one containing a continuous supported membrane; if no recovery was observed, a continuous lipid membrane would not exist in either regions. Results indicate that there was fluorescence recovery only inside these patches, suggesting free lateral lipid diffusion within the membrane (Figure 3.12 – H, I, J), while most of the NBD-DPPE on the coverslip surface was fully immobile. Apparently, blocking the surface with BSA changes its properties in such a way that most SUVs cannot fuse with the surface and as a result no supported lipid membranes are formed. In cleaned glass at neutral pH (7.0 - 7.4), a great number of hydroxyl groups are usually available to interact with lipid polar heads ($\text{pK}_{\text{a(OH)}} = 7.1$, in silica) (131) and, in the presence of Ca^{2+} , which is

frequently used to stabilize negative hydroxyl groups or negative lipid head charges, vesicle adhesion and fusion is generally successful (83).

The results shown here confirm that the BSA-coated surface lacks the necessary hydrophilic character for vesicle fusion and supported membrane formation. In this way, some regions might be able to form small supported lipid bilayers, accounting for the patches observed, while most SUVs remain adsorbed on the surface without fusion and formation of SLBs. This accounts for the rather heterogeneous fluorescence observed outside the lipid patches. This hypothesis is also consistent with reports showing that electrostatic and Van der Waals interactions play a crucial role in vesicle fusion to the substrate (132) and also with the fact that SLBs on uncoated glass do not present these patches, but rather a homogeneous membrane throughout the surface. The next experiment attempted to form these bilayers onto an avidin-micropatterned glass substrate.

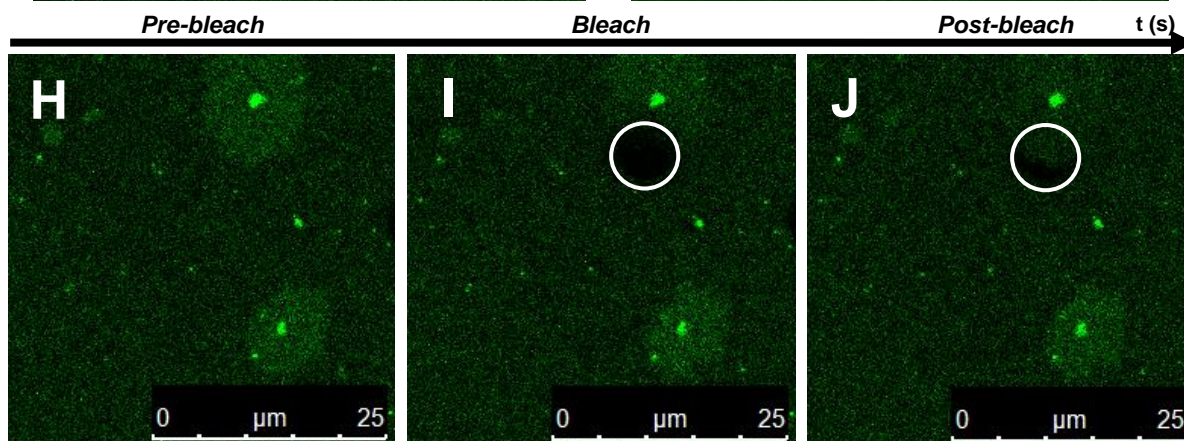
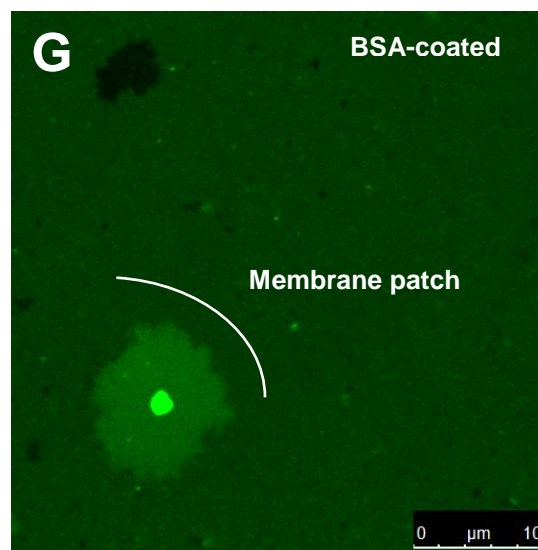
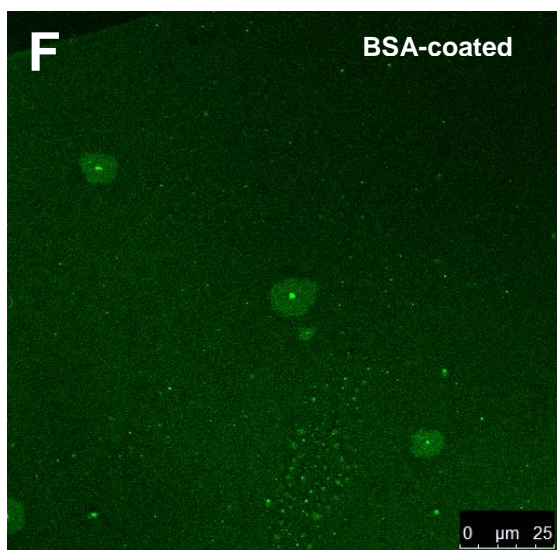
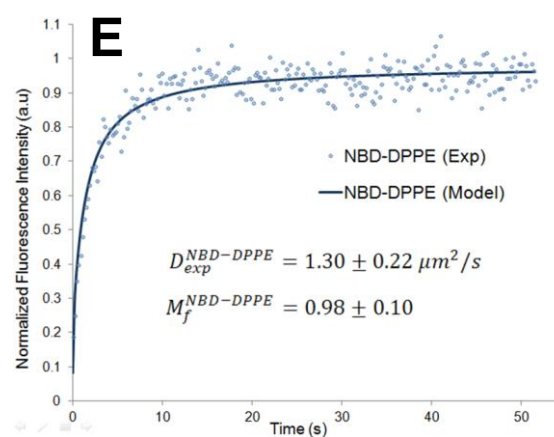
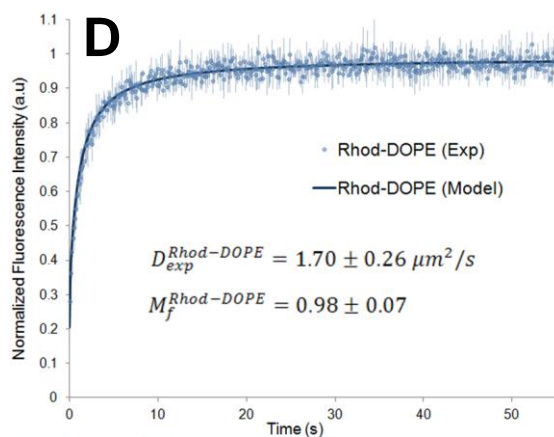
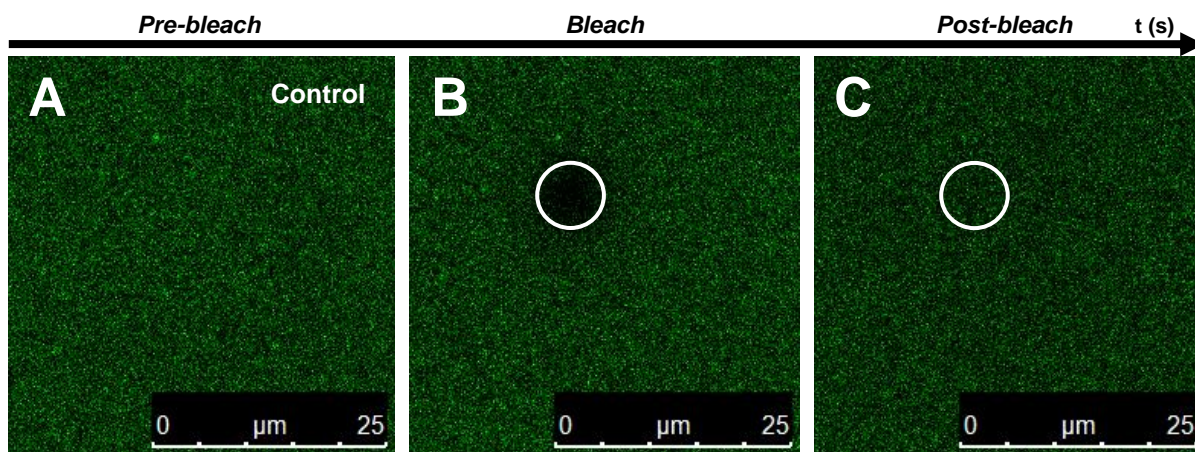


Figure 3.12 – Effect of BSA coating on the formation of glass supported lipid bilayers from POPC SUVs (in the absence of biotinylation). (A), (B), (C) Fluorescence recovery after photobleaching experiment onto glass supported lipid bilayer for control sample (not blocked with BSA) showing pre-bleach, bleach and post-bleach phase, respectively. (D), (E) FRAP curves (normalized fluorescence intensity over time) obtained for NBD-DPPE and Rhod-DOPE respectively, showing the recovered diffusion coefficient D and mobile fraction M_r for each. (F), (G) Fluorescence across the glass surface blocked with BSA. Small independent patches of lipid membranes were observed and confirmed by FRAP experiments. (H), (I), (J) FRAP experiment performed on the borders of a membrane patch, showing NBD-DPPE pre-bleach, bleach and post-bleach phases respectively; recovery was observed only inside the bright patch. In either confocal imaging or FRAP experiments, Fluorescence is from NBD-DPPE. NBD-DPPE or Rhod-DOPE were used at 1:200 mol:mol or 1:500 mol:mol labeled to unlabeled lipid ratio. BSA was added at 0.1 mg/mL concentration.

3.2.3. *Formation of supported lipid bilayers from POPC SUVs onto avidin-micropatterned glass substrate*

Since BSA was shown to prevent supported bilayer formation on glass, the next studies aimed to elucidate whether a continuous SLB could be formed onto avidin micropatterned surface in the absence of liposome biotinylation. After the micropatterning was completed by standard procedure using BSA-biotin and avidin (see section 3.1.4, Figure 3.7), we blocked one of the samples with BSA, while the other remained unblocked; in this way, BSA would be coating the glass regions outside the avidin-enriched regions and any effect observed inside these regions could be attributed to avidin and not to BSA. We used the same mixture of POPC and NBD-DPPE as in the previous experience.

In the sample without BSA blocking, results show that the lipid was mainly present outside micropatterned regions, as indicated by ratio measurements (about 3 times more fluorescence intensity outside). This was expected given the results previously obtained for the ternary lipid mixture, and confirms that SUVs prefer the glass-exposed regions to the protein-coated areas (Figure 3.13 – A, B, C).

Results for the sample where coverslip exposed areas were blocked with an additional 0.1 mg/mL BSA show, on the other hand, that NBD-DPPE co-localized again with avidin-enriched regions, as indicated by imaging and intensity ratios (about 13 times more intense inside avidin regions) (Figure 3.13 - D, E, F). Since we used a POPC mixture, which had no potential to phase separate, NBD-DPPE enrichment in these regions was surely not related to lipid mixture and phase separation; additionally, biotinylated lipid is absent from the experiment and no membrane component was expected to have affinity towards these regions. These results seem to suggest that the inclusion of avidin in the surface strongly promotes the adsorption of SUVs to the protein surface when compared to BSA, likely as a result of the different electrostatic properties of avidin and BSA.

To further elucidate these results, FRAP experiments were performed both in the unblocked and in BSA-coated micropatterned surfaces to test for the presence of an immobilized pool of NBD-DPPE. One needs to be careful when performing FRAP experiment on limited surfaces such as avidin-enriched regions – because the total area is limited, the quantity of fluorescent lipid available to diffuse to the bleached spot is also limited; since the FRAP 2D model assumes an infinite area available for recovery outside the bleached spot (see section 2.5.2), diffusion coefficients may be underestimated.

Nonetheless, the avidin-enriched area is about 20 times larger than the bleached ROI area, which was large enough to infer about the actual mobile fraction available ($\text{area}_{\text{bleached}} \approx 20 \mu\text{m}^2$, $\text{area}_{20\mu\text{m square}} = 400 \mu\text{m}^2$).

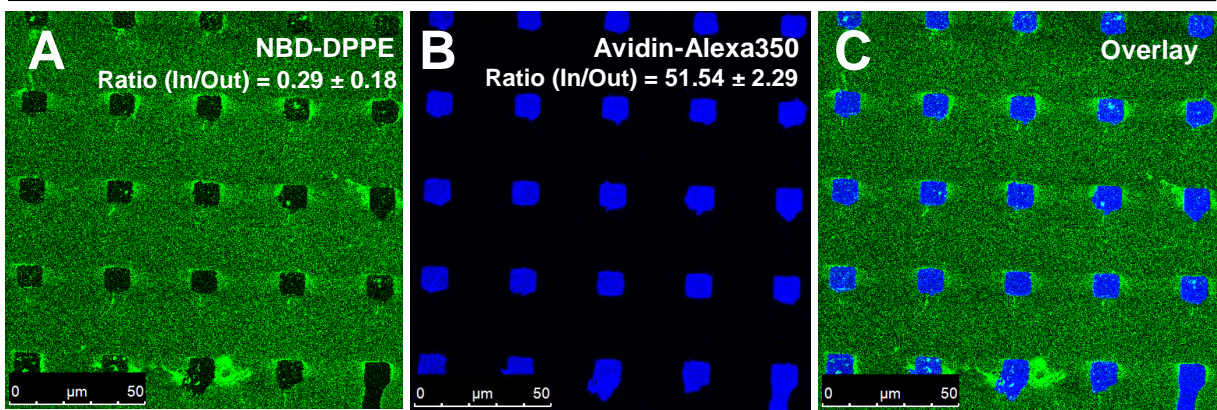
FRAP results for the sample without BSA blocking show that a continuous supported lipid membrane existed, in some regions, outside the avidin regions (Figure 3.13 – G), indicating that this surface does not prevent formation of SLBs from SUVs even after micropatterning procedure and that an immobilized pool of NBD-DPPE is negligible in the absence of BSA coating. We recovered a diffusion coefficient of $0.84 \pm 0.08 \mu\text{m}^2/\text{s}$, which is slightly lower than the previously obtained in non-micropatterned glass; this difference in diffusion might have to do with (i) the substrate, which in this case is modified during the micropatterning procedure, rendering the surface more hydrophobic and affecting lipid mobility when compared with clean glass; (ii) an incomplete membrane, which lead to an underestimation of the diffusion coefficient.

On the other hand, results for the BSA-blocked surface show the presence of both a mobile (17% of total lipid) and an immobile (83%) fraction of labeled lipid on the SLB within avidin-coated regions (Figure 3.13 – H). The mobile lipid population moved with a diffusion coefficient of $D = 0.49 \pm 0.23 \mu\text{m}^2/\text{s}$. The low diffusion coefficient obtained (when compared with the previous experiment, section 3.2.2) could be explained by defective membranes which impaired normal lateral lipid diffusion. Identical results were obtained for samples not blocked with BSA (not shown), suggesting that SLBs cannot properly form onto avidin-enriched regions.

The results obtained here for the sample not blocked with BSA differ from the experiment shown on Figure 3.11 – A with a ternary mixture, where higher NBD-DPPE signal is seen inside avidin-coated areas, again in the absence of BSA blocking. As already discussed, in that experiment Rhod-DOPE was also included in the lipid mixture leading to NBD-DPPE quenching in the membrane outside these regions. It is possible that the higher NBD fluorescence measured then in the avidin-coated regions (where no lipid membrane was present) was solely due to FRET alleviation when the labeled phospholipid bound to surface BSA. In the case of the experiment presented here, on Figure 3.13 – A-C, since no Rhod-DOPE was included, insertion of NBD-DPPE into surface BSA would lead instead to a decrease in quantum yield as shown elsewhere (128).

Thus, it is confirmed that with the standard methods it is not possible to form SLBs in a protein-coated surface. Importantly, the adsorption of SUVs to surfaces containing BSA or BSA-biotin + avidin is shown to be significantly different, probably as a result of different electrostatic properties of both proteins. The next studies aimed to optimize a different methodology for the generation of supported membranes onto protein-coated surfaces.

No BSA



0.1 mg/mL BSA

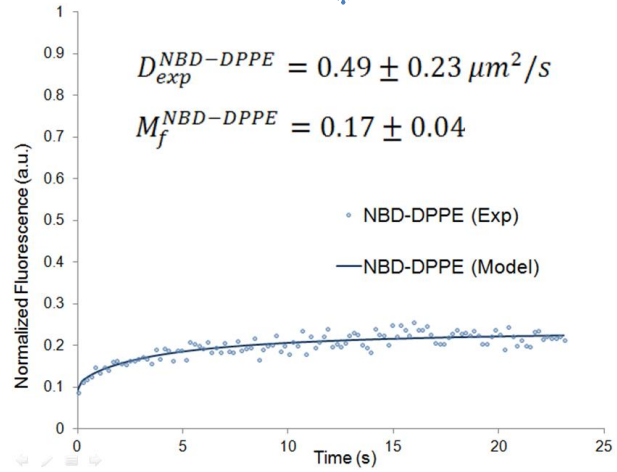
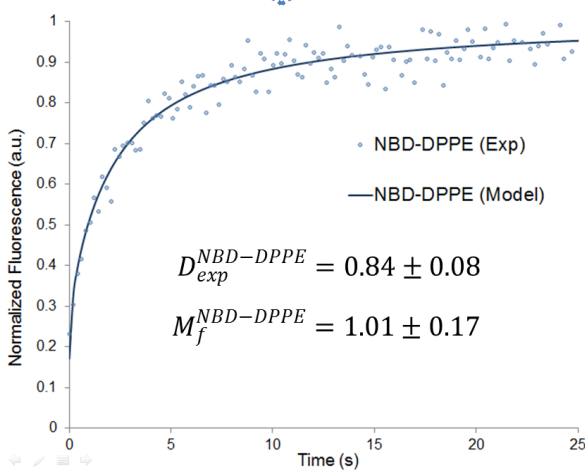
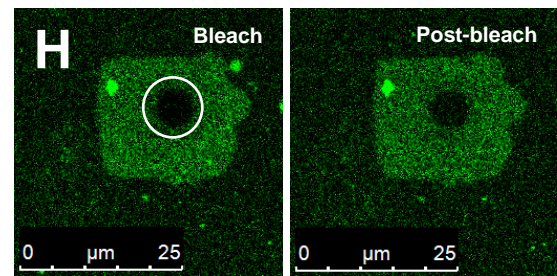
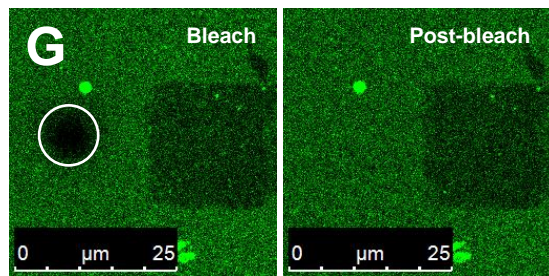
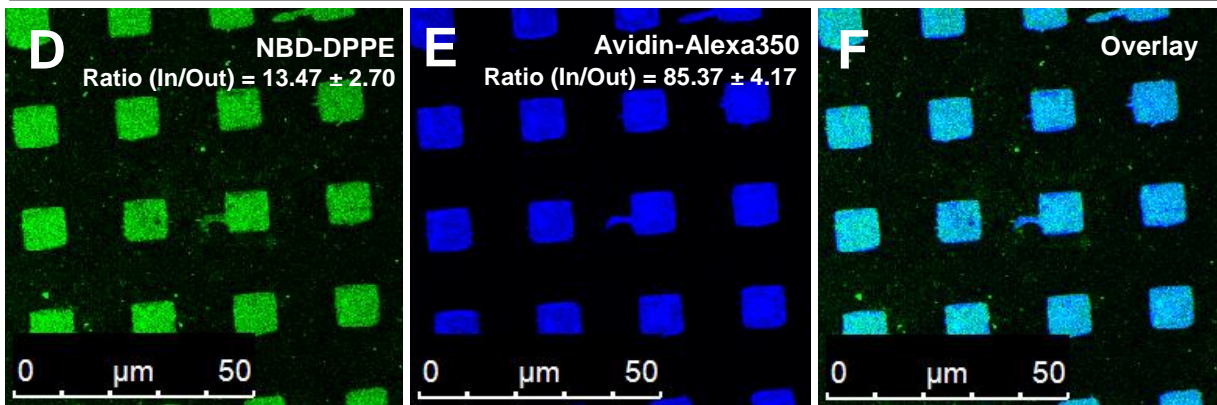


Figure 3.13 – Effect of avidin micropatterning on the formation of supported lipid bilayers from POPC SUVs (in the absence of biotinylation). (A), (B), (C) Avidin micropatterning showing NBD-DPPE fluorescent signal, avidin-Alexa350 fluorescent signal and overlay between the two for the sample not blocked with BSA; exclusion of NBD-DPPE from avidin-enriched regions was observed. (D), (E), (F) Avidin micropatterning showing NBD-DPPE fluorescent signal, avidin-Alexa350 fluorescent signal and overlay between the two for the sample blocked with additional 0.1 mg/mL BSA; NBD-DPPE signal is enriched in avidin-enriched regions. (G), (H) FRAP curve (normalized fluorescence over time) for NBD-DPPE outside the avidin-enriched regions (in glass) for the sample not blocked with BSA and inside avidin-enriched regions in BSA-blocked sample, respectively. Diffusion coefficient D and mobile fraction M_f are also shown. NBD-DPPE and avidin-Alexa350 were used at 1:200 and 1:12 labeled to unlabeled lipid and protein ratio, respectively. Avidin pattern was fabricated according to section 3.1.4., Figure 3.17. BSA-biotin and avidin were added at 1 mg/mL concentration and BSA was added at 0.1 mg/mL concentration.

3.2.4. Effect of temperature in the formation of supported lipid bilayers from POPC SUVs onto BSA and BSA-biotin/avidin-coated glass substrate

Initially, we studied if temperature was able to induce the formation of SLBs containing POPC, DOPE-cap-biotin (1:1000 mol:mol) and Rhod-DOPE (1:500 mol:mol), onto BSA and BSA-biotin/avidin-coated glass coverslips. Biotinylated lipid was included in order to immobilize a higher number of vesicles onto BSA-biotin/avidin surface, thus enhancing SUV fusion potential. SUVs were prepared in liposome fusion buffer at the desired temperature, either 25°C or 60°C, and added to the substrate as described in Materials and Methods (section 2.3.2).

The results from BSA-coated glass showed a very heterogeneous fluorescence both at room temperature and 60°C (Figure 3.14 - A, B). The characteristic membrane patches from the BSA-coated surface were confirmed by FRAP experiments (Figure 3.14 - E), suggesting that high temperature had no apparent effect on the formation of a uniform, defect-free supported lipid membrane.

The results from glass coated with BSA-biotin and avidin did not show supported membrane patches, but rather a more intense and homogeneous fluorescence distribution, although with some bright fluorescent spots, both at room temperature and 60°C (Figure 3.14 - C, D). This was expected since DOPE-cap-biotin was present in the SUV mixture, providing very high affinity towards the avidin surface. The bright spots observed in the surface are likely corresponding to a large number of vesicles clustered in the same area of the surface. Surprisingly, FRAP experiments showed that almost no place on the surface contained a properly-formed SLB since almost no fluorescence recovery was observed. However, for the sample heated to 60°C, we were able to extract diffusional parameters, showing that about 20% of Rhod-DOPE was mobile, diffusing with a coefficient of $3.10 \pm 1.20 \mu\text{m}^2/\text{s}$ (Figure 3.14 - F). The diffusion coefficient, although within error or literature value for Rhod-DOPE (130), has a very high associated error, which can be explained by the fact that, when measuring diffusion by FRAP, low mobile lipid fractions are subject to more error, which in turn leads to a poorer fit of the 2D diffusion model to the experimental data. Nevertheless, temperature does not seem to produce a significant effect on vesicle fusion, even if a high number of them are previously immobilized on the surface through DOPE-cap-biotin.

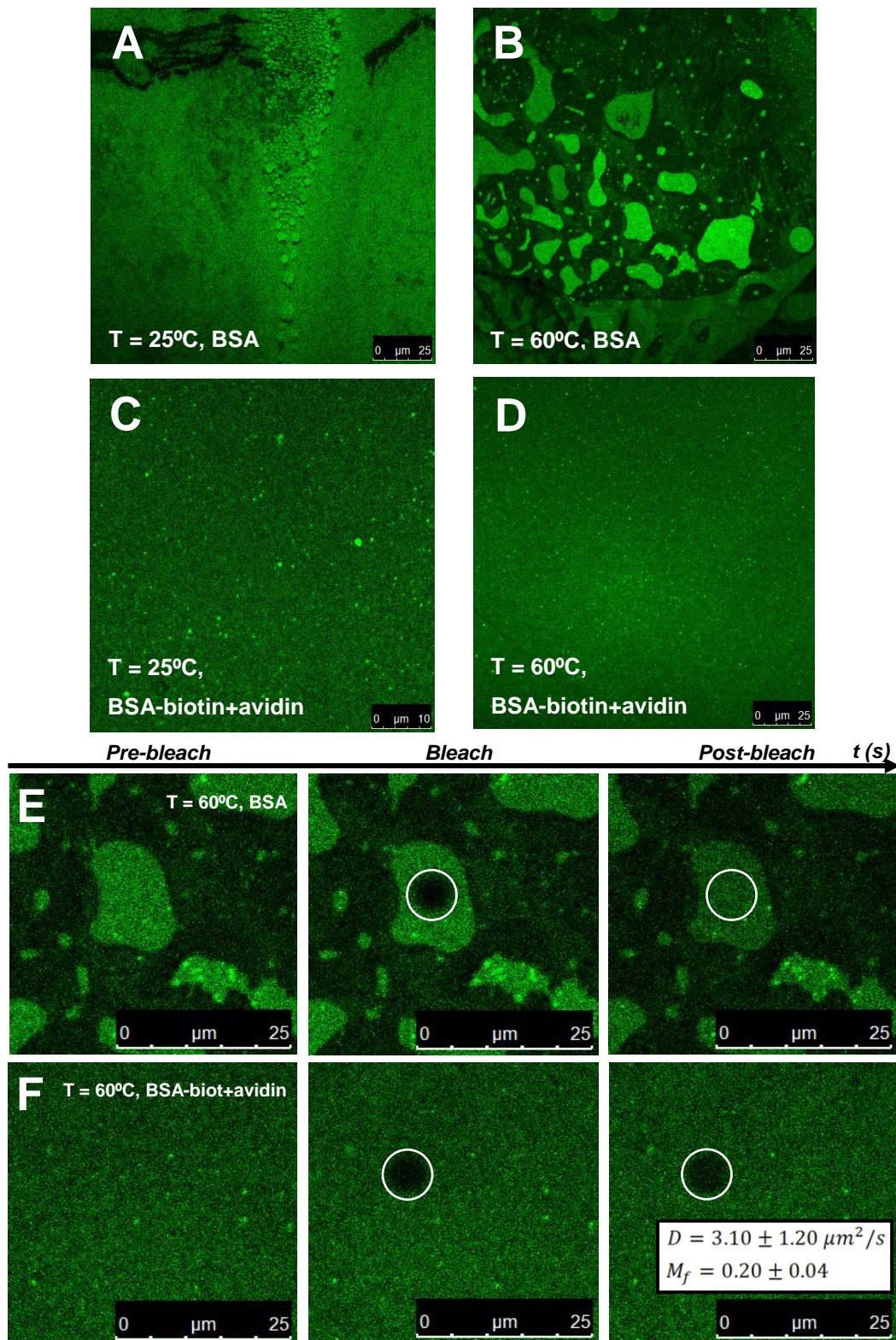


Figure 3.14 – Effect of temperature in the formation of supported lipid bilayers from POPC SUVs containing biotinylated lipid onto BSA and BSA-biotin/avidin coated glass substrate. (A) Rhod-DOPE fluorescence in BSA-coated surface at room temperature (25°C). (B) Rhod-DOPE fluorescence in BSA-coated surface at 60°C. (C) Rhod-DOPE fluorescence in glass surface blocked with BSA-biotin plus avidin at 25°C. (D) Rhod-DOPE fluorescence in glass surface blocked with BSA-biotin plus avidin at 60°C. (E) FRAP experiment performed on a lipid membrane patch in BSA-coated surface at 60°C. (F) FRAP experiment performed on BSA-biotin and avidin-coated surface at 60°C and the corresponding Rhod-DOPE diffusion coefficient D and mobile fraction M_f ; FRAP curve is not shown. Both in (E) and in (F) a representative image of pre-bleach, bleach and post-bleach phase are shown. Rhod-DOPE and DOPE-cap-biotin were used at 1:500 and 1:1000 labeled to unlabeled lipid ratio, respectively. Unlabeled BSA, BSA-biotin and avidin were added at 1 mg/mL concentration.

3.2.5. Effect of poly (ethylene glycol) in the formation of supported lipid bilayers from POPC SUVs onto avidin-coated glass substrate

To try to force vesicle fusion on BSA-biotin/avidin-coated surface, we made use of PEG as a fusion agent of lipid vesicles, as this strategy had been previously shown to work (133). We used the same mixture as before, containing POPC, DOPE-cap-biotin (1:1000 mol:mol) and Rhod-DOPE (1:500 mol:mol) as a membrane marker. After incubation and vesicle adhesion, we incubated each glass coverslip containing adsorbed vesicles with concentrated PEG 3400 (30% w/v) in fusion buffer solution at different times (5, 10 and 20 minutes); after this step, they were copiously washed and treated similarly to previous experiments for microscope observation. Since PEG is a long-chain polymer with the ability to retain large quantities of water, this would result in dehydration of lipid bilayer surface and a more favorable vesicle-vesicle interaction, eventually leading to liposome fusion and formation of SLBs. Results showed a distribution of fluorescence not so different from the obtained for in the previous experiments, for all PEG incubation times (Figure 3.15 – A - D). FRAP experiments showed that no fluorescence recovery occurred in most of the surface, suggesting the absence of a properly-formed SLB even after PEG incubation for 20 minutes (Figure 3.15 - D). In contrast with literature (133), PEG had no distinct effect on SUV fusion when compared with control experiments.

Altogether, results suggest that SUVs are highly stable when adsorbed to the protein-coated surface and do not tend to fuse with each other. Given these results, we changed our approach to the problem and attempted to use another method of forming SLBs that did not rely on SUVs, but rather made use of giant unilamellar vesicles (GUVs) - the third part of the work describes various experiences based on this strategy.

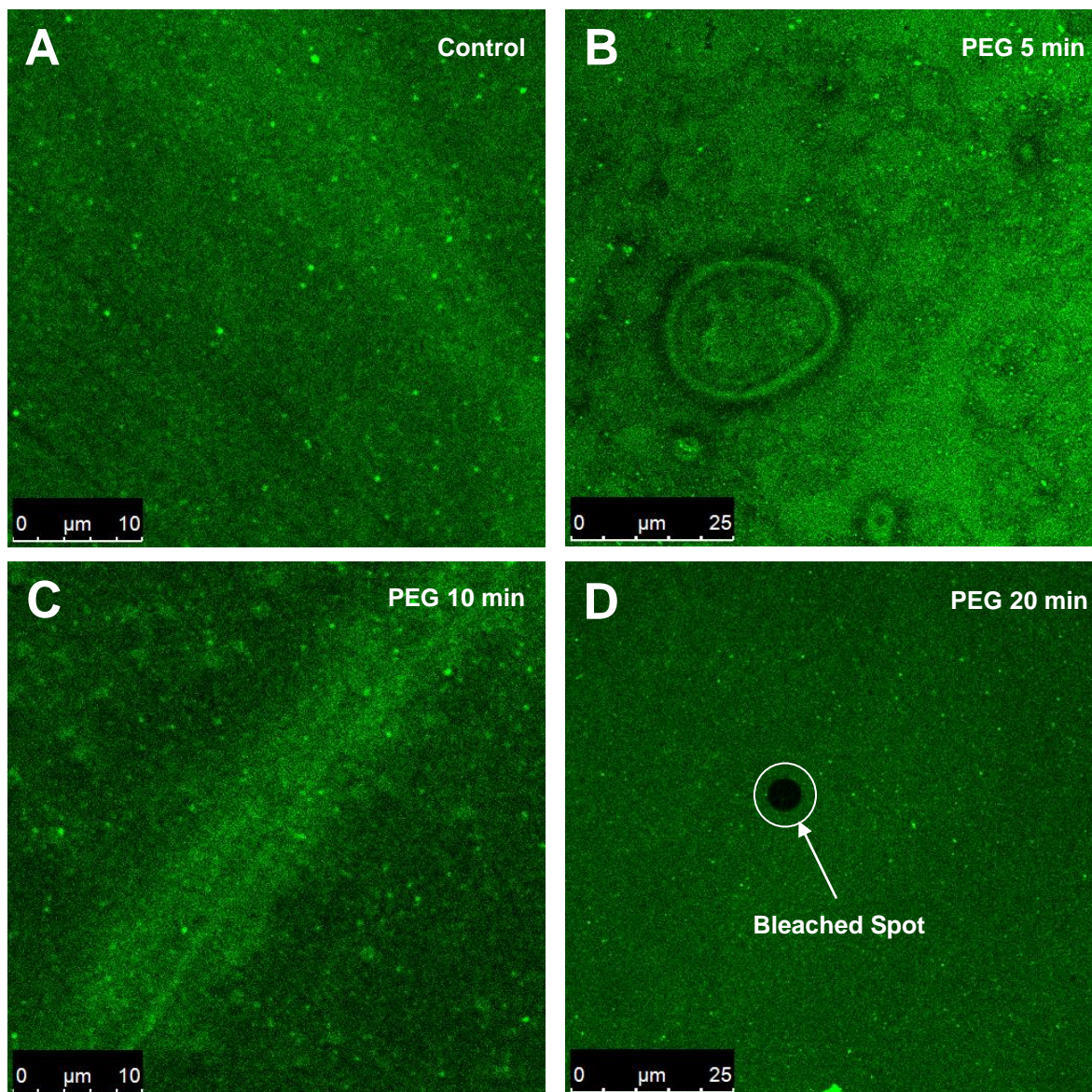


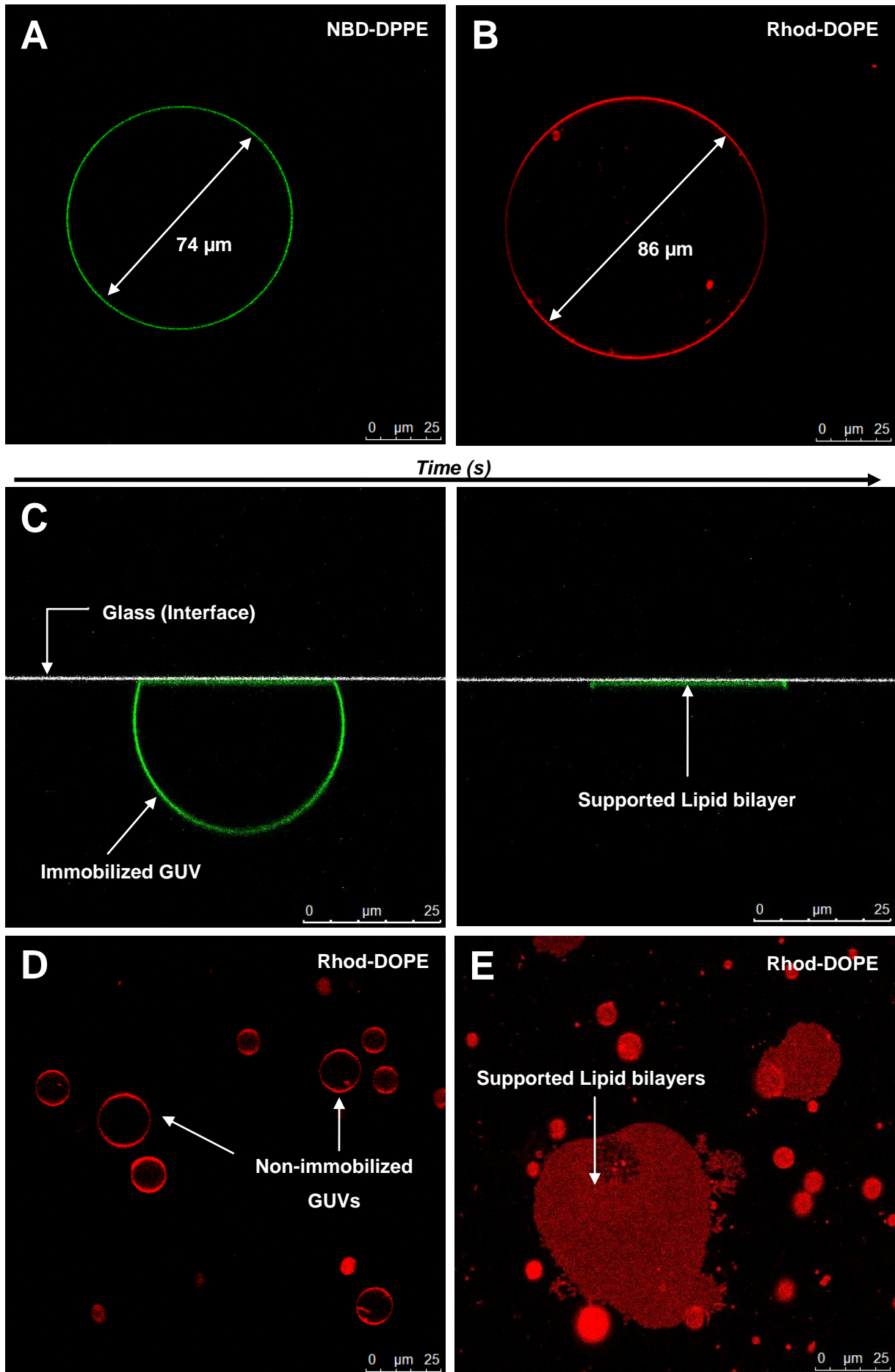
Figure 3.15 – Effect of PEG in the formation of supported lipid bilayers from POPC SUVs containing biotinylated lipid onto BSA-biotin and avidin-coated glass coverslips. (A) Rhod-DOPE fluorescence in glass substrate coated with BSA-biotin and avidin, without PEG incubation (control). (B) Rhod-DOPE fluorescence in glass substrate coated with BSA-biotin and avidin, after 5 minutes of incubation with PEG. (C) Rhod-DOPE fluorescence in glass substrate coated, after 10 minutes of incubation with PEG. (D) Rhod-DOPE fluorescence in glass substrate coated with BSA-biotin and avidin, after 20 minutes of incubation with PEG. The marked spot is the bleaching spot after FRAP experiment, showing no fluorescence recovery. Rhod-DOPE and DOPE-cap-biotin were used at 1:500 and 1:1000 labeled to unlabeled lipid ratio, respectively. BSA, BSA-biotin and avidin were added at 1 mg/mL concentration.

3.3. FORMATION OF SUPPORTED LIPID BILAYERS FROM GIANT UNILAMELLAR VESICLES

3.3.1. *Formation of supported lipid bilayers from GUVs onto avidin-coated Ibidi glass bottom slides*

The diameter of giant unilamellar vesicles typically exceeds several micrometers (75), making them less stable than SUVs vesicles when tethered to a surface. In fact, the host laboratory has already shown that a significant GUV membrane fraction adheres and spreads onto an avidin-blocked surface, even when the ratio of DOPE-cap-biotin present in lipid mixture is as low as 10^{-6} of the total lipid (80). Making use of this data, we pretended to form supported lipid bilayers using GUVs, which would adhere to the avidin-coated surface and eventually burst, forming supported lipid bilayers. We prepared a simple mixture of POPC, biotinylated lipid (DOPE-cap-biotin, 1:1000 mol:mol) and either Rhod-DOPE (1:500 mol:mol) or NBD-DPPE (1:200 mol:mol) as a membrane marker and performed electroformation, according to Materials and Methods (section 2.3.3) to form giant vesicles.

We first checked the quality of the electroformations in Ibidi uncoated slides under the confocal microscope. Both GUVs formed with NBD-DPPE and Rhod-DOPE as fluorescent labels proved to be unilamellar and have large sizes, almost reaching 100 μm diameter (Figure 3.16 - A, B); in some cases, lipid residue could be identified inside the vesicle, possibly remains from electroformation (Figure 3.16 - B). We then added the GUV solution to Ibidi glass bottom slides previously coated with either BSA-biotin and avidin or BSA (control). Following xz images over time, we were able to observe GUVs adherence and spreading in the avidin-coated surface due to the affinity of biotin towards avidin – because of this, the vesicles became unstable and collapsed, leaving a SLB onto the protein-coated surface (Figure 3.16 - C, E). It can be observed that the smaller GUVs didn't collapse, suggesting that the bigger GUVs were the ones who formed SLBs, possibly due to their greater instability when immobilized on the surface (Figure 3.16 - E). In BSA-coated glass surface, this protein has a repelling effect on these vesicles, which do not adhere to the surface as expected (Figure 3.16 - D). FRAP measurement confirmed the existence of an homogenous and defect-free supported lipid bilayer – we obtained a diffusion coefficient for Rhod-DOPE of $3.00 \pm 0.97 \mu\text{m}^2/\text{s}$ and a 100% mobile lipid fraction (Figure 3.16 - F). These results show that indeed a supported bilayer can be formed from GUVs onto an avidin-coated surface; however, the density of the GUVs in the surface was far too small for the purpose of our work. In the micropatterned system, we aimed to create a membrane all over the avidin-micropatterning so that we would have the largest membrane area available for our studies. Given the low density of GUVs that form SLBs, we pretended to answer three main questions: 1) Could we increase GUVs concentration in order to have more material available to form SLBs? 2) Could we induce or force GUV collapse onto avidin-coated glass to form SLBs? 3) Do supported lipid membranes formed from different GUVs fuse with each other, creating a larger membrane? These issues proved important and necessary to create a large, uniform lipid bilayer from GUVs onto avidin, similar to those formed from SUVs onto cleaned glass.



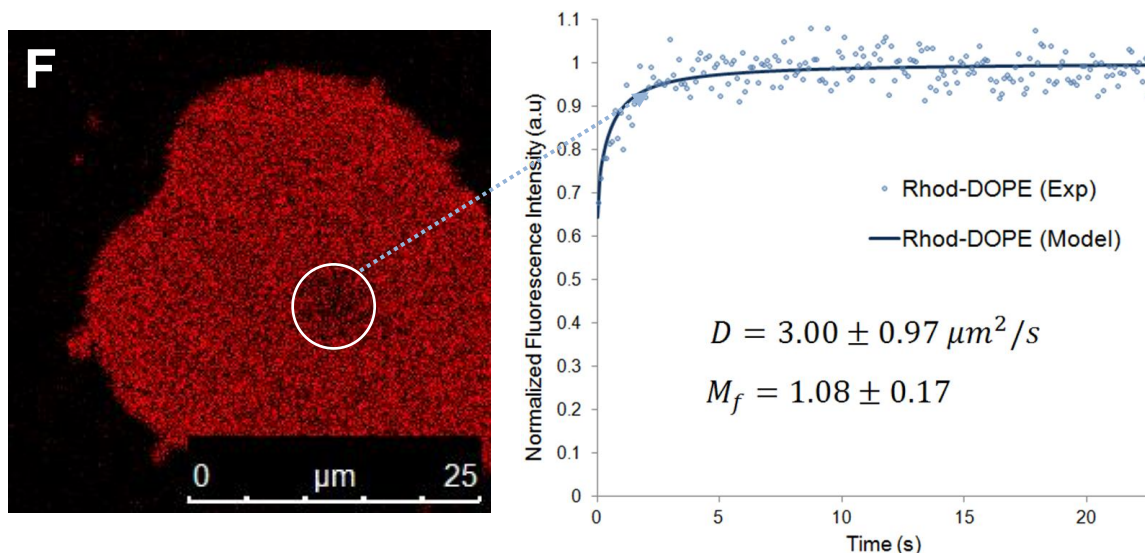


Figure 3.16 – Formation of supported lipid bilayer from GUVs containing a mixture of POPC, biotinylated lipid (DOPE-cap-biotin) and either NBD-DPPE or Rhod-DOPE as a membrane marker, in Ibidi glass bottom slides. (A) XY slice of a GUV labeled with NBD-DPPE in Ibidi uncoated glass slides. (B) XY slice of a GUV labeled with Rhod-DOPE in Ibidi uncoated glass slides. (C) XZ image sequence over time showing an immobilized GUV labeled with NBD-DPPE adhered to Ibidi glass bottom slides coated with BSA-biotin and avidin. After some time, the vesicle collapsed and formed a supported lipid bilayer. (D) XY slice of GUVs labeled with Rhod-DOPE in Ibidi glass bottom slides coated with BSA. (E) XY slice of GUVs labeled with Rhod-DOPE in Ibidi glass bottom slides coated with BSA-biotin and avidin; some of the GUVs collapsed and formed supported lipid bilayers. (F) FRAP experiment performed onto a SLB formed by GUV collapse; the FRAP curve (normalized fluorescence intensity over time) and the correspondent diffusion coefficient D and mobile fractions M_f are shown on the right. NBD-DPPE, Rhod-DOPE and DOPE-cap-biotin were used at 1:200 mol:mol, 1:500 mol:mol and 1:1000 mol:mol labeled to unlabeled lipid ratio. Unlabeled BSA, BSA-biotin and avidin were added at 1 mg/mL concentration.

3.3.2. GUV concentration by glucose/sucrose density difference deposition

In order to obtain a concentrated solution of GUVs, we used the same lipid mixture as in the previous experience, performing electroformations in sucrose solution (4 mL) and added glucose to this mixture to a total of 8 mL (see Materials and Methods, section 3.3.3). We let the solution rest overnight, so that GUVs would deposit in the bottom of the falcon tube due to density difference between inside sucrose and outside glucose. In the next day, we collected 6 different fractions from the solution: 8 – 6 mL, 6 – 4 mL, 4 – 2 mL, 2 – 1 mL, 1 – 0.5 mL and the last 500 μ L. 100 μ L of each fraction and an extra 300 μ L of glucose solution were added to an uncoated Ibidi slides and allowed to for 1 hour. From the representative images under the confocal microscope, we could observe that the last fraction (500 μ L) contained a much higher quantity of GUVs when comparing to the previous fractions, from 8 – 6 mL to 1 – 0.5 mL (Figure 3.17 - A, B, C, D). The GUVs in the last fraction were also bigger, which was expected, since deposition by density different is more effective for vesicles with higher dimensions. Representative images of each fraction were taken and total fluorescence intensity was averaged and normalized, showing a much higher fluorescence in the last 500 μ L (Figure 3.17 - E). We thus used this simple procedure to increase the concentration of GUVs in the next experiments.

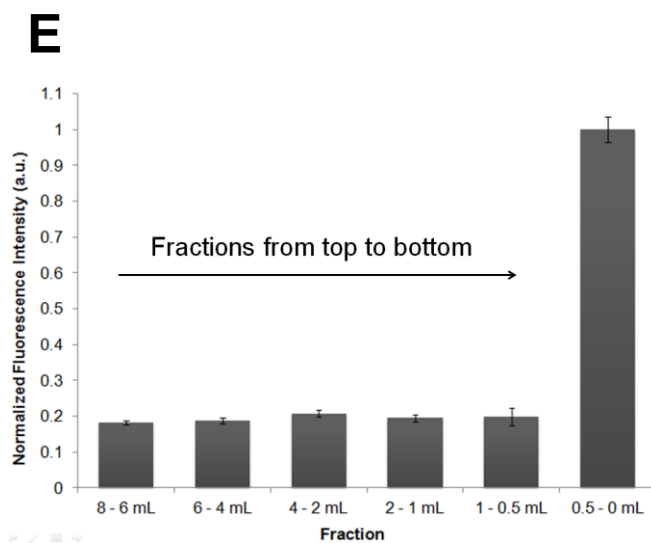
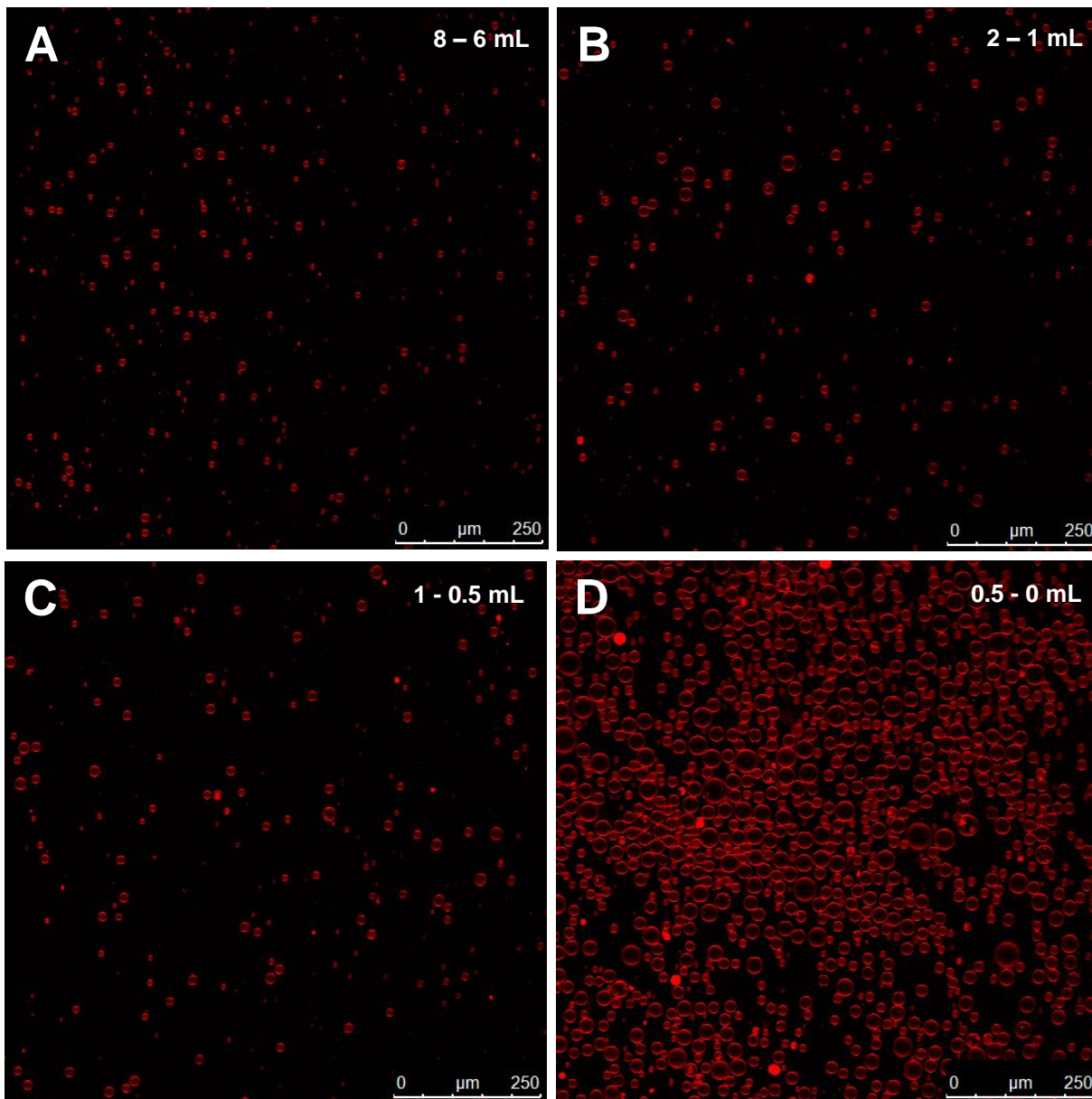


Figure 3.17 – POPC GUVs concentration in different volume fractions collected from an 8 mL glucose solution. (A) Representative image of the top fraction corresponding to the first 2 mL (8 – 6 mL). (B) Representative image of the fourth fraction from the top (2 – 1 mL). (C) Representative image of the fifth fraction from the top (1 – 0.5 mL). (D) Representative image of the bottom fraction, corresponding to the last 500 μ L (0.5 – 0 mL) fraction. Fluorescence is from Rhod-DOPE (1:500 mol:mol labeled to unlabeled lipid ratio). (E) Bar plot showing the average normalized fluorescence intensity \pm standard deviation for each collected fractions. Intensities were obtained from at least three representative images of each fraction and normalized to the maximum fluorescence intensity observed.

3.3.3. *Formation of supported lipid bilayers from GUVs onto avidin-coated glass Ibidi glass bottom slides by osmotic shock*

We performed four electroformations of GUVs containing POPC and DOPE-cap-biotin (1:1000 mol:mol), two of them with Rhod-DOPE (1:500 mol:mol) and the other two with NBD-DPPE (1:200 mol:mol) as a membrane fluorescent label. The solutions of GUVs were all mixed with each other, and GUVs were concentrated by the methodology described in the previous experience (the last 500 μL fraction was collected after overnight rest). 200 μL of this fraction plus 100 μL of glucose were added to an Ibidi glass bottom slide previously coated with BSA-biotin and avidin.

Imaging results under the confocal microscope showed GUVs independently labeled with Rhod-DOPE or NBD-DPPE immobilized and spread on the surface, as is evident by fluorescence observed inside of the vesicles in the xy plane (Figure 3.18 - A) and by the xz plane results (not shown). After 1 hour rest, we tried to induce an osmotic shock onto these vesicles; since the interior of the vesicles contains 200 mM sucrose, a lower osmolarity outside these vesicles could induce rupture. We carefully removed 200 μL of solution from the chamber, added the same amount of glucose/sucrose free water and immediately observed the results under the microscope, observing that most of the GUVs had collapsed, forming SLBs (Figure 3.18 - B). In some cases, we observed double supported bilayers formed from the collapse of a GUV onto a previously formed SLB; these structures had, naturally, a higher fluorescence than single SLBs and could be readily identified under the microscope (Figure 3.18 - B). Nevertheless, osmotic shock proved to be an effective strategy to collapse adhered GUVs and form supported lipid bilayers. In fact, we observed the existence of supported bilayers containing both NBD-DPPE and Rhod-DOPE signals (Figure 3.18 - C, D, E); since GUVs were formed with either fluorescent label separately, this could be attributed to membrane fusion from GUVs labeled with Rhod-DOPE and NBD-DPPE after rupture (no GUVs were detected with both labels prior to osmotic shock). This is important, since it means that larger membranes can be formed by fusion of two or more smaller membranes; if this didn't happen, a larger, uniform SLB could not possibly be formed from a mixture of GUVs and only SLBs from isolated GUVs would be available for our studies. To verify lipid probe mobility in the supported lipid bilayers, we chose a membrane labeled with only NBD-DPPE or Rhod-DOPE and performed FRAP studies. We obtained a diffusion coefficient of $1.50 \pm 0.24 \mu\text{m}^2/\text{s}$ for NBD-DPPE and $2.10 \pm 0.22 \mu\text{m}^2/\text{s}$ for Rhod-DOPE, both in agreement with literature (130). For both probes, we obtained a mobile fraction of 100%, showing a properly-formed membrane onto avidin-coated glass surface (Figure 3.18 - F, G). The next studies focused on forming SLBs from GUVs on glass coverslips and avidin micropatterning by the same methodology than in Ibidi glass bottom slides.

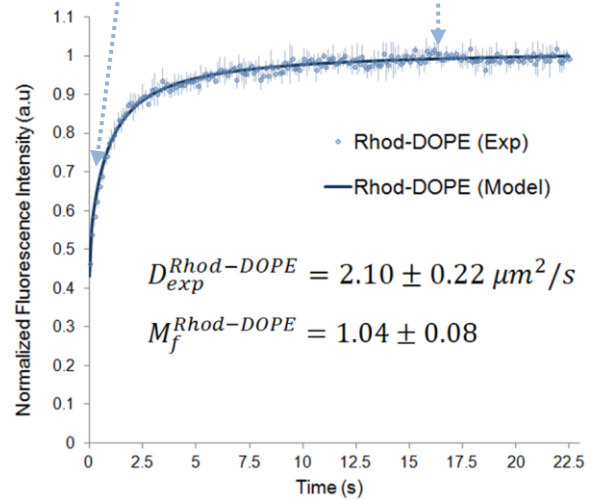
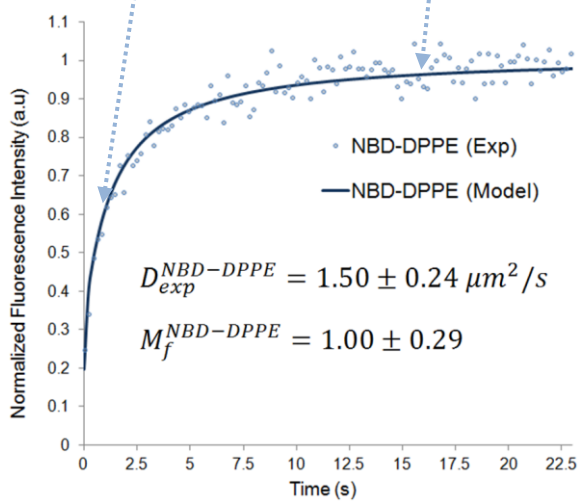
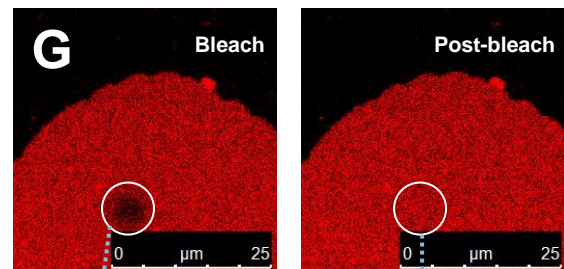
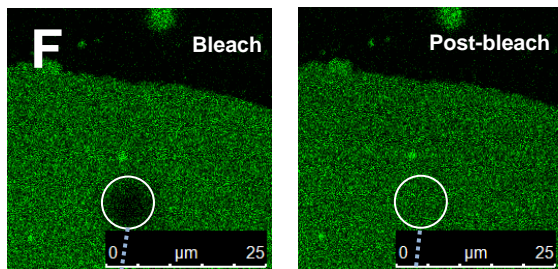
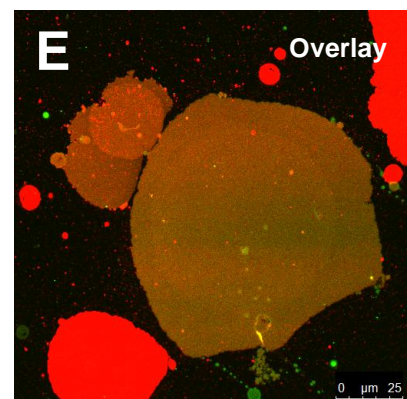
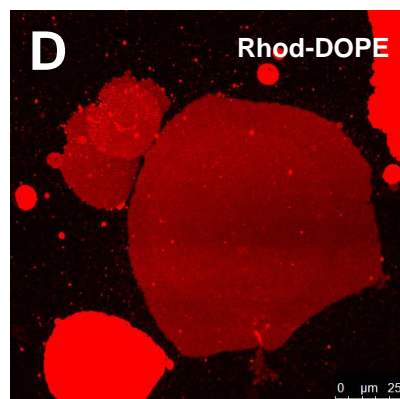
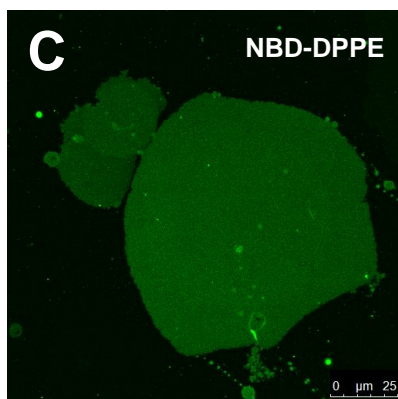
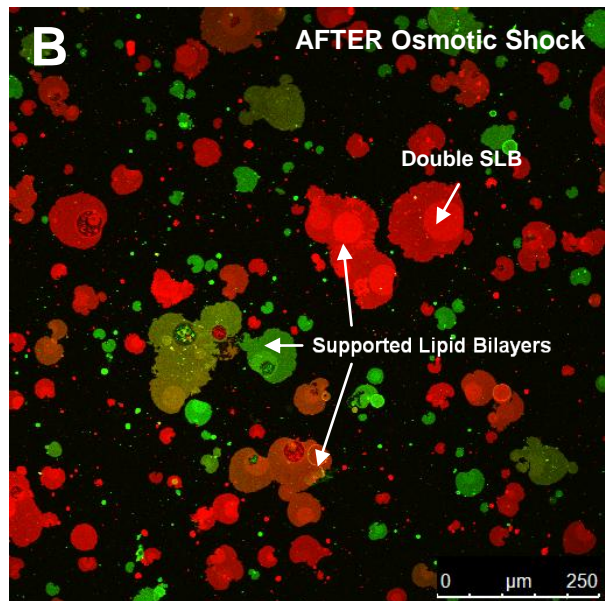
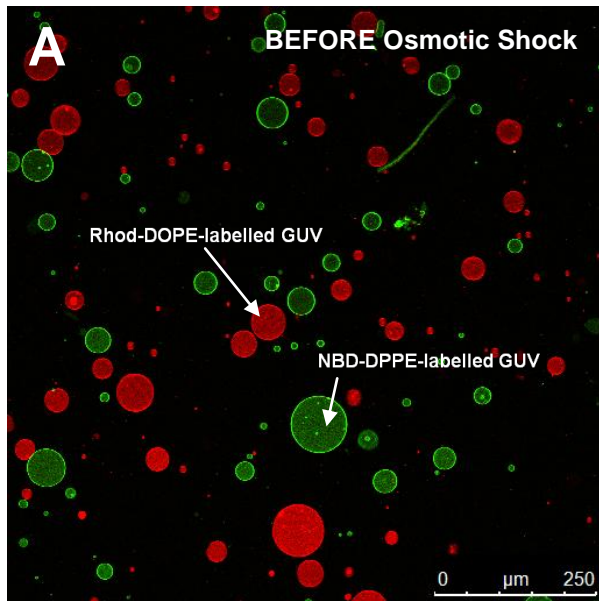


Figure 3.18 – Formation of supported lipid bilayers from POPC GUVs onto BSA-biotin/avidin-coated Ibidi glass bottom slides by osmotic shock induction. (A) GUVs labeled with Rhod-DOPE (red) or NBD-DPPE (green) before osmotic shock; most GUVs were immobilized in the surface. (B) GUVs labeled with Rhod-DOPE (red) or NBD-DPPE (green) after osmotic shock. SLBs were formed from vesicles after collapse had been induced by osmotic shock. (C) NBD-DPPE channel showing SLBs formed from GUVs after osmotic shock. (D) Rhod-DOPE channel showing supported lipid bilayer formed from GUVs after osmotic shock. (E) Overlay between NBD-DPPE and Rhod-DOPE channels. (F), (G) FRAP experiments on SLB formed by GUV labeled with NBD-DPPE or Rhod-DOPE, showing a representative image of both bleach and post-bleach phase. FRAP curves (normalized fluorescence intensity over time) below show diffusion coefficients D and fluorophore mobile fractions M_f . NBD-DPPE and Rhod-DOPE were used at 1:200 mol:mol and 1:500 mol:mol labeled to unlabeled lipid ratio. Unlabeled BSA-biotin and avidin were added at 1 mg/mL concentration.

3.3.4. *Formation of supported lipid bilayers from GUVs onto non-micropatterned and micropatterned avidin-coated glass coverslips*

Using the same lipid mixtures as in the previous experience, together with the same method for GUV concentration, we performed studies onto glass coverslips (i) blocked by BSA-biotin and avidin (control); (ii) containing an avidin micropatterning fabricated by standard procedure.

Results from the control show that, even before inducing GUV burst by osmotic shock, a great number of them had already collapsed forming supported lipid bilayers; after applying osmotic shock, practically all of them had collapsed (Figure 3.19 - A, B). We observed that most of the surface was covered with SLBs; although not forming a completely homogeneous membrane, this surface density of SLBs was satisfactory for the purpose of our work if the equivalent happened onto an avidin micropatterning. When this mixture was added to an avidin micropatterned glass coverslip, a huge number of GUVs was observable even before osmotic shock; however, after inducing the osmotic shock, no SLBs were apparently detected and GUV size seemed to decrease (Figure 3.19 - C, D; the plane of the micropatterning is below the plane of the GUVs and is not shown here). Additionally, most of the GUVs were not immobilized, contrarily to what happened in normal avidin-coated surfaces, where they were readily immobilized. After another cycle to induce osmotic shock, a small number of supported lipid bilayers were formed - however, the density of SLBs was not only small, but it didn't appear that GUVs were immobilizing on the micropatterning or had any special affinity towards the surface (Figure 3.19 - E, F). For the SLBs formed in these studies, we obtained a diffusion coefficient of $1.80 \pm 0.44 \mu\text{m}^2/\text{s}$, which is in agreement with the previous results for Rhod-DOPE and with literature (130); the mobile fraction was 100%, suggesting a defect-free supported lipid bilayer onto patterned surface (results not shown).

Thus, the behavior of GUVs onto the avidin micropatterning, when comparing with the control, seems to suggest that these vesicles are not binding surface avidin after micropatterning fabrication. Finally, the decreasing size of non-immobilized GUVs after osmotic shock could be explained by minimization of osmotic stress by fission. The last studies tried to elucidate why GUVs were unable adhere to avidin micropatterned surfaces.

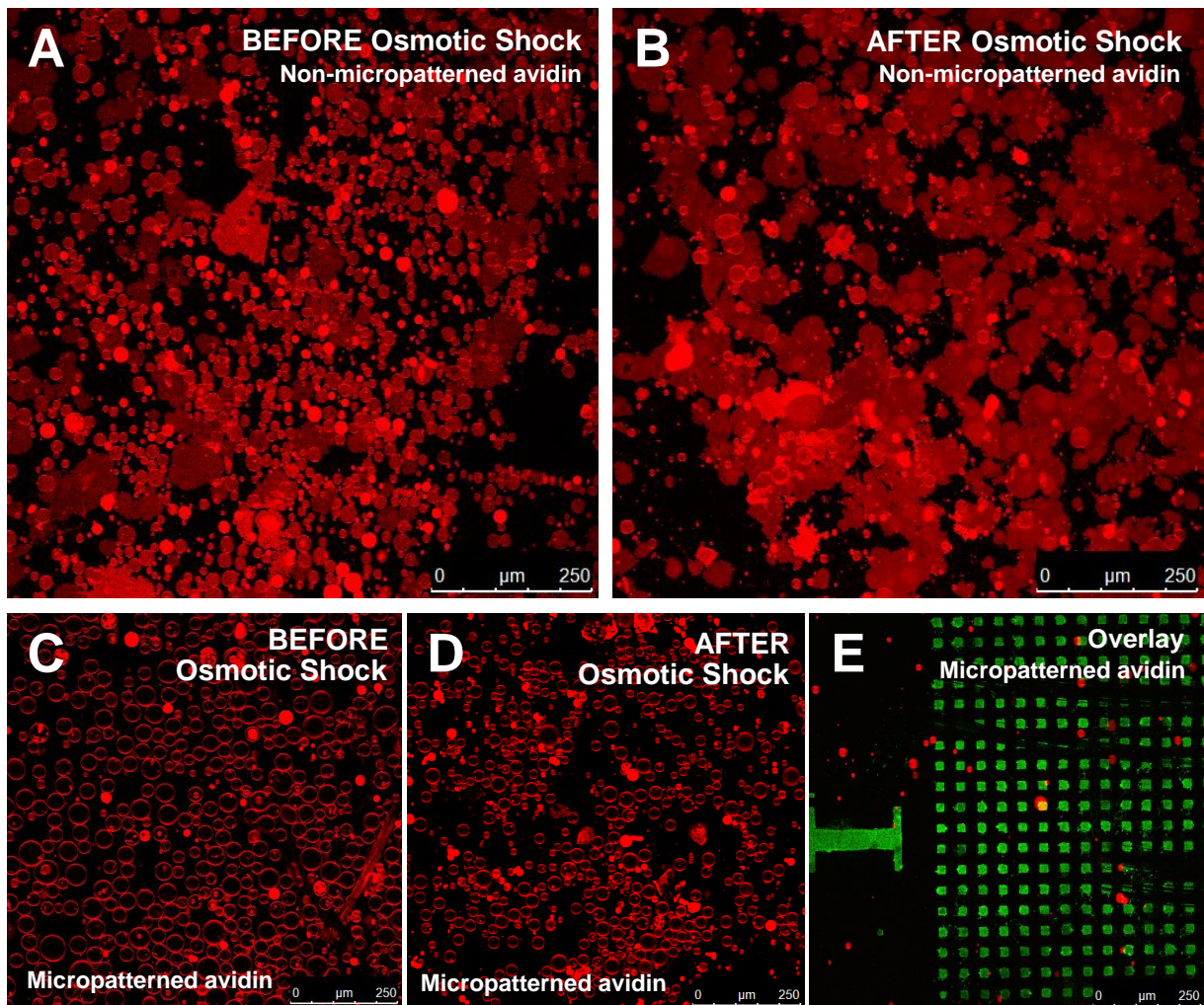


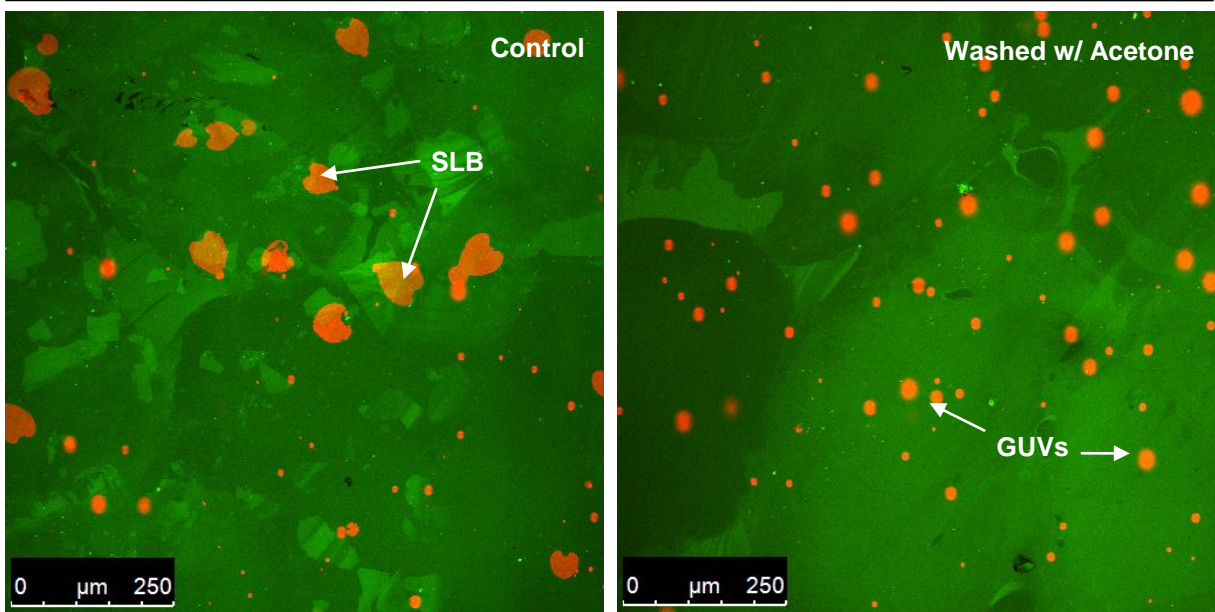
Figure 3.19 – Formation of supported lipid bilayers from POPC GUVs onto micropatterned and non-micropatterned avidin-coated glass coverslips. (A), (B) GUVs onto glass coverslips coated with BSA-biotin and avidin before and after osmotic shock, respectively. (C), (D) GUVs onto glass coverslips micropatterned with avidin before and after osmotic shock, respectively. The xy plane shown is above the surface and the micropatterning is not visible (E), (F) Overlay channels (Rhod-DOPE at red + avidin-Alexa350 at green), showing GUVs onto avidin micropatterning, after osmotic shock; an SLB formed from GUV collapse is shown in (E). Fluorescence is from avidin-Alexa488 and Rhod-DOPE, which were used at 1:25 mol:mol and 1:500 mol:mol labeled to unlabeled protein and lipid ratio, respectively. Avidin pattern was fabricated according to section 3.1.4., Figure 3.17. BSA-biotin and avidin were added at 1 mg/mL concentration.

3.3.5. Effect of acetone washing on GUV immobilization onto BSA-biotin and avidin-coated glass substrate

We thus tried to evaluate the direct effect of acetone on GUV immobilization and inability of biotinylated lipid for binding biotin, without using avidin micropatterning. For this, we performed four electroformations of GUVs containing POPC and DOPE-cap-biotin (1:1000 mol:mol) with Rhod-DOPE (1:500 mol:mol) as membrane label; we did not use the GUV concentration procedure described in 3.3.2., since we did not require high quantities of vesicles for the purpose of this experiment. Ibbidi glass bottom slides coated with BSA-biotin and avidin were either briefly washed with acetone and water or only with water. We added 50 μ L of the mixed GUV electroformations to 200 μ L of glucose solution to the slides and waited one hour to let the vesicles deposit in the bottom surface.

The results show that, as expected, GUVs immobilized and collapsed to form SLBs onto the control sample even before osmotic shock, similarly to what had happened in section 3.3.4 (Figure 3.20 – A). On the contrary, the sample washed with acetone after protein incubation was not able to immobilize and form SLBs; the red spots that can be seen on the surface belong to the lower part of the vesicles close to the surface (Figure 3.20 – B). After osmotic shock induction, practically all the vesicles had burst to form SLBs on the surface of the control, while nothing happened on the sample washed with acetone (Figure 3.20 – C, D). These results suggest that acetone is responsible for the inability of avidin to bind biotinylated lipids on GUVs, shedding light on why these vesicles were unable to bind to the avidin micropatterned surface; partial denaturation of avidin during the acetone washing step is a strong possibility. However, these results do not explain why biotin-fluorescein conjugate was able to efficiently bind the micropatterned surface and retain this ability even after acetone washing (section 3.1.5). One could try to explain these results suggesting that biotin-fluorescein can bind surface avidin much easier than biotin when inserted in a GUV – the former is a small molecule that can easily diffuse through aqueous solution, while the latter is inserted in a large membrane, having a much lower diffusion rate and more difficult access for binding.

BEFORE Osmotic Shock



AFTER Osmotic Shock

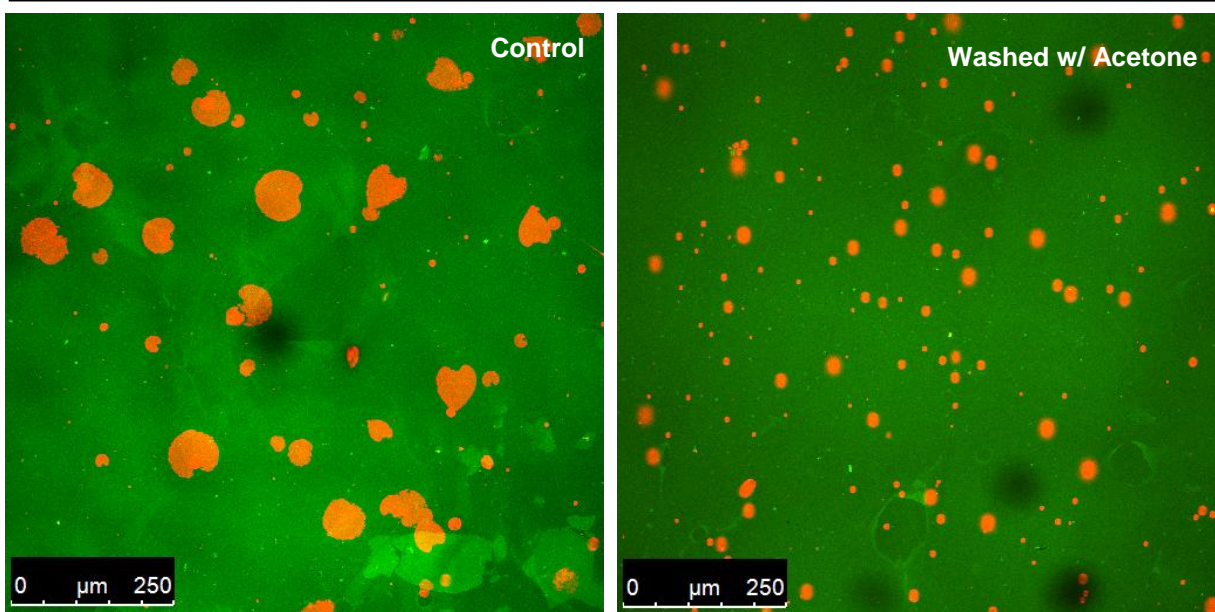


Figure 3.20 – Effect of acetone washing in the formation of supported lipid bilayers from POPC GUVs in Ibidi glass slides. (A), (B) GUVs (red) in a BSA-biotin and avidin-coated glass (green) not exposed and exposed to acetone, respectively. SLBs were observed even before osmotic shock induction; the lower part of the GUVs (lower hemisphere) is pointed out in the picture. (C), (D) GUVs (red) in a BSA-biotin and avidin-coated glass (green) not exposed and exposed to acetone, respectively, after osmotic shock induction in order to form SLBs. While most GUVs collapsed on the control (not exposed to acetone), in the sample washed with acetone practically no SLBs were detected. Avidin-Alexa488 and Rhod-DOPE were used at 1:25 mol:mol and 1:500 mol:mol labeled to unlabeled protein and lipid ratio, respectively. BSA-biotin and avidin were added at 0.1 mg/mL concentration.

3.4. FINAL REMARKS AND FUTURE PERSPECTIVES

The micropatterned system chosen by us in this study relied on the use of BSA-biotin, which offers great protein adhesion, resistance to organic solvent exposure and is required for photoresist removal in the final step of the microfabrication process. The presence of biotin allows for avidin binding which generates sites of protein surface-lipid membrane adhesions.

The formation of supported lipid bilayers onto a protein micropatterned surface fabricated by standard photolithography is a challenging task. On one hand, SUVs are the most appropriate systems for studies attempting to form supported lipid bilayers on clean glass, but fail to form defective-free and homogeneous SLBs onto protein-coated surfaces, even in the presence of PEG or high temperatures. In fact SUVs are shown here to be highly stable when immobilized in a BSA-biotin/avidin-coated surface. It is possible that this property is useful for applications demanding presentation of liposomes in surfaces.

On the other hand, GUVs are far more unstable when immobilized than SUVs, even in protein-coated surfaces as demonstrated here. Making use of this circumstance, we employed GUVs as tools for the generation of SLBs. The attempt to form supported lipid bilayers from GUVs onto BSA-biotin and avidin coated surfaces was successful, since after osmotic shock induction practically all immobilized GUVs were able to form homogeneous SLBs, and even fuse with each other to create larger membranes; in principle, the size of membranes so created would be enough for us to study the effect of avidin adhesions on membranes with a composition that enabled phase coexistence to occur. However, these GUVs proved unable to adhere to the avidin micropatterned surface, an effect that we ultimately attributed to the acetone washing step. This effect was not expected for two main reasons: first, biotin fluorescein experiments showed that acetone washing had no effect on the ability of avidin to bind biotin in solution; second, we observed that SUVs containing biotinylated lipid still bound micropatterned avidin, suggesting that this protein was not affected after acetone washing. It might be that, after acetone washing, proteins in the surface are modified such that only small molecules such as biotin, or small vesicles such as SUVs, are able to efficiently bind avidin, while bigger-sized vesicles, such as GUVs, are incapable of doing so.

In this way, although avidin has been reported to resist organic solvents, it is clear that, in order to achieve supported membrane formation with GUVs on micropatterned surfaces, avidin must not be exposed to this type of treatment. A possible alternative is to perform incubation of BSA-biotin-patterned surfaces with avidin only after acetone treatment, making sure that non-specific adsorption of avidin to the exposed coverslip surface is kept at a minimum.

Alternative methods that rely on photomasks include the use of photosensitizers that graft desired proteins on PEG surfaces or the use of deep-UV that selectively destroys binding molecules through oxidation (134, 135). At the same time, efforts have been made to use bio-friendly photoresists to construct protein micropatterned surfaces (136, 137). However, most lithographic procedures still have the problem of low biocompatibility.

One of the most widely used techniques for biological applications that require protein micropatterning is soft lithography, namely microcontact printing using a PDMS stamp (102). Although

this technique also makes use of photolithography to create the stamps with the micro or nanostructures intended, this procedure is only needed once, since the mold can be used repeatedly, and is much more biocompatible than standard photolithography (102, 134). The use of a PDMS stamp to create the avidin micropatterning, followed by addition and immobilization of GUVs is a potential strategy in the upcoming experiments.

Finally, after obtaining a working avidin patterned surface for studies on the impact of membrane adhesion on lipid phase separation, biotinylated GPMVs would be prepared by incubation of GPMVs obtained from cell culture of animal cells and BSA-biotinylated lipid complexes or mixtures of biotinylated lipids and lysophospholipids. These vesicles could then be used to generate supported membranes obtained from living cells, and the impact of membrane adhesions could be directly studied on them.

Altogether, it is evident that merging a delicate field of study such as biophysics with microtechnologies proves challenging, since these fields were born from radically different backgrounds and are, in the broadest, concerned with different goals. Additionally, the plasma membrane of living cells is so complex that it is almost imperative to study its principles and dynamics at a more simple level – however, we can only do this to a certain extent, otherwise we risk ourselves to favor simplicity over biological relevance. The cytoskeleton, as already stated, is likely to be an extremely important component in mediating the formation of plasma membrane heterogeneities (such as membrane rafts), and there is a great need to include adhesions to the lipid membrane *in vitro* and observe what the effects are in relevant lipid mixtures able to display phase coexistence. This work represented an additional step in generating a more complete model system for the study of the modulation of plasma membrane heterogeneities and to the understanding of plasma membrane raft dynamics. The completion of the work is a worthy and important goal to pursue, and it is the source of much motivation for future studies.

4.REFERENCES

1. Gorter, E., and F. Grendel. 1925. On Bimolecular Layers of Lipoids on the Chromocytes of the Blood. *J. Exp. Med.* 41: 439–443.
2. Singer, S.J., and G.L. Nicolson. 1972. The fluid mosaic model of the structure of cell membranes. *Science.* 175: 720–31.
3. Simons, K., and J.L. Sampaio. 2011. Membrane organization and lipid rafts. *Cold Spring Harb. Perspect. Biol.* 3.
4. Van Meer, G., and A.I.P.M. de Kroon. 2011. Lipid map of the mammalian cell. *J. Cell Sci.* 124: 5–8.
5. Futerman, A.H., and Y.A. Hannun. 2004. The complex life of simple sphingolipids. *EMBO Rep.* 5: 777–782.
6. Kihara, A., and Y. Igarashi. 2004. Cross talk between sphingolipids and glycerophospholipids in the establishment of plasma membrane asymmetry. *Mol. Biol. Cell.* 15: 4949–4959.
7. Shevchenko, A., and K. Simons. 2010. Lipidomics: coming to grips with lipid diversity. *Nat. Rev. Mol. Cell Biol.* 11: 593–598.
8. Pike, L.J. 2009. The challenge of lipid rafts. *J. Lipid Res.* 50 Suppl: S323–8.
9. Bagatolli, L.A., J.H. Ipsen, A.C. Simonsen, and O.G. Mouritsen. 2010. An outlook on organization of lipids in membranes: searching for a realistic connection with the organization of biological membranes. *Prog. Lipid Res.* 49: 378–89.
10. Domanska, M.K., D. Wrona, and P.M. Kasson. 2013. Multiphasic effects of cholesterol on influenza fusion kinetics reflect multiple mechanistic roles. *Biophys. J.* 105: 1383–7.
11. Head, B.P., H.H. Patel, and P. a Insel. 2014. Interaction of membrane/lipid rafts with the cytoskeleton: impact on signaling and function: membrane/lipid rafts, mediators of cytoskeletal arrangement and cell signaling. *Biochim. Biophys. Acta.* 1838: 532–45.
12. Hjort Ipsen, J., G. Karlström, O.G. Mouritsen, H. Wennerström, and M.J. Zuckermann. 1987. Phase equilibria in the phosphatidylcholine-cholesterol system. *Biochim. Biophys. Acta.* 905: 162–172.
13. Simons, K., and E. Ikonen. 1997. Functional rafts in cell membranes. *Nature.* 387: 569–72.
14. García-Sáez, A.J., and P. Schuille. 2010. Stability of lipid domains. *FEBS Lett.* 584: 1653–8.
15. Van Meer, G., and K. Simons. 1988. Lipid polarity and sorting in epithelial cells. *J. Cell. Biochem.* 36: 51–8.
16. Schroeder, R., E. London, and D. Brown. 1994. Interactions between saturated acyl chains confer detergent resistance on lipids and glycosylphosphatidylinositol (GPI)-anchored proteins: GPI-anchored proteins in liposomes and cells show similar behavior. *Proc. Natl. Acad. Sci. U. S. A.* 91: 12130–4.
17. Brown, D.A. 2006. Lipid rafts, detergent-resistant membranes, and raft targeting signals. *Physiology.* 21: 430–9.
18. Lingwood, D., and K. Simons. 2010. Lipid rafts as a membrane-organizing principle. *Science.* 327: 46–50.

19. Pike, L.J. 2006. Rafts defined: a report on the Keystone symposium on lipid rafts and cell function. *J. Lipid Res.* 47: 1597–8.
20. Jacobson, K., O.G. Mouritsen, and R.G.W. Anderson. 2007. Lipid rafts: at a crossroad between cell biology and physics. *Nat. Cell Biol.* 9: 7–14.
21. Meiri, K.F. 2005. Lipid rafts and regulation of the cytoskeleton during T cell activation. *Philos. Trans. R. Soc. B.* 360: 1663–72.
22. Heberle, F.A., and G.W. Feigenson. 2011. Phase separation in lipid membranes. *Cold Spring Harb. Perspect. Biol.* 3.
23. Feigenson, G.W. 2007. Phase boundaries and biological membranes. *Annu. Rev. Biophys. Biomol. Struct.* 36: 63–77.
24. De Almeida, R.F.M., A. Fedorov, and M. Prieto. 2003. Sphingomyelin/phosphatidylcholine/cholesterol phase diagram: boundaries and composition of lipid rafts. *Biophys. J.* 85: 2406–16.
25. Feigenson, G.W. 2009. Phase diagrams and lipid domains in multicomponent lipid bilayer mixtures. *Biochim. Biophys. Acta.* 1788: 47–52.
26. Gómez-Llobregat, J., J. Buceta, and R. Reigada. 2013. Interplay of cytoskeletal activity and lipid phase stability in dynamic protein recruitment and clustering. *Sci. Rep.* 3: 2608.
27. Korlach, J., P. Schwille, W.W. Webb, and G.W. Feigenson. 1999. Characterization of lipid bilayer phases by confocal microscopy and fluorescence correlation spectroscopy. *Proc. Natl. Acad. Sci. U. S. A.* 96: 8461–6.
28. Hammond, A.T., F.A. Heberle, T. Baumgart, D. Holowka, B. Baird, et al. 2005. Crosslinking a lipid raft component triggers liquid ordered-liquid disordered phase separation in model plasma membranes. *Proc. Natl. Acad. Sci. U. S. A.* 102: 6320–5.
29. Lingwood, D., J. Ries, P. Schwille, and K. Simons. 2008. Plasma membranes are poised for activation of raft phase coalescence at physiological temperature. *Proc. Natl. Acad. Sci. U. S. A.* 105: 10005–10.
30. Kaiser, H.-J., D. Lingwood, I. Levental, J.L. Sampaio, L. Kalvodova, et al. 2009. Order of lipid phases in model and plasma membranes. *Proc. Natl. Acad. Sci. U. S. A.* 106: 16645–50.
31. Baumgart, T., A.T. Hammond, P. Sengupta, S.T. Hess, D. a Holowka, et al. 2007. Large-scale fluid/fluid phase separation of proteins and lipids in giant plasma membrane vesicles. *Proc. Natl. Acad. Sci. U. S. A.* 104: 3165–70.
32. Veatch, S.L., P. Cicuta, P. Sengupta, A. Honerkamp-Smith, D. Holowka, et al. 2008. Critical fluctuations in plasma membrane vesicles. *ACS Chem. Biol.* 3: 287–93.
33. Veatch, S.L., O. Soubias, S.L. Keller, and K. Gawrisch. 2007. Critical fluctuations in domain-forming lipid mixtures. *Proc. Natl. Acad. Sci. U. S. A.* 104: 17650–5.
34. Connell, S.D., G. Heath, P.D. Olmsted, and A. Kisil. 2013. Critical point fluctuations in supported lipid membranes. *Faraday Discuss.* 161: 91.
35. Elson, E.L., E. Fried, J.E. Dolbow, and G.M. Genin. 2010. Phase separation in biological membranes: integration of theory and experiment. *Annu. Rev. Biophys.* 39: 207–26.

36. Honerkamp-Smith, A.R., S.L. Veatch, and S.L. Keller. 2009. An introduction to critical points for biophysicists; observations of compositional heterogeneity in lipid membranes. *Biochim. Biophys. Acta.* 1788: 53–63.
37. Zhao, J., J. Wu, and S.L. Veatch. 2013. Adhesion stabilizes robust lipid heterogeneity in supercritical membranes at physiological temperature. *Biophys. J.* 104: 825–34.
38. Luna, E.J., and A.L. Hitt. 1992. Cytoskeleton--plasma membrane interactions. *Science.* 258: 955–64.
39. Pinder, J.C., S.E. Clark, A.J. Baines, E. Morris, and W.B. Gratzer. 1981. The construction of the red cell cytoskeleton. *Prog. Clin. Biol. Res.* 55: 343–61.
40. Doherty, G.J., and H.T. McMahon. 2008. Mediation, modulation, and consequences of membrane-cytoskeleton interactions. *Annu. Rev. Biophys.* 37: 65–95.
41. Kapus, A., and P. Janmey. 2013. Plasma membrane--cortical cytoskeleton interactions: a cell biology approach with biophysical considerations. *Compr. Physiol.* 3: 1231–81.
42. Eddin, M. 2006. Switching sides: the actin/membrane lipid connection. *Biophys. J.* 91: 3963.
43. Garg, S., J.X. Tang, J. R uhe, and C.A. Naumann. 2009. Actin-induced perturbation of PS lipid-cholesterol interaction: A possible mechanism of cytoskeleton-based regulation of membrane organization. *J. Struct. Biol.* 168: 11–20.
44. Lenne, P.-F., L. Wawrezinieck, F. Conchonaud, O. Wurtz, A. Boded, et al. 2006. Dynamic molecular confinement in the plasma membrane by microdomains and the cytoskeleton meshwork. *EMBO J.* 25: 3245–56.
45. Goswami, D., K. Gowrishankar, S. Bilgrami, S. Ghosh, R. Raghupathy, et al. 2008. Nanoclusters of GPI-anchored proteins are formed by cortical actin-driven activity. *Cell.* 135: 1085–97.
46. Heinemann, F., S.K. Vogel, and P. Schwille. 2013. Lateral membrane diffusion modulated by a minimal actin cortex. *Biophys. J.* 104: 1465–75.
47. Golebiewska, U., J.G. Kay, T. Masters, S. Grinstein, W. Im, et al. 2011. Evidence for a fence that impedes the diffusion of phosphatidylinositol 4,5-bisphosphate out of the forming phagosomes of macrophages. *Mol. Biol. Cell.* 22: 3498–507.
48. Kusumi, A., T.K. Fujiwara, R. Chadda, M. Xie, T.A. Tsunoyama, et al. 2012. Dynamic organizing principles of the plasma membrane that regulate signal transduction: commemorating the fortieth anniversary of Singer and Nicolson's fluid-mosaic model. *Annu. Rev. Cell Dev. Biol.* 28: 215–50.
49. Machta, B.B., S. Papanikolaou, J.P. Sethna, and S.L. Veatch. 2011. Minimal model of plasma membrane heterogeneity requires coupling cortical actin to criticality. *Biophys. J.* 100: 1668–77.
50. Sako, Y., A. Nagafuchi, S. Tsukita, M. Takeichi, and A. Kusumi. 1998. Cytoplasmic regulation of the movement of E-cadherin on the free cell surface as studied by optical tweezers and single particle tracking: corralling and tethering by the membrane skeleton. *J. Cell Biol.* 140: 1227–40.
51. Fujiwara, T., K. Ritchie, H. Murakoshi, K. Jacobson, and A. Kusumi. 2002. Phospholipids undergo hop diffusion in compartmentalized cell membrane. *J. Cell Biol.* 157: 1071–81.

52. Ritchie, K., R. Iino, T. Fujiwara, K. Murase, and A. Kusumi. 2003. The fence and picket structure of the plasma membrane of live cells as revealed by single molecule techniques (Review). *Mol. Membr. Biol.* 20: 13–18.
53. Andrews, N.L., K.A. Lidke, J.R. Pfeiffer, A.R. Burns, B.S. Wilson, et al. 2008. Actin restricts FcεRI diffusion and facilitates antigen-induced receptor immobilization. *Nat. Cell Biol.* 10: 955–63.
54. Ehrig, J., E.P. Petrov, and P. Schwille. 2011. Near-critical fluctuations and cytoskeleton-assisted phase separation lead to subdiffusion in cell membranes. *Biophys. J.* 100: 80–9.
55. Saarikangas, J., H. Zhao, and P. Lappalainen. 2010. Regulation of the actin cytoskeleton-plasma membrane interplay by phosphoinositides. *Physiol. Rev.* 90: 259–289.
56. Zhang, L., Y.S. Mao, P.A. Janmey, and H.L. Yin. 2012. Phosphatidylinositol 4, 5 bisphosphate and the actin cytoskeleton. *Subcell. Biochem.* 59: 177–215.
57. Ben-Aissa, K., G. Patino-Lopez, N. V. Belkina, O. Maniti, T. Rosales, et al. 2012. Activation of moesin, a protein that links actin cytoskeleton to the plasma membrane, occurs by phosphatidylinositol 4,5-bisphosphate (PIP₂) binding sequentially to two sites and releasing an autoinhibitory linker. *J. Biol. Chem.* 287: 16311–23.
58. Maniti, O., N. Khalifat, K. Goggia, F. Dalonneau, C. Guérin, et al. 2012. Binding of moesin and ezrin to membranes containing phosphatidylinositol (4,5) bisphosphate: a comparative study of the affinity constants and conformational changes. *Biochim. Biophys. Acta.* 1818: 2839–49.
59. Maniti, O., K. Carvalho, and C. Picart. 2013. Model membranes to shed light on the biochemical and physical properties of ezrin/radixin/moesin. *Biochimie.* 95: 3–11.
60. Fehon, R.G., A.I. McClatchey, and A. Bretscher. 2010. Organizing the cell cortex: the role of ERM proteins. *Nat. Rev. Mol. Cell Biol.* 11: 276–87.
61. Itoh, K., M. Sakakibara, S. Yamasaki, A. Takeuchi, H. Arase, et al. 2002. Cutting edge: negative regulation of immune synapse formation by anchoring lipid raft to cytoskeleton through Cbp-EBP50-ERM assembly. *J. Immunol.* 168: 541–4.
62. Johnson, C.M., and W. Rodgers. 2008. Spatial Segregation of Phosphatidylinositol 4,5-Bisphosphate (PIP₂) Signaling in Immune Cell Functions. *Immunol. Endocr. Metab. Agents Med. Chem.* 8: 349–357.
63. Gambhir, A., G. Hangyás-Mihályné, I. Zaitseva, D.S. Cafiso, J. Wang, et al. 2004. Electrostatic sequestration of PIP₂ on phospholipid membranes by basic/aromatic regions of proteins. *Biophys. J.* 86: 2188–207.
64. Heo, W. Do, T. Inoue, W.S. Park, M.L. Kim, B.O. Park, et al. 2006. PI(3,4,5)P₃ and PI(4,5)P₂ lipids target proteins with polybasic clusters to the plasma membrane. *Science.* 314: 1458–61.
65. Redfern, D.A., and A. Gericke. 2005. pH-dependent domain formation in phosphatidylinositol polyphosphate/phosphatidylcholine mixed vesicles. *J. Lipid Res.* 46: 504–15.
66. Fernandes, F., L.M.S. Loura, A. Fedorov, and M. Prieto. 2006. Absence of clustering of phosphatidylinositol-(4,5)-bisphosphate in fluid phosphatidylcholine. *J. Lipid Res.* 47: 1521–5.
67. Sheetz, M.P., J.E. Sable, and H.-G. Döbereiner. 2006. Continuous membrane-cytoskeleton adhesion requires continuous accommodation to lipid and cytoskeleton dynamics. *Annu. Rev. Biophys. Biomol. Struct.* 35: 417–34.

68. Hope, H.R., and L.J. Pike. 1996. Phosphoinositides and phosphoinositide-utilizing enzymes in detergent-insoluble lipid domains. *Mol. Biol. Cell.* 7: 843–51.
69. Rozelle, A.L., L.M. Machesky, M. Yamamoto, M.H. Driessens, R.H. Insall, et al. 2000. Phosphatidylinositol 4,5-bisphosphate induces actin-based movement of raft-enriched vesicles through WASP-Arp2/3. *Curr. Biol.* 10: 311–20.
70. Pike, L.J., and J.M. Miller. 1998. Cholesterol Depletion Delocalizes Phosphatidylinositol Bisphosphate and Inhibits Hormone-stimulated Phosphatidylinositol Turnover. *J. Biol. Chem.* 273: 22298–22304.
71. Johnson, C.M., G.R. Chichili, and W. Rodgers. 2008. Compartmentalization of phosphatidylinositol 4,5-bisphosphate signaling evidenced using targeted phosphatases. *J. Biol. Chem.* 283: 29920–8.
72. Levental, I., D.A. Christian, Y.-H. Wang, J.J. Madara, D.E. Discher, et al. 2009. Calcium-dependent lateral organization in phosphatidylinositol 4,5-bisphosphate (PIP₂)- and cholesterol-containing monolayers. *Biochemistry.* 48: 8241–8.
73. Levental, I., F.J. Byfield, P. Chowdhury, F. Gai, T. Baumgart, et al. 2009. Cholesterol-dependent phase separation in cell-derived giant plasma-membrane vesicles. *Biochem. J.* 424: 163–7.
74. Sarmiento, M.J., A. Coutinho, A. Fedorov, M. Prieto, and F. Fernandes. 2014. Ca²⁺ induces PI(4,5)P₂ clusters on lipid bilayers at physiological PI(4,5)P₂ and Ca²⁺ concentrations. *Biochim. Biophys. Acta.* 1838: 822–30.
75. Sezgin, E., and P. Schwille. 2012. Model membrane platforms to study protein-membrane interactions. *Mol. Membr. Biol.* 29: 144–54.
76. Vogel, S.K., and P. Schwille. 2012. Minimal systems to study membrane-cytoskeleton interactions. *Curr. Opin. Biotechnol.* 23: 758–65.
77. Wesolowska, O., K. Michalak, J. Maniewska, and A.B. Hendrich. 2009. Giant unilamellar vesicles - a perfect tool to visualize phase separation and lipid rafts in model systems. *Acta Biochim. Pol.* 56: 33–9.
78. Chan, Y.-H.M., and S.G. Boxer. 2007. Model membrane systems and their applications. *Curr. Opin. Chem. Biol.* 11: 581–7.
79. Liu, A.P., and D.A. Fletcher. 2006. Actin polymerization serves as a membrane domain switch in model lipid bilayers. *Biophys. J.* 91: 4064–70.
80. Sarmiento, M.J., M. Prieto, and F. Fernandes. 2012. Reorganization of lipid domain distribution in giant unilamellar vesicles upon immobilization with different membrane tethers. *Biochim. Biophys. Acta.* 1818: 2605–15.
81. El Kirat, K., S. Morandat, and Y.F. Dufrêne. 2010. Nanoscale analysis of supported lipid bilayers using atomic force microscopy. *Biochim. Biophys. Acta.* 1798: 750–65.
82. Castellana, E.T., and P.S. Cremer. 2006. Solid supported lipid bilayers: From biophysical studies to sensor design. *Surf. Sci. Rep.* 61: 429–444.
83. Richter, R.P., R. Bérat, and A.R. Brisson. 2006. Formation of solid-supported lipid bilayers: an integrated view. *Langmuir.* 22: 3497–505.

84. Yu, C.-H., and J.T. Groves. 2010. Engineering supported membranes for cell biology. *Med. Biol. Eng. Comput.* 48: 955–63.
85. Murray, D.H., L.K. Tamm, and V. Kiessling. 2009. Supported double membranes. *J. Struct. Biol.* 168: 183–9.
86. Mossman, K., and J. Groves. 2007. Micropatterned supported membranes as tools for quantitative studies of the immunological synapse. *Chem. Soc. Rev.* 36: 46–54.
87. Barfoot, R.J., K.H. Sheikh, B.R.G. Johnson, J. Colyer, R.E. Miles, et al. 2008. Minimal F-actin cytoskeletal system for planar supported phospholipid bilayers. *Langmuir.* 24: 6827–36.
88. Lee, K., J.L. Gallop, K. Rambani, and M.W. Kirschner. 2010. Self-assembly of filopodia-like structures on supported lipid bilayers. *Science.* 329: 1341–5.
89. Owens, F., and C. Poole. 2003. *Introduction to Nanotechnology.* New Jersey, USA: John Wiley & Sons.
90. M. S. Dresselhaus, Y.-M. Lin, O. Rabin, M. R. Black, Jing Kong, G.D. 2004. *Springer Handbook of Nanotechnology.* New York, USA: Springer Berlin Heidelberg.
91. Groves, J.T. 1997. Micropatterning Fluid Lipid Bilayers on Solid Supports. *Science.* 275: 651–653.
92. Goudar, V.S., S. Suran, and M.M. Varma. 2012. Photoresist functionalisation method for high-density protein microarrays using photolithography. *Micro Nano Lett.* 7: 549.
93. Vail, T.L., K.W. Cushing, J.C. Ingram, and I. St Omer. 2006. Micropatterned avidin arrays on silicon substrates via photolithography, self-assembly and bioconjugation. *Biotechnol. Appl. Biochem.* 43: 85–91.
94. Orth, R.N., J. Kameoka, W.R. Zipfel, B. Ilic, W.W. Webb, et al. 2003. Creating biological membranes on the micron scale: forming patterned lipid bilayers using a polymer lift-off technique. *Biophys. J.* 85: 3066–73.
95. Torres, A.J., L. Vasudevan, D. Holowka, and B.A. Baird. 2008. Focal adhesion proteins connect IgE receptors to the cytoskeleton as revealed by micropatterned ligand arrays. *Proc. Natl. Acad. Sci. U. S. A.* 105: 17238–44.
96. Nair, P.M., K. Salaita, R.S. Petit, and J.T. Groves. 2011. Using patterned supported lipid membranes to investigate the role of receptor organization in intercellular signaling. *Nat. Protoc.* 6: 523–39.
97. Salaita, K., P.M. Nair, R.S. Petit, R.M. Neve, D. Das, et al. 2010. Restriction of receptor movement alters cellular response: physical force sensing by EphA2. *Science.* 327: 1380–5.
98. Irvine, D.J., J. Doh, and B. Huang. 2007. Patterned surfaces as tools to study ligand recognition and synapse formation by T cells. *Curr. Opin. Immunol.* 19: 463–9.
99. Biswas, A., A. Saha, B. Jana, P. Kurkute, G. Mondal, et al. 2013. A biotin micropatterned surface generated by photodestruction serves as a novel platform for microtubule organisation and DNA hybridisation. *Chembiochem.* 14: 689–94.
100. Kam, L., and S.G. Boxer. 2001. Cell adhesion to protein-micropatterned-supported lipid bilayer membranes. *J. Biomed. Mater. Res.* 55: 487–95.

101. Kung, L.A., L. Kam, J.S. Hovis, and S.G. Boxer. 2000. Patterning hybrid surfaces of proteins and supported lipid bilayers. *Langmuir*. 16: 6773–6776.
102. Whitesides, G.M., E. Ostuni, S. Takayama, X. Jiang, and D.E. Ingber. 2001. Soft lithography in biology and biochemistry. *Annu. Rev. Biomed. Eng.* 3: 335–73.
103. Predki, P.F. 2004. Functional protein microarrays: ripe for discovery. *Curr. Opin. Chem. Biol.* 8: 8–13.
104. Lesaichere, M.L., M. Uttamchandani, G.Y.J. Chen, and S.Q. Yao. 2002. Developing site-specific immobilization strategies of peptides in a microarray. *Bioorg. Med. Chem. Lett.* 12: 2079–83.
105. Halliwell, C.M., and A.E. Cass. 2001. A factorial analysis of silanization conditions for the immobilization of oligonucleotides on glass surfaces. *Anal. Chem.* 73: 2476–83.
106. Han, J., R.B. Seale, P. Silcock, A.J. McQuillan, and P.J. Bremer. 2011. The physico-chemical characterization of casein-modified surfaces and their influence on the adhesion of spores from a *Geobacillus* species. *Biofouling*. 27: 459–66.
107. Zhang, Q., R. Huang, and L.-H. Guo. 2009. One-step and high-density protein immobilization on epoxysilane-modified silica nanoparticles. *Chinese Sci. Bull.* 54: 2620–2626.
108. McClare, C.W. 1971. An accurate and convenient organic phosphorus assay. *Anal. Biochem.* 39: 527–30.
109. Wiederschain, G.Y. 2011. The molecular probes handbook. A guide to fluorescent probes and labeling technologies. *Biochem.* 76: 1276–1276.
110. Richter, R.P., and A.R. Brisson. 2005. Following the formation of supported lipid bilayers on mica: a study combining AFM, QCM-D, and ellipsometry. *Biophys. J.* 88: 3422–33.
111. De Almeida, R.F.M., J. Borst, A. Fedorov, M. Prieto, and A.J.W.G. Visser. 2007. Complexity of lipid domains and rafts in giant unilamellar vesicles revealed by combining imaging and microscopic and macroscopic time-resolved fluorescence. *Biophys. J.* 93: 539–53.
112. Lopez, A., L. Dupou, A. Altibelli, J. Trotard, and J.F. Tocanne. 1988. Fluorescence recovery after photobleaching (FRAP) experiments under conditions of uniform disk illumination. Critical comparison of analytical solutions, and a new mathematical method for calculation of diffusion coefficient D . *Biophys. J.* 53: 963–70.
113. Soumpasis, D.M. 1983. Theoretical analysis of fluorescence photobleaching recovery experiments. *Biophys. J.* 41: 95–7.
114. Axelrod, D., D.E. Koppel, J. Schlessinger, E. Elson, and W.W. Webb. 1976. Mobility measurement by analysis of fluorescence photobleaching recovery kinetics. *Biophys. J.* 16: 1055–69.
115. Ishikawa-Ankerhold, H.C., R. Ankerhold, and G.P.C. Drummen. 2012. Advanced fluorescence microscopy techniques--FRAP, FLIP, FLAP, FRET and FLIM. *Molecules.* 17: 4047–132.
116. Braeckmans, K., L. Peeters, N.N. Sanders, S.C. De Smedt, and J. Demeester. 2003. Three-dimensional fluorescence recovery after photobleaching with the confocal scanning laser microscope. *Biophys. J.* 85: 2240–52.
117. Wolf, D.E. 1992. Theory of fluorescence recovery after photobleaching measurements on cylindrical surfaces. *Biophys. J.* 61: 487–93.

118. Koppel, D.E., D. Axelrod, J. Schlessinger, E.L. Elson, and W.W. Webb. 1976. Dynamics of fluorescence marker concentration as a probe of mobility. *Biophys. J.* 16: 1315–29.
119. Koppel, D.E. 1979. Fluorescence redistribution after photobleaching. A new multipoint analysis of membrane translational dynamics. *Biophys. J.* 28: 281–91.
120. Waharte, F., K. Steenkeste, R. Briandet, and M.-P. Fontaine-Aupart. 2010. Diffusion measurements inside biofilms by image-based fluorescence recovery after photobleaching (FRAP) analysis with a commercial confocal laser scanning microscope. *Appl. Environ. Microbiol.* 76: 5860–9.
121. Halavatyj, A.A., P. V. Nazarov, S. Medves, M. van Troys, C. Ampe, et al. 2009. An integrative simulation model linking major biochemical reactions of actin-polymerization to structural properties of actin filaments. *Biophys. Chem.* 140: 24–34.
122. Phair, R.D., S.A. Gorski, and T. Misteli. 2004. Measurement of dynamic protein binding to chromatin in vivo, using photobleaching microscopy. *Methods Enzymol.* 375: 393–414.
123. Piran, U., and W.J. Riordan. 1990. Dissociation rate constant of the biotin-streptavidin complex. *J. Immunol. Methods.* 133: 141–3.
124. Green, N.M. 1963. The use of [¹⁴C]biotin for kinetic studies and for assay. *Biochem. J.* 89: 585–91.
125. Holmberg, A., A. Blomstergren, O. Nord, M. Lukacs, J. Lundeberg, et al. 2005. The biotin-streptavidin interaction can be reversibly broken using water at elevated temperatures. *Electrophoresis.* 26: 501–10.
126. Baumgart, T., G. Hunt, E.R. Farkas, W.W. Webb, and G.W. Feigenson. 2007. Fluorescence probe partitioning between Lo/Ld phases in lipid membranes. *Biochim. Biophys. Acta.* 1768: 2182–94.
127. Dietrich, C., L.A. Bagatolli, Z.N. Volovyk, N.L. Thompson, M. Levi, et al. 2001. Lipid rafts reconstituted in model membranes. *Biophys. J.* 80: 1417–28.
128. Sampaio, J.L., M.J. Moreno, and W.L.C. Vaz. 2005. Kinetics and thermodynamics of association of a fluorescent lysophospholipid derivative with lipid bilayers in liquid-ordered and liquid-disordered phases. *Biophys. J.* 88: 4064–71.
129. Spector, A.A., K. John, and J.E. Fletcher. 1969. Binding of long-chain fatty acids to bovine serum albumin. *J. Lipid Res.* 10: 56–67.
130. Guo, L., J.Y. Har, J. Sankaran, Y. Hong, B. Kannan, et al. 2008. Molecular diffusion measurement in lipid bilayers over wide concentration ranges: a comparative study. *Chemphyschem.* 9: 721–8.
131. Hair, M.L., and W. Hertl. 1970. Acidity of surface hydroxyl groups. *J. Phys. Chem.* 74: 91–94.
132. Cremer, P.S., and S.G. Boxer. 1999. Formation and Spreading of Lipid Bilayers on Planar Glass Supports. *J. Phys. Chem. B.* 103: 2554–2559.
133. Berquand, A., P.-E. Mazeran, J. Pantigny, V. Proux-Delrouyre, J.-M. Laval, et al. 2003. Two-Step Formation of Streptavidin-Supported Lipid Bilayers by PEG-Trigged Vesicle Fusion. Fluorescence and Atomic Force Microscopy Characterization. *Langmuir.* 19: 1700–1707.
134. Théry, M. 2010. Micropatterning as a tool to decipher cell morphogenesis and functions. *J. Cell Sci.* 123: 4201–13.

135. Azioune, A., N. Carpi, Q. Tseng, M. Théry, and M. Piel. 2010. Protein micropatterns: A direct printing protocol using deep UVs. *Methods Cell Biol.* 97: 133–46.
136. Kim, M., K.H. Song, and J. Doh. 2013. PDMS bonding to a bio-friendly photoresist via self-polymerized poly(dopamine) adhesive for complex protein micropatterning inside microfluidic channels. *Colloids Surf. B. Biointerfaces.* 112: 134–8.
137. Kim, M., J.-C. Choi, H.-R. Jung, J.S. Katz, M.-G. Kim, et al. 2010. Addressable micropatterning of multiple proteins and cells by microscope projection photolithography based on a protein friendly photoresist. *Langmuir.* 26: 12112–8.
138. Chichili, G.R., and W. Rodgers. 2009. Cytoskeleton-membrane interactions in membrane raft structure. *Cell. Mol. Life Sci.* 66: 2319–28.
139. Braeckmans, K., K. Buyens, B. Naeye, D. Vercauteren, H. Deschout, et al. 2010. Advanced fluorescence microscopy methods illuminate the transfection pathway of nucleic acid nanoparticles. *J. Control. Release.* 148: 69–74.